TU Wien
Department of
Applied Physics

Columbia University
Department of Applied Physics
and Applied Mathematics

Matthias Werl, BSc

Interpretation of synergistic effects between electron beam and microwave startup of a torsatron plasma

Master Thesis

Master programme Technical Physics

Technical University of Vienna

Supervisor:

Assoc. Prof. Francesco A. Volpe, Dr.rer.nat.

Department of Applied Physics and Applied Mathematics

Columbia University in the City of New York

Univ.-Prof. Mag.rer.nat. Dipl.-Ing. Dr.techn. Friedrich Aumayr

Institute for Applied Physics

TU Vienna

Vienna, April 2020

Abstract

The Columbia (non-)Neutral Torus (CNT) is a simple, low aspect ratio stellarator currently operated by Columbia university. It is unique in its design, consisting out of only four circular coils: Two interlocked coils in the center and two vertical field coils. Initially built to study non-neutral electron plasmas, it has since been re-purposed to study neutral plasmas by increasing the background pressure in its vacuum chamber.

For plasma start-up and heating, initially a filament was heated and then a bias voltage between the filament and the vacuum vessel walls was applied to extract electrons from the filament. Electrons spiral around the magnetic field lines with a frequency known as their gyrofrequency. If electromagnetic radiation at this exact same frequency are injected into a plasma, the particles can absorb the microwaves' energy using an effect known as electron resonant cyclotron heating (ECRH). To use this effect, a microwave source to heat the plasma was installed.

Either of these methods alone can start up a plasma. However, if both are used simultaneously, the measured plasma densities were higher than the sum of the densities obtained by either method alone (by a factor of around 2), implying some synergistic effect between the two.

Candidate mechanisms to explain the observed synergy were proposed and are studied in this thesis. One major candidate was that the electric field created by the microwaves might enhance the field emission from the heated filament, increasing the emission current. To examine this candidate, the emission current from the filament was calculated based on estimates.

The second major candidate mechanism to be studied in this thesis revolves around the efficiency of microwave absorption. The average energy of electrons emitted from the filament is around 100 eV. On the other hand, the background electrons starting up the plasma in the presence of microwaves have average energies of around 5 eV. The efficiency of microwaves absorption increases with the Larmor-radius r_L; which increase with energy. The electrons emitted from the filament can thus absorb the microwave energy more efficiently, enabling them to ionize more particles and create higher densities.

This proposed mechanism was studied by tracing single electrons in CNT's magnetic field. These electrons are subject to collision, including elastic collisions between charged particles, ionizing collisions and recombinations. Additionally, the electric field of induced microwaves will alter the particles' energy. A Monte-Carlo code was developed to study the particles. Comparing the results of many individual electrons, the average number of ionization events per unit time can be determined and be compared to loss mechanisms; such as recombination or particle escape. This will give insight on the obtainable densities.

It was found that even under optimistic assumptions the microwaves have no significant

impact on the filament emission currents. Particle tracing in CNT was performed and resulting Poincaré-plots qualitatively compared to previous models. The energy loss due to collisions was verified. Parameters used to compute the microwave electric field were varied and their effect onto the particles' energy absorption studied.

Kurzfassung

Der Columbia (non-)Neutral Torus (CNT) ist einfacher Stellarator mit einem geringen *aspect ratio*, welcher momentan an der Columbia University betrieben wird. Das einzigartige Design besteht aus lediglich 4 Spulen: 2 ineinander verriegelte Spulen im Zentrum und zwei Vertikalfeldspulen. Ursprünglich zur Analyse nicht neutraler Elektronenplasmen konzipiert, ist das Ziel nun die Analyse neutraler Plasmen. Dies wurde durch Erhöhung des Druckes in der Vakuumkammer erreicht.

Zur Plasmaerzeugung und -heizung wurde anfangs ein Draht erhitzt und durch Anlegen einer Spannung zwischen dem Draht und der Vakuumkammer Elektronen extrahiert. Die Elektronen bewegen sich auf Spiralbahnen um die magnetischen Feldlinien mit der charakteristischen Zyklotronfrequenz. Wird elektromagnetische Strahlung derselben Frequenz eingestrahlt, kann diese durch Elektron-Zyklotron-Resonanz (EZR) absorbiert werden und die Elektronen damit heizen. Hierfür wurde in weiterer Folge eine Mikrowellen-Quelle installiert um das Plasma zu heizen.

Jeder dieser beiden Methoden alleine kann ein Plasma erzeugen. Werden jedoch beide simultan verwendet, waren die gemessenen Plasmadichten höher als die Summe der Dichten welche durch den Einsatz einer einzelnen Methode erreicht wurden (um einen Faktor ≈ 2). Das weist auf einen synergistischen Effekt zwischen den beiden hin.

Mögliche Kandidaten zur Erklärung dieser Synergie wurden präsentiert und in dieser Arbeit untersucht. Ein erster Kandidat beinhaltet, dass das von den Mikrowellen erzeugte elektrische Feld den Emissionsstrom vom Filament erhöhen könne. Dieser Effekt wurde mithilfe von Schätzungen berechnet.

Der zweite Kandidat welcher in dieser Studie behandelt wurde befasst sich mit der Effizienz der Mikrowellen-Absorption. Die vom Filament emittierten Elektronen haben eine durchschnittliche Energie von ungefähr 100 eV. Im Vergleich dazu haben die Hintergrund-Elektronen, welche mithilfe der Mikrowellenheizung ein Plasma erzeugen können, eine Durchschnitts-Energie von 5 eV. Die Effizienz der Mikrowellenabsorption steigt mit dem Larmor-Radius r_L, welcher sich mit der Energie vergrößert. Die thermisch emittierten Elektronen können demnach die Energie der Mikrowellen besser absorbieren und damit mehr Teilchen ionisieren, was letztlich zu höheren Dichten führt.

Dieser Mechanismus wurde untersucht indem einzelne Elektronen im Magnetfeld des CNT verfolgt wurden. Die Elektronen stoßen dabei mit anderen Teilchen: entweder elastisch mit anderen geladenen Teilchen, durch Ionisations-Stöße oder Rekombinations-Stöße. Zusätzlich verändert das elektrische Feld der Mikrowellen die Energie des Teilchens. Ein Monte-Carlo Code wurde entwickelt um die Teilchen zu untersuchen. Durch Analyse vieler einzelner Elektronen kann die durchschnittliche Anzahl an Ionisations-Stößen pro Zeiteinheit bestimmt werden und mit Dichteverlust-Mechanismen verglichen werden. Das gibt Aufschluss über die

erreichbaren Dichten.

Selbst unter sehr konservativen Annahmen haben die Mikrowellen keinen bedeutenden Einfluss auf den Emissionsstrom des Filaments. Die Berechnung von Teilchenbahnen in CNT wurde durchgeführt und resultierende Poincaré-Plots wurden qualitativ mit früheren Modellen und Simulationen verglichen. Der Energieverlust der Teilchen als Folge von Stößen wurden mit analytischen Modellen verifiziert. Parameter, welche zur Berechnung des elektrischen Feldes der Mikrowellen benötigt werden, wurden variiert und deren Einfluss auf die Energie-Absorption der Teilchen untersucht.

Acknowledgements

Many people guided and accompanied me both in the path leading up to this thesis as well as during the research and writing process.

First, I want to thank the people I've worked with at the IPP in Germany. I want to thank Thomas Sunn Pedersen for establishing contact and thus opening up the possibility for this thesis. I also want to thank Elisabeth Wolfrum and Georg Harrer, who guided me through another related project and from whom I've learned a lot about the topic of fusion and plasma physics.

I want to thank the people I've met and worked with at Columbia University. Specifically, I want to thank my group members, James Borovilas, Sugal Sutter and Rui Diaz-Pacheco for creating the fun, friendly and fruitful environment in the lab. A special thanks goes to Manolis Maragkoudakis for additionally showing me around New York City after first arriving and becoming a very close colleague and friend.

I am grateful for the financial support granted by FuseNet, helping me fund my stay in New York.

I appreciate my supervisor from the TU in Vienna, Friedrich Aumayr, for the supervision and enabling me to write my thesis abroad in the first place.

Kenneth Hammond initially took the experimental data leading up to my thesis. I want to say my warmest thanks for continuing to help me and guide me in this project, even long after leaving Columbia for his next position.

I am utterly thankful for my supervisor at Columbia, Francesco Volpe, for giving me this opportunity and guiding me through the project. Countless hours were spent discussing my work and Francesco was always there to answer my questions, share his insight and further guide me through the project. I owe a great deal of my experience and knowledge to him and his guidance.

Last but not least I want to thank my parents. Without them, I would not be where I am today. They helped me throughout my whole academic studies, enabling my international experiences and supporting me in becoming the person I am today. I could never thank them enough for their continuous love and support.

Abbreviations

CIRCUS	**Circu**lar coil **s**tellarator
CMS	**C**enter of **m**ass **s**ystem
CNT	**C**olumbia (non-)**n**eutral **t**orus
COM	center of mass system
ECRH	**E**lectron **C**yclotron **R**esonant **H**eating
EOM	equations of motion
GCM	guiding center motion
ICRH	**I**on **C**yclotron **R**esonant **H**eating
IL	Interlocked
ITER	**I**nternational **T**hermonuclear **E**xperimental **R**eactor
LCFS	last closed flux surface
LHD	**L**arge **H**elical **D**evice
mfp	mean free pathlength
MHD	Magnetohydrodynamics
NBI	**N**eutral **B**eam **I**njection
PT	**P**article **T**racing
RK4	Runge-Kutta-4
RNG	**R**andom **N**umber **G**enerator
VF	Vertical field
W7X	Wendelstein 7-X

Contents

1. Introduction

The global demand in energy is constantly rising. Not only is the global population at an all-time high and still rising [1], but also the percentage of people living in highly developed and industrialized societies has never been higher. The energy consumption per capita is higher for more developed societies. [2, 3] Around 80% of the world's population are currently living in so-called 'developing' countries [5, 4], meaning that they have a still growing economy and their demand for energy and resources will increase even further in the future.

Following these developments, the demand for reliable, safe and efficient means of energy and electricity generation has become ever more crucial. Current, established means all have their disadvantages. Burning fossil fuels, like coal, oil and gas, leads to the emission of vast amounts of greenhouse gases. These greenhouse gases trap infrared radiation emitted by the Earth's surface, causing the temperatures on our planet to rise. This global warming effect could result in irreversible natural disasters, such as the melting of glaciers and polar caps as well as extreme weather conditions like droughts, monsoons and heavy thunderstorms.

Additionally, fossil fuels make countries dependent on other countries to supply these fuels. The global supply of these fossil fuels is dwindling and is expected to be depleted during the next 50-100 years [3], unless new reserves will be discovered.

Nuclear fission per se doesn't generate greenhouse gases; however, as of now there is no safe and reliable method of disposing of toxic nuclear waste. The threat of nuclear accidents and proliferation is ever present as well. Despite bigger reserves than fossil fuels, the supply of fissile material might eventually run out as well.

Renewable energy sources, such as hydroelectric, solar and wind power, don't face many of the problems fossil and nuclear fuels have. Most of these use fuels and energy sources which are generally abundant, such as solar or wind energy. However, their efficiency and overall capacities are usually strongly affected by regional and time-/date-related factors. Contemporary means of energy storage are not (yet) sufficiently advanced to store large amounts of energy for times when renewable technologies are not producing energy.

Nuclear fusion wouldn't face many of the problems presented above. Its fuel is contained in (sea) water and is extremely energy-dense, meaning practically infinite supply anywhere on the planet. Unlike renewables, it could be operated without substantial regional constraints and can, like fossil fuels and nuclear power, deliver electric power at any time. Probably most important of all: It creates practically no dangerous or toxic by-products. The only waste created during operation would be materials activated due to the constant bombardment with neutrons. This waste would be easier to handle than for nuclear fission. Nuclear fusion reactors would be safe, as the worst case scenario would mean that plasma confinement would be lost and the plasma would cool off quickly, potentially damaging the reactor but under no circumstances leading to fatal incidents like explosion or nuclear meltdowns.

Probably the biggest promise of nuclear fusion is its high energy gain. Fusing 1 g of hydrogen can potentially release the same amount of energy as burning 70,000 t coal.

The main downside of nuclear fusion however is its complexity. Research on the civil use of fusion power has been conducted since the 1950's. It was believed nuclear fusion would be available within 2 decades; however, successfully confining a plasma long enough to get a net energy gain proved to be a lot more complex than initially presumed. During the past decades of research, many breaking and fundamental discoveries in plasma physics have been made. Current devices such as ITER, currently under destruction in southern France or W7X, currently under operation in Germany, might prove the viability of this technology and will hopefully pave the way for future nuclear fusion power plants.

1.1. Nuclear fusion

In nuclear fission, a heavy nucleus is bombarded with a neutron, rendering the nucleus unstable. As a result, the nucles is split into two (or more) smaller nuclei, releasing energy. Nuclear fusion is similar; however, here two smaller nuclei are fused into a heavier one, releasing energy in the process. The energy difference Q related to both processes can be calculated using Einstein's famous energy-mass relation:

$$Q = \left(\sum_i m_{initial} - \sum_i m_{final} \right) \cdot c^2 \tag{1.1}$$

where $\sum_i m_{initial}$ is the sum of the mass of all involved particles before the process and $\sum_i m_{final}$ is the sum of all masses after the process. If $\sum_i m_{final} < \sum_i m_{initial}$, energy is released. The mass difference can be explained using nuclear physics models such as the drop model. [6] Essentially, when splitting the nuclei are more stable due to inter-nuclear forces, meaning that less energy is needed as binding energy to hold the nuclei together. The excess energy is then released. Fig. 1.1 shows the binding energy per nucleon (=protons and neutrons). It shows that light nuclei gain energy if fused together; this process works for all nuclei lighter than iron. All elements heavier than iron release energy only if they are split. The most common fission materials are ^{235}U and ^{239}P, but recently research on reactors using ^{232}Th has been conducted.[7, 8, 9] Since only the fusion of light nuclei releases energy, heavier elements are only created when there is a surplus of energy to create heavier elements. This is the case in supernovae and is the origin of all elements heavier than iron in our universe.

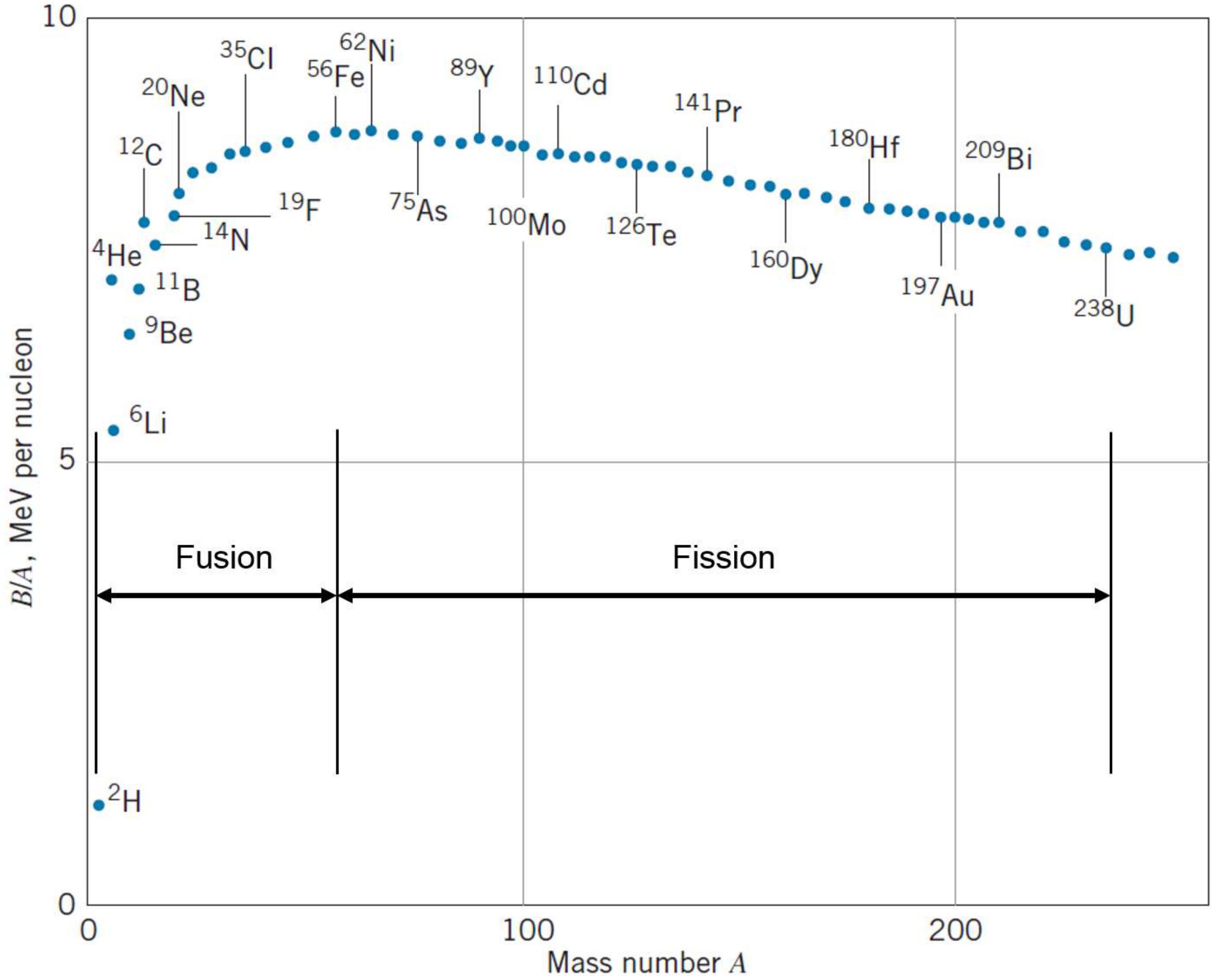

Figure 1.1: Binding energy per nucleon B/A as function of atomic mass number A. Modified from [10].

Nuclear fusion is the main energy source of our (visible) universe and takes place in every star. Each star undergoes a cycle of different fusion processes with different fuels. On earth however, only a few processes would be viable due to their cross-section σ; which is a measure of the probability of the fusion process to occur; being high and peaking at relatively low energies. Currently, the main global research focuses mainly on fusing Deuterium ${}^2_1D$ and Tritium ${}^3_1T$, two isotopes of Hydrogen, to a Helium ${}^4_2He$ nucleus (and an excess neutron):

$$
{}^2_1D +^3_1 T \rightarrow^4_2 He +^1_0 n + \underbrace{17.6\ MeV}_{E_{ex}} \tag{1.2}
$$

where the excess energy E_{ex} is split as kinetic energy between the two products. 3.5 MeV are obtained by the ${}^4_2He$-particle, the other 14.1 MeV are obtained by the neutron.

The Coulomb force causes two (positively) charged nuclei to repel each other. To get two nuclei close enough in order for them to fuse, matter needs to be either sufficiently dense and/or hot. While stars use gravity, on earth this is not possible and thus higher temperatures are necessary.

At the high temperatures/energies involved in these processes, matter exists in its fourth state of matter, the plasma state.

1.2. Plasma physics

When free electrons in a gas are sufficiently energetic, they can collide with neutral atoms with a chance of ionizing the atom in the process. A second, free electron is created alongside a positively charged nucleus. When this process occurs regularly, which can be achieved by heating a gas or by applying electric fields, more and more ionization events will occur. If there are enough ionization processes to counter charged particle losses, such as the recombination of an electron with an ion, matter will be in a plasma state. Despite this state being very uncommon on earth it is in fact the most common state of matter in our universe.

Plasma in many ways behaves quite differently from the other states of matter. One of the most characteristic features of this state is that the charges move freely and can thus be affected by outer electromagnetic fields. However, the total (net) charge of a plasma will still equal to (approximately) zero. This is referred to as *quasi-neutrality*:

$$\sum_i (Z_i n_i) \approx n_e \tag{1.3}$$

where Z_i is the nuclear charge for particle of type i, n_i is the particle density of type i and n_e is the density of the electrons.

1.3. CNT

The probability for ions to fuse is very low, meaning an ion on average has to pass many other ions before it will eventually fuse. It is thus crucial to keep the ions confined together over longer periods of time.

The idea for most terrestrial approaches for fusion is to use magnetic fields to confine the particles. In first approximation, on the net of "drifts" that will be discussed later, a charged particle will follow the path of a magnetic field line. Thus, by clever design, charged particles can be confined over extended periods of time and may eventually fuse.

The **C**olumbia (non-)**n**eutral **t**orus (CNT) is an example of a magnetic confinement experiment. It is a Stellarator-type device ([11],see section 2.3.2) currently operated at the Columbia University in the City of New York, United States. Despite being too small to study fusion-relevant plasmas, it can still be used to study fundamental properties of plasma physics. Its construction was finished in 2004 and it was initially scheduled to study (non-neutral) electron plasmas. [12, 13, 14]

CNT is one of the simplest and the world's lowest aspect ratio device currently in operation. [15] It consists of only four coils: 2 Interlocked coils (IL) in the center and two vertical field coils (VF) on the outside. The plasma is created inside a steel vacuum chamber enclosing the IL-coils. The VF-coils are located outside the vessel. A schematic of the coils and the resulting plasma is shown in Fig. 1.2a. Fig. 1.2b shows the vacuum-vessel including the VF-coils and auxiliaries.

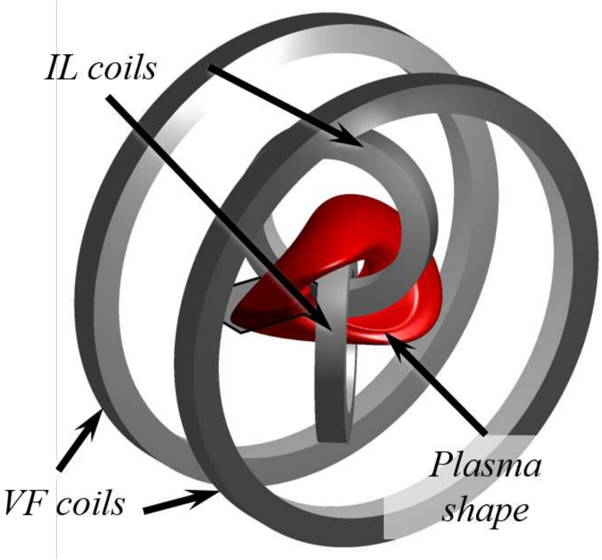

(a) Coil configuration (grey) and plasma shape (red) of CNT.

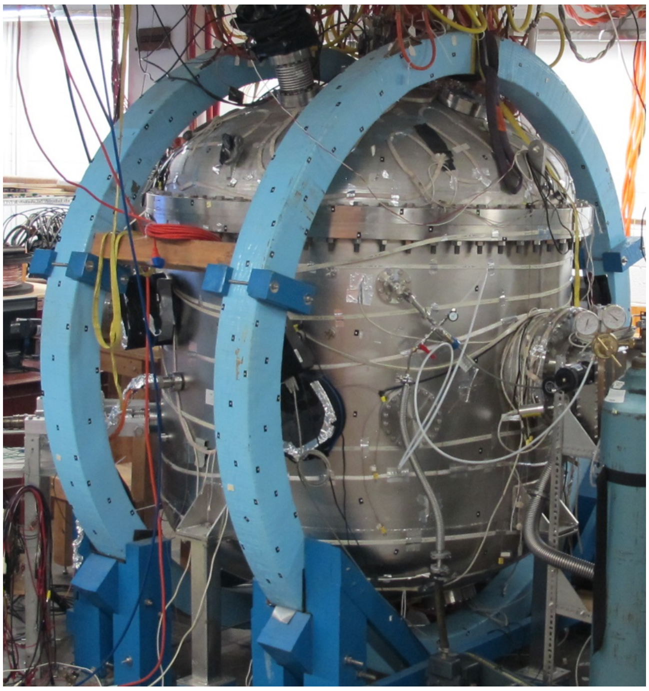

(b) Photograph of CNT vessel including the VF-coils and auxiliaries.

Initially, pure electron plasmas were created by pumping down the vessel to very low background pressures and emitting electrons into the vessel using an electron gun. This was essentially heated filament, biased relative to the vessel in order to emit and accelerate electrons.

If the background pressure is increased, an increasing amount of background atoms will be ionized, changing the neutrality of the plasma (see eq. 2.1). [16, 17]. In 2012, the experiment was taken over by Professor Francesco Volpe and the main objective of CNT was switched to study fundamental effects of neutral plasmas. The recent research focus has been mostly on studying error-fields in Stellarators [18, 19] and overdense microwave heating as a means towards high-beta stability studies. [20, 21] The latter is specifically interesting in CNT, since due to the low magnetic fields (on-axis: $B_0 \approx 87.5\ mT$) high values of the plasma-β (ratio of plasma pressure p_p to magnetic pressure p_m) can be achieved:

$$\beta(\vec{r}) = \frac{p_p}{p_m} = \frac{n k_B T}{B^2(\vec{r})/2\mu_0} \tag{1.4}$$

where n is the plasma density, k_B the Boltzmann constant, T the plasma temperature, $B(\vec{r}) = |\vec{B}(\vec{r})|$ the magnitude of the magnetic field at any point $\vec{r}$ and μ_0 is the vacuum permeability.

1.4. Aim of this thesis

As a first step towards overdense microwave heating, a crude 1 kW Magnetron was installed to heat the plasma. The operation of the magnetron was pulsed, sending pulses of length $\tau \approx 6\ ms$ at a repetition rate of $f_{rep} \approx 60\ Hz$. The frequency of the microwaves was $f = 2.45\ GHz$ and the on axis magnetic field B_0 was chosen such that the electron cyclotron frequency Ω_{ce} coincides with the wave frequency. Ω_{ce} is the frequency at with which the particles revolve around the magnetic field lines:

$$\Omega_{ce} = \frac{eB_0}{m_e} \tag{1.5}$$

, where m_e is the electrons' mass and e its charge.

It was observed that when microwave heating was applied alongside the electron gun (already in use before), a synergistic effect occurs. The densities measured when simultaneously using both start-up mechanisms were higher than the sum of the densities obtained by either method alone. Fig. 1.3 shows that the measured densities. The densities obtained by the combined use (red line) is higher by a factor of about 2-3, compared to a purely electron gun plasma (black line) or a purely wave-heated plasma (blue line).

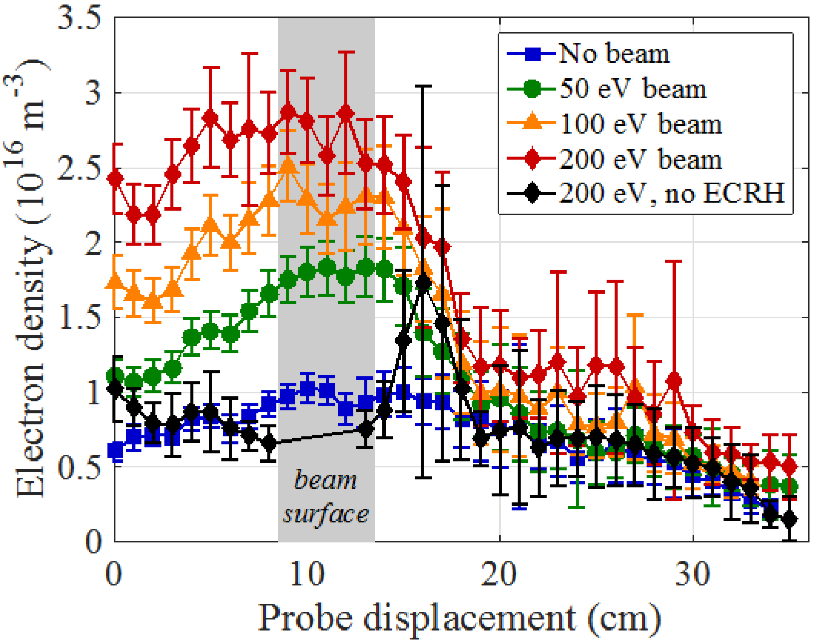

Figure 1.3: Densities measured as a function of probe displacement/radial extension from the center axis. The beam electrons stem from the electron gun heating, whilst the ECRH heating was obtained from the Magnetron.

The experimental setup for these measurements is shown in Fig. 1.4. An array of Langmuir probes (denoted as 1 in the figure), which measure the temperature and density at a given point, was mounted on a moving bellows drive (2) to measure at different radial positions from the center. A second array of probes was mounted on a second bar (3) which were heated and served as the electron gun. The microwaves entered the vessel through a small port (4) on the upper side of the vessel. The port window was a quartz window with a diameter of $d \approx 25\ cm$.

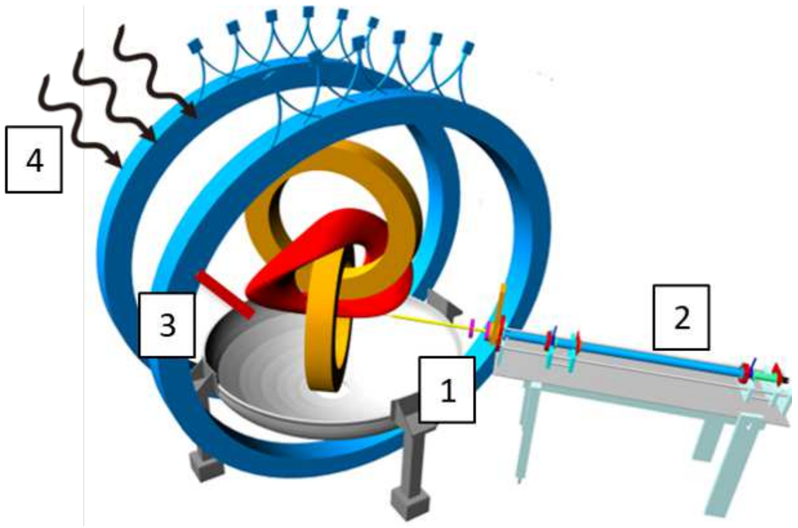

Figure 1.4: CNT Experimental Setup for synergy measurements.
1: Langmuir probes. 2: Bellows drive. 3: Electron gun. 4: Microwave oven.

The experiments were conducted at background pressures of (2-5) $\mu torr$. Despite the magnetron having a total power output of $P = 1\ kW$, it is known that much less power actually coupled to the plasma. This was due to the rudimentary setup deployed in this simple experiment: the magnetron was mounted outside the vessel and injected the microwaves in the vessel through a quartz window. The magnetron is effectively a point source and since no optics were used to refocus and properly aim the beam, only a fraction of the power injected reached the plasma at the first transit or after multiple reflections within the vessel. The rest was lost through the windows or dissipated on the vessel due to its reflectivity being less than 100%.

Several candidate mechanisms were proposed to explain this synergy. They were grouped into two main categories:

Microwaves enhancing electron gun start-up

1. One proposed mechanism is that the electric field created by the microwaves enhances the emission current from the electron gun. The current density j_{em} is proportional to the electric field strength E applied:

$$j_{em} \propto exp(E) \tag{1.6}$$

   The microwaves would create an additional electric field, added to the field created by the bias.

2. A second possibility is that microwaves alter the $\vec{E} \times \vec{B}$-drifts of particle orbits and/or the plasma potential V_{plasma}. Both can have a positive effect on confinement in CNT,

as known from a previous study [22] where, however; they were not controlled by microwaves.

Electron gun enhancing microwave start-up

3. The densities and temperatures present in CNT are in a regime where the optical thickness, being the fraction of incident wave power absorbed in one pass, is proportional to the square of the Larmor radius $r_{L,e}$ (see eq. 2.9): [23]

$$\tau \propto r_{L,e}^2 \tag{1.7}$$

In the absence of the electron gun, the background electron temperature is $T_e \approx 5\ eV$, leading to an average Larmor radius of $r_{L,e} \approx 60\ \mu m$. When the electron gun is activated and biased at -200 V with respect to the vessel, an additional population of electrons with an average temperature of $T_e \approx 100\ eV$ will be introduced. Fig. 1.5 illustrates this situation: It shows the distribution of particles at certain energies. The blue line shows the Maxwell-Boltzmann distribution of the background electrons at $T \approx 5\ eV$. The orange line is a small distribution of electrons centered around $E \approx 100\ eV$, depicting the electrons ejected by the electron gun.

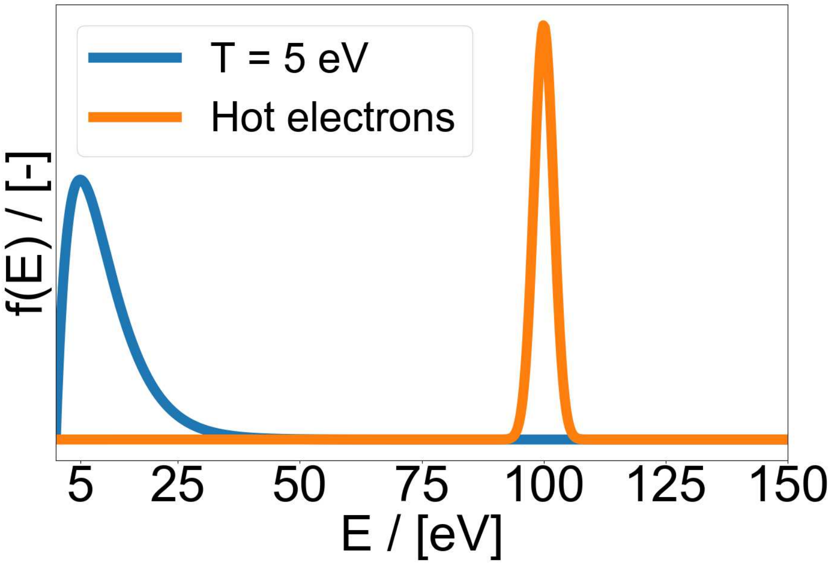

Figure 1.5: Sample energy distribution function. The blue line is the Maxwell-Boltzmann distribution function for electrons with T = 5 eV, the orange line marks an additional population introduced by the biased filament.

The hot electrons have an average Larmor-radius of $r_{L,e} \approx 400\ \mu m$ and can thus potentially absorb the incident microwaves more efficiently. Additionally, since more wave power is absorbed during the first pass, less power is lost to reflections off the vessel walls or to leakage through unshielded ports.

4. The voltage applied already partially breaks down the gas between the two electrodes (filament and vessel walls), releasing electrons in the process. These additional electrons are also subject to wave-resonant absorption. That is, they gain energy, and some of them become energetic enough to cause more ionization events, leading to higher densities. After the plasma has fully formed, the potential will be shielded everywhere but in the close vicinity of the two electrodes (sheath). Electrons outside of these regions won't feel the electric field.

This thesis investigates the enhancement of the emission current due to microwaves (first proposed mechanism) as well as the more efficient microwave absorption of the hot electrons (third mechanism).

The thesis is structured as follows: Chapter 2 will give the theoretical background necessary to understand the methods applied. Chapter 3 explains the exact procedure and methods used to model and study the synergy. Chapter 4 will show the results obtained from the modelling. Chapter 5 summarizes the work performed and chapter 6 gives an outlook for future work. Appendix A summarizes the most important formulas used.

2. Theoretical background

This chapter describes the theoretical background necessary to understand the phenomena described in this thesis.

2.1. Plasma physics

Criterion for a plasma For an ionized gas to be considered a plasma; being a state where collective effects dominate over binary interactions; it needs to fulfil some criteria. A plasma is often considered the fourth state of matter. The ionized gas contains electrons, positively charged ions and potentially neutral atoms or molecules. Unlike other states of matter, it contains charged particles which interact with (outer) electromagnetic fields. The long-ranging interactions between the single constituents typically leads to collective phenomena.

The probability to find the negative charges close to other positive charges is higher than finding them further away. This follows from the potential created by a charge decreasing in strength with increasing distance from the charge. The Debye-length λ_D is the length after which the potential $V(r)$ from a charge has dropped to $\frac{1}{exp}$ of its unshielded value. At distances $d \gg \lambda_D$, the potential is effectively shielded: [24]

$$V(r) = \frac{1}{4\pi\varepsilon_0}\frac{e}{r}exp(-\frac{r}{\lambda_D}) \tag{2.1}$$

$$\lambda_D = \sqrt{\frac{\varepsilon_0 k_B T}{ne^2}}, \tag{2.2}$$

with ε_0 the vacuum permittivity, k_B the Boltzmann-constant, T the plasma temperature, n the plasma density and e being the fundamental electron charge.

There are three main criteria for a plasma. [25] First, to ensure collective behaviour of the single constituent particles, the plasma needs to be bigger than λ_D:

$$L \gg \lambda_D$$

The second criterion refers to the plasma parameter N_D. It gives the number of particles inside the Debye-sphere, being a sphere with radius λ_D. The plasma parameter is defined as:

$$N_D = n\frac{4\pi}{3}\lambda_D^3. \tag{2.3}$$

It needs to be:

$$N_D \gg 1.$$

When electrons in a plasma are pulled away from the ions (due to external forces or thermal movement), they will experience a force pulling them back towards the ions. Due to the electron mass inertia, they will 'overshoot' their equilibrium position and the force will reverse, pulling them back in the other direction. The particle will end up oscillating around its equilibrium position. The oscillatory motion can be compared to an harmonic oscillator with the (angular) plasma frequency ω_{pe}:

$$\omega_{pe} = \sqrt{\frac{n_e e^2}{m_e \varepsilon_0}}. \tag{2.4}$$

The ions will experience a similar oscillation with the ionic plasma frequency $\omega_{p,i}$:

$$\omega_{pi} = \sqrt{\frac{n_i (Z_i e)^2}{m_i \varepsilon_0}}, \tag{2.5}$$

where $(Z_i e)$ is the charge of the ion. The total plasma-frequency is the sum of the two:

$$\omega_p^2 = \omega_{pe}^2 + \omega_{pi}^2, \tag{2.6}$$

but due to the heavy mass of the ions ($m_i >> m_e$), the ionic plasma frequency can usually be neglected $\omega_{pe}^2 >> \omega_{pi}^2$ and the plasma frequency is:

$$\omega_p^2 \approx \omega_{pe}^2.$$

The oscillations can only form if the particles are not disturbed by collisions. The oscillations time $\tau_{pe} = \frac{2\pi}{\omega_{pe}}$ needs to be short compared to the time between two subsequent collisions $\tau_{ce} = \frac{1}{f_{ce}}$, which gives the third criterion for a plasma:

$$\tau_{pe} \ll \tau_{ce}.$$

Gas discharge A common application of plasma physics is in a discharge tube. Here, an electric voltage is applied between two cathodes which will (partially) ionize the gas contained within, creating free electrons and leading to a current flowing through the gas. The degree of ionization α gives the proportion of ionized particles inside a plasma:

$$\alpha = \frac{n_e}{n_e + n_n}. \tag{2.7}$$

For low values of $\alpha << 1$, in a so-called weakly ionized plasma, there are (still) many neutral atoms present. In a fully ionized plasma, $\alpha \to 1$ and thus all atoms are (fully) ionized.

Due to the different particles partaking at different values of α, the dynamics are different.

If a voltage is applied between the two electrodes of a gas, the initial potential curve will vary linearly between the cathodes. The electrons are much more mobile than the ions, meaning they will arrive at the cathode long before the ions reach the anode. Due to many electrons impacting on the cathode, a surplus of negative charges will accumulate, repulsing more electrons whilst attracting additional ions. In the bulk of the plasma, the majority of electrons will have been drained, leaving behind a surplus of ion. The distribution of the *plasma potential* V_p, which is the potential created by the plasma itself, is shown in Fig. 2.1: The ions in the bulk plasma will cause a positive potential which drops rapidly in the small region before the cathode, known as the **Cathode sheath**.

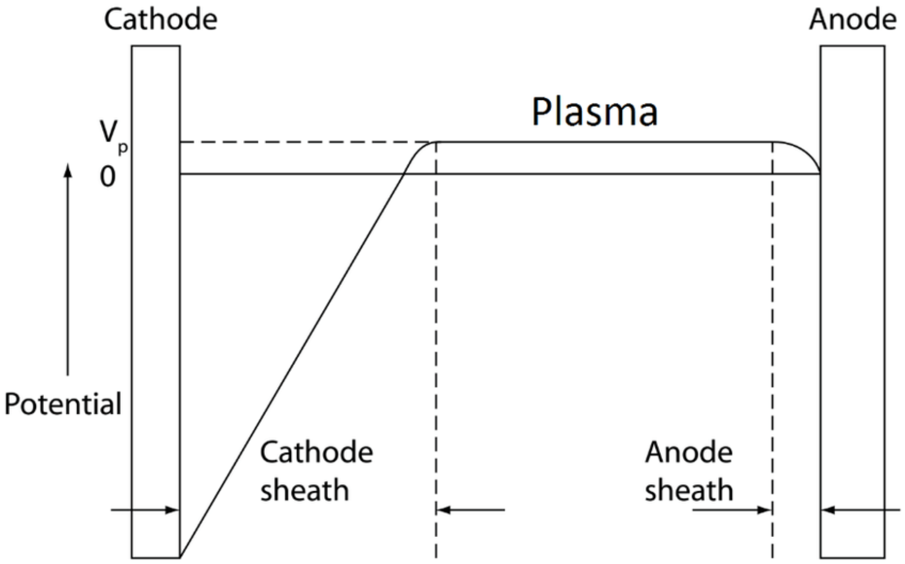

Figure 2.1: Plasma potential inside a plasma during a glow discharge. [26].

A similar potential drop will form in front of the anode (*anode sheath*), however the drop is not as steep.

An externally applied voltage will be shielded inside the plasma and will only be felt in the sheath regions.

2.2. Particle motion in electromagnetic fields

Charged particles in the presence of electromagnetic fields will be subject to the Lorentz-force $\vec{F_L}$:

$$\vec{F_L} = q \cdot (\vec{E} + \vec{v} \times \vec{B}) \tag{2.8}$$

where q is the particles charge, $\vec{E}$ an electric field, $\vec{v}$ the particles' velocity and $\vec{B}$ the magnetic field. In the absence of an electric field, the Lorentz force causes the particles to spiral around the magnetic field lines with an effective radius r_L, called the Larmor-radius:

$$r_L = \frac{mv_\perp}{|q|B}, \tag{2.9}$$

with $v_\perp$ being the particles' velocity component perpendicular to the direction of the applied magnetic field $\vec{B}$ and m the particles' mass. The (angular) frequency of this *gyromotion* is given by:

$$\Omega_c = \frac{|q|B}{m}. \tag{2.10}$$

Fig. 2.2 shows this gyromotion (black line) around a magnetic field line (black dotted line).

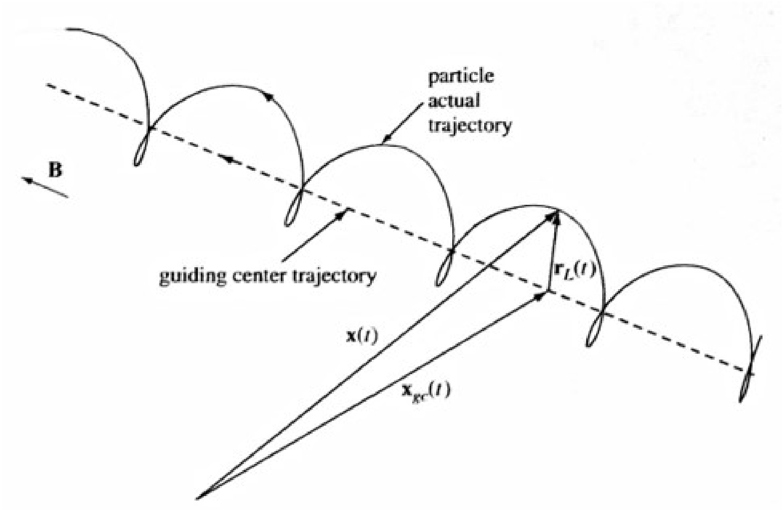

Figure 2.2: Particle trajectory (sold line) in the presence of a magnetic field (dashed line). The particle will spiral around the magnetic field lines at a radius of r_L, with the frequency Ω_{ce}. [27].

2.2.1. Guiding center motion

The gyromotion shown in Fig. 2.2 is typically very fast. For instance, in the presence of an on-axis magnetic field of $B_0 = 87.5\ mT$ (as used in CNT), electrons have an (angular) gyro-frequency in the order of 10 GHz. For many applications, one can simply average over the gyrophase of the particle and look at the so-called guiding center motion (GCM) [28]. In Fig. 2.2, the GCM coincides with the magnetic field line. However, in non-uniform magnetic fields (which is practically always the case), gyrations with a non-uniform Larmor radius r_L occur and, as a result, slowly "drift" with respect to its unperturbed orbit. Essentially, the particle's orbit will not close after one gyration and the guiding center will slowly drift across the magnetic field. The particle's magnetic moment μ in this case is an adiabatic invariant, remaining constant: [29]

$$\mu = \frac{W_\perp}{B} = \frac{mv_\perp^2}{2B} = const. \tag{2.11}$$

Using the Lagrangian of this system, one obtains the equation of motion of the guiding center, here written in components parallel and perpendicular to the magnetic field: [28]

$$m\dot{v_{||}} = (Ze)\cdot E_{||} - \mu\nabla_{||}B \tag{2.12}$$

$$\vec{v_d} = \vec{v_\perp} = \underbrace{\frac{\vec{E}\times\vec{B}}{B^2}}_{E\times B-drift} + \underbrace{\frac{v_\perp^2}{2\Omega_e}\vec{b}\times\nabla ln(B)}_{\nabla B-drift} + \underbrace{\frac{v_{||}^2}{\Omega_e}\vec{b}\times\vec{\kappa}}_{curvature-drift} \quad . \tag{2.13}$$

Here, (Ze) is the particle charge, $E_{||}$ the component of an electric field parallel to the magnetic field and $\nabla_{||}$ the gradient parallel to the magnetic field. In eq. 2.13, the first component is termed the $\vec{E}\times\vec{B}$ drift. The second term, the ∇B-drift, follows from the magnetic field strength changing as a function of the position $\vec{r}$. $\vec{b} = \frac{\vec{B}}{B}$ is the normalized direction of the magnetic field. Finally, a curvature of the magnetic field (with curvature vector $\vec{\kappa}$) will also alter the motion.

A particle's trajectory can be obtained by integrating the (differential) equations of motion. Numerical approaches compute the velocity and position after a short timestep Δt, given the initial values are known. The GCM is computationally less expensive, as stepsizes bigger than the distance over which a particle completes a full gyrocircle can be used without losing accuracy.

2.3. Magnetic confinement

2.3.1. Linear type confinement

Several different concepts and designs to magnetically confine plasmas have been studied and developed over the years. At first, *pinch* configurations seemed promising: here, a current carrying filament in the z-direction creates a poloidal magnetic field B_θ around the filament. The situation is sketched in Fig. 2.3.

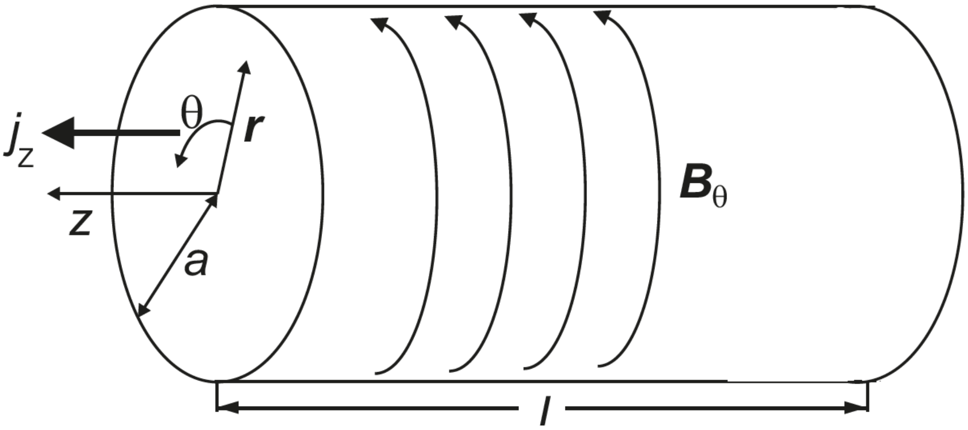

Figure 2.3: Sketch of the (linear) pinch configuration. A current-carrying filament (pointing in the z-direction) creates an azimuthal magnetic field B_θ. [30].

Often the filament is a plasma itself; the current stemming from electrons accelerated by a voltage applied between two electrodes. The resulting Lorentz-force

$$\vec{F}_L = q(\vec{v} \times \vec{B}) = q(\vec{v}_z \times \vec{B}_\theta) = F\hat{e}_r \tag{2.14}$$

points in the radial direction. For negatively charged electrons it causes a compression of the filament, until the compression force and the opposing plasma pressure p_p are in equilibrium:

$$p_p = nk_BT \tag{2.15}$$

$$F_{pinch} = p_p \cdot A_{surface} \tag{2.16}$$

with $A_{surface}$ being the surface area of the filament on which the pressure acts.

Despite having decent confinement properties, this configuration is very frail to instabilities. Small kinks in the filament for instance lead to an alteration of the magnetic field and subsequent ejection of particles.

An improvement of the pinch-configuration is the screw-configuration. In this configuration, an additional magnetic field pointing in the direction of the filament B_z is applied. This leads to the effective field lines following a winding pattern around the filament, giving this setup its name. A sketch is shown in Fig. 2.4.

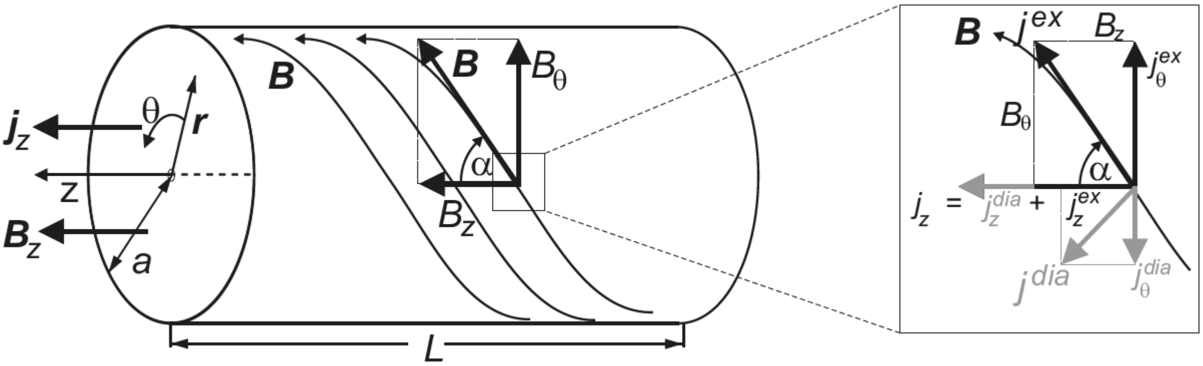

Figure 2.4: Sketch of the screw-pinch configuration. An additional linear magnetic field B_z is applied in the direction of the current, creating helical field lines around the filament. [30].

This configuration is less susceptible to instabilities, as they can be countered whilst still keeping the relatively good confinement properties of the linear z-pinch.

Both setups have the disadvantage that due to their finite, linear extent, particles will be lost at either end. A possible way to counter this is by using a magnetic mirror. Here, the coils are aligned in such a way, that the magnetic field strength will increase towards the ends of the design. This is sketched in Fig. 2.5. The electrons will gyrate around the magnetic field lines, pointing in the z-direction. Since the magnetic moment μ (eq. 2.11) is conserved, higher values of B lead to an increase in the perpendicular velocity $v_\perp$. The total kinetic energy $E_{kin} = \frac{m}{2}(v_{||}^2 + v_\perp^2)$ is conserved; thus increasing $v_\perp$ causes a decrease in $v_{||}$. This process will continue until $v_{||} \to 0$ and the particle is reflected.

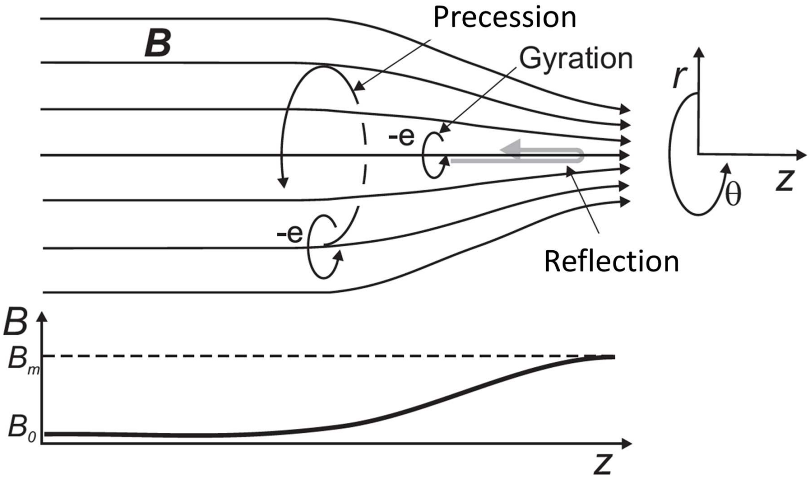

Figure 2.5: Setup of a magnetic mirror machine. The magnetic field strength increases in the z-direction, causing $v_{||}$ to decrease due to conservation of magnetic moment μ, eventually reflecting a charged particle. Modified from [30].

Not all particles are reflected however, since the magnetic field cannot be made infinitely high.

To evaluate if a particle will leave the setup, we define the *pitch-angle* α as the angle between a particles' velocity and the magnetic field, relating the velocity components of the particle:

$$\alpha = tan^{-1}(\frac{v_\perp}{v_{||}}) \tag{2.17}$$

The perpendicular velocity is thus $v_\perp = v \cdot sin(\alpha)$ and the magnetic moment can be written as $\mu = \frac{mv^2}{2} \cdot \frac{sin^2(\alpha)}{B} = const.$ At the point of reflection, $\alpha \rightarrow \frac{\pi}{2}$. If the point of reflection lies at the maximum magnetic field B_M (being the last possible point of reflection), conservation of magnetic moment gives:

$$\frac{mv^2}{2}\frac{sin^2(\alpha_0)}{B_0} = \frac{mv^2}{2}\frac{sin^2(\alpha_M)}{B_M} \tag{2.18}$$

with α_0/B_0 being the pitch-angle/magnetic field at the center of the setup. With $sin^2\left(\frac{\pi}{2}\right) = 1$, the maximum pitch-angle for reflection yields:

$$sin(\alpha_0) = \sqrt{\frac{B_0}{B_M}}. \tag{2.19}$$

Particles with a pitch-angle at the center $\alpha > \alpha_0$ will be lost. Particles inside the *loss cone*, a cone with angle α_0, will be confined in this setup.

2.3.2. Toroidal type confinement

Another method to prevent particle losses at the ends is to combine the ends and form a torus. Due to the toroidal geometry of most machines, it is convenient to use toroidal coordinates (r, φ, θ). It is related to the Cartesian coordinate system as follows:

$$x = (R_0 + rcos(\theta))cos(\varphi) \tag{2.20}$$

$$y = (R_0 + rcos(\theta))sin(\varphi) \tag{2.21}$$

$$z = rsin(\theta). \tag{2.22}$$

Here, R_0 (*major radius*) is the distance from the center of the torus (*minor axis*) to the origin of the coordinate system (*major axis*). r (*minor radius*) is the radius from the minor axis to a point inside the torus. $0 \leq \theta \leq 2\pi$ is the poloidal angle (angle in a poloidal cut plane) and $0 \leq \varphi \leq 2\pi$ is the toroidal angle, revolving around the major axis. Fig. 2.6 illustrates the coordinate system used.

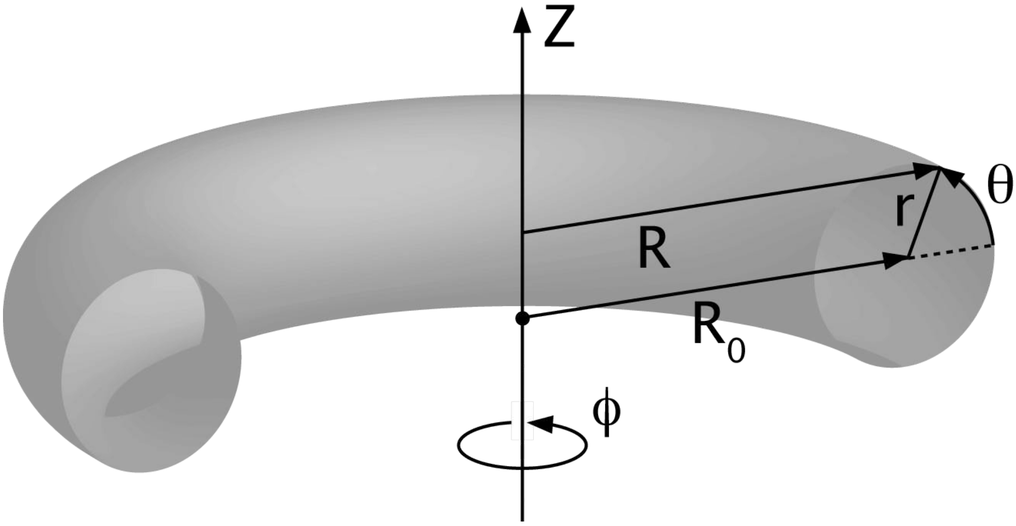

Figure 2.6: Toroidal coordinate system, as used in most magnetic confinement machines. [31]

The simplest torus is the simple magnetized torus: here, only a toroidal magnetic field B_φ is present. The charged particles will spiral around the field-lines. However, it can be shown that for this simple setup, the particles will be lost due to drifts. [30, 25] To counter these drifts, an additional poloidal magnetic field B_θ is necessary. The resulting magnetic field-lines will follow a helical pattern around the torus, similar as for the screw-pinch configuration. A sketch is shown in Fig. 2.7.

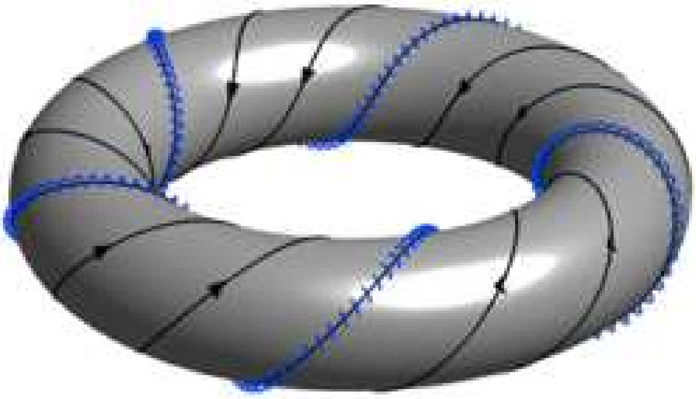

Figure 2.7: Sketch of a fully magnetized torus. The toroidal and poloidal magnetic fields B_φ/B_θ create helical magnetic field lines (black lines) around the torus. The blue lines represent the motion of a charged particle. Courtesy of K. Hammond.

The helical field lines are generally not closed. Following a single field line several times around the torus will define a surface known as *flux surface*. These flux surfaces play a central role in plasma confinement and the design of a confinement device. For a simple magnetized torus, the flux surfaces are single tori nested into each other, as shown in Fig. 2.8. In general, the shape of the flux surfaces depends on the magnetic topography.

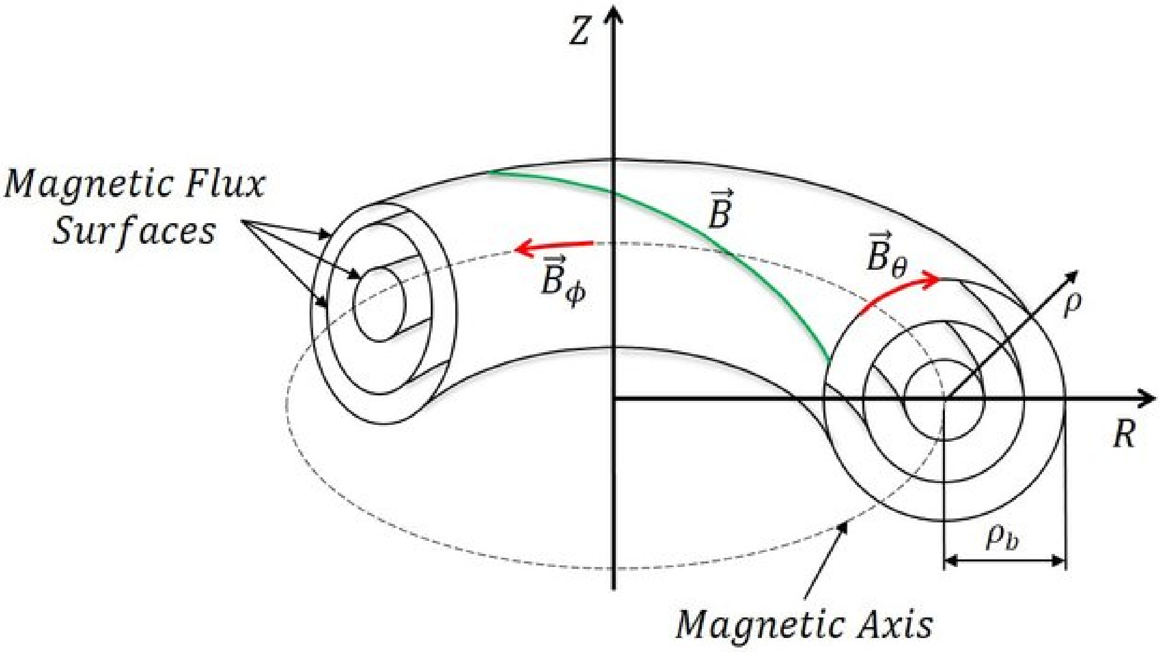

Figure 2.8: Magnetic field topology and resulting magnetic *flux surfaces* in a magnetized torus. [32]

Two different designs for fully magnetized toruses are currently being studied: the *tokamak* design and the *stellarator* design.

The word tokamak, being a transliteration of the Russian acronym '**to**roidal'naya **kam**era s **ak**sial'nym magnitnym polem', translates to 'toroidal chamber with axial magnetic field'. This design, originally invented by Russian scientists during the 1950's, uses the plasma current flowing in the toroidal direction $\vec{j} = j\hat{e_\varphi}$ to produce the poloidal magnetic field component B_θ. Additional toroidal field coils, arranged around the torus, create the necessary toroidal field component B_φ.

The need for high magnetic field strengths requires high currents. The plasma current is driven using the plasma as the second winding of a transformer with a central solenoid serving as the first winding. This induces a current in the plasma, strong enough to create the poloidal magnetic field component B_θ necessary. An additional set of vertical field coils ensures vertical stability and prevents the particles from escaping in the vertical direction. A schematic of a tokamak is shown in Fig. 2.9.

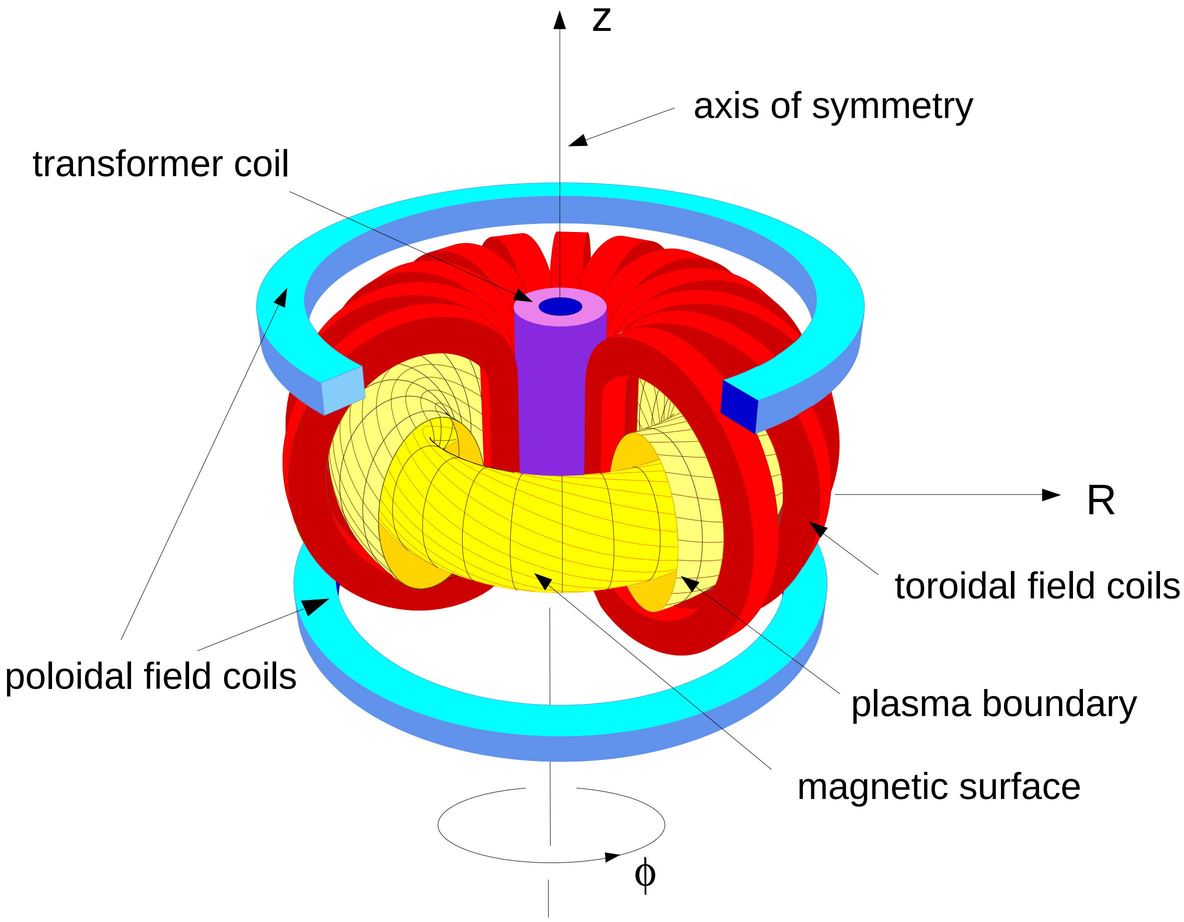

Figure 2.9: Schematic of a tokamak including the magnetic surface of the plasma (yellow), the transformer coil (central solenoid, violet), the toroidal field coils (red) and the vertical field coils (turquoise). [33]

A major downside of a tokamak is its need for the plasma current to operate. When the (directed) plasma current weakens or breaks down, previously confined particles will escape (due to drifts). For most designs, the plasma current can only be driven as long as the central solenoid still operates. Contemporary solenoids usually store enough energy to drive the plasma for several seconds before being depleted. The energy for the central solenoid is usually stored using large flywheels. [34]

Designs using microwaves for the current drive are currently being studied; [35], however, they still require additional investigation.

A stellarator, its name deriving from the latin word *stella* (star), uses only external coils to produce the magnetic field necessary for confinement. In a stellarator, there is no need for a plasma current, removing the pulsed operation limitation. The stellarator is a steady-state device capable of continuous operation.

Several different designs have been studied in the past. A *heliotron* for instance uses helical coils wrapped around the plasma vessel. These coils are able to create the necessary poloidal and toroidal magnetic field components. Fig. 2.10 shows an aerial view of the helical coils for the **L**arge **H**elical **D**evice (LHD) in Japan, the world's biggest device of this type.

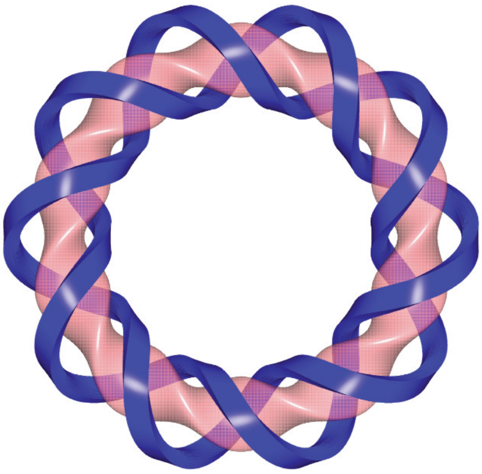

Figure 2.10: Aerial view of the helical coils for LHD. The coils are shown in blue and the resulting plasma shape is shown in pink. [36]

A different type of stellarator uses modular coils. These modular coils allow an in principle arbitrary magnetic configuration, allowing arbitrary optimization to fulfil certain criteria. This optimization is usually performed numerically, which means that this type of Stellarator could only effectively be studied with the development of high performance computers in the late 20th century. The most prominent example is the Wendelstein 7-X (W7X), currently operating in Greifswald, Germany. It uses a set of 5 different coils which are mirrored and periodically repeated, leading to a total of 50 coils; at the cost of high complexity in plasma shape and device construction.

In 2018, during its second operation phase, it already set a world record for the highest triple product (eq. 2.33) of any stellarator worldwide. [37] Currently undergoing construction and upgrades for the next operation phase, it aims to uphold a plasma for 30 minutes, confirming the ability of stellarators to operate for long pulses in steady state, as is desirable for a power-plant.

Fig. 2.11 shows the coils configuration (blue) and plasma shape (yellow) for W7X. Fig. 2.12 shows the 5 different coil types and the trim coils (A,B) to modify the magnetic field for further studies.

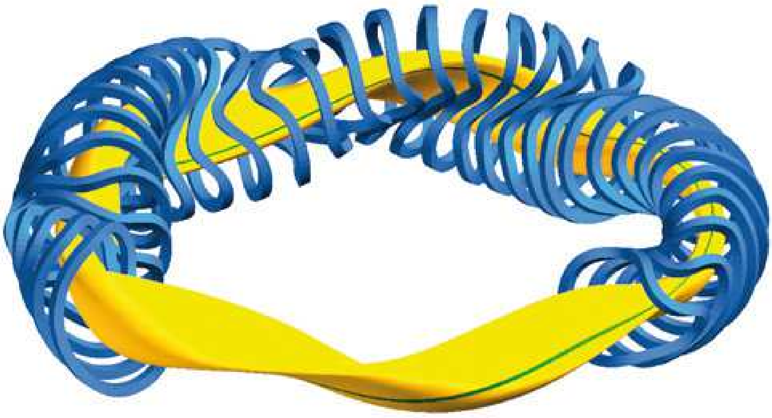

Figure 2.11: Coil configuration (blue) and resulting plasma shape (yellow) for the W7X experiment in Germany. [38]

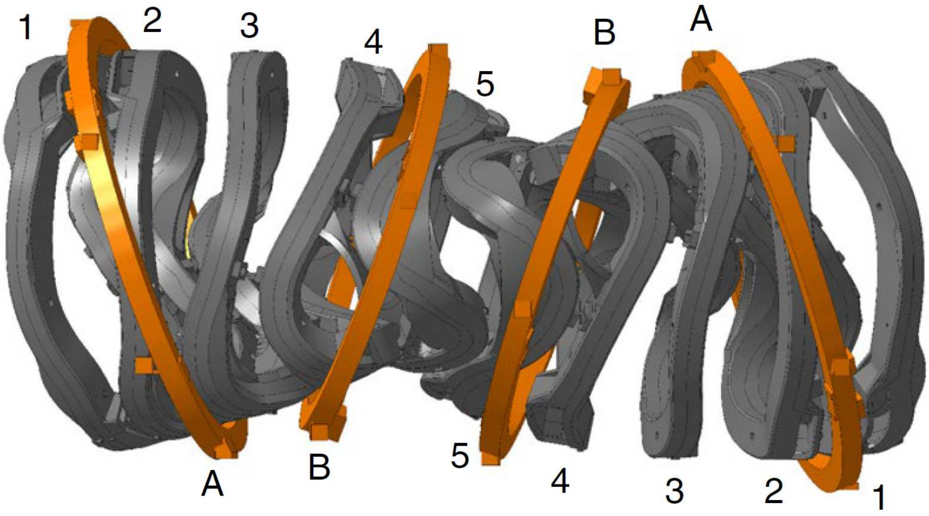

Figure 2.12: Close-up on the 5 different coil types used in W7X. The trim coils A,B allows variation of the magnetic field for scientific purposes. [39]

2.3.3. Plasma Heating

The fusion cross-section σ_{fus} is a measure of probability of a fusion process (section 2.4.1). It is typically very low (see Fig. 2.14), but has a maximum at temperatures of 10-100 keV (corresponding to temperatures of $10^8 \leq T \leq 10^9$ K). A high σ_{fus} is necessary to ensure many fusion reactions per unit time.

To reach such high temperatures, several different heating techniques must be applied, depending on the type of reactor and the temperature range where the technique is applied. [40]

Ohmic heating This technique can only be used in tokamaks. It uses ohmic losses due to the finite electrical resistivity η of the plasma. Whilst this heating mechanism is ideal for heating (almost all 'lost' energy is used for heating), the resistance of the plasma η decreases with increasing temperature: [41]

$$\eta \propto T_e^{-3/2}, \tag{2.23}$$

and hence the plasma can't be heated indefinitely. With ohmic heating, temperatures up to a few keV can be reached.

Cyclotron resonant heating A different method to heat a plasma is by using electromagnetic waves at a frequency coinciding with the gyro-frequency Ω_c of the particle (eq. 2.10): [42]

$$\omega_{wave} = \frac{l\Omega_c}{\gamma} + k_{||}v_{||}. \tag{2.24}$$

Here, l is the harmonic number, γ is the relativistic factor of the particle (≈ 1 for CNT) and the term $k_{||}v_{||}$ accounts for the Doppler-shift for moving charges.
If eq. 2.3.3 is fulfilled (for any harmonic number l), the wave may transfer energy to the particle. Since the cyclotron frequency depends on the particle mass, it is different for each particle type and therefore different radiation sources are necessary to heat different particle species. In the case of **E**lectron **C**yclotron **R**esonant **H**eating (ECRH), radiation is injected to heat the electrons, which then transfer energy to the ions via collisions. For fusion-relevant plasmas with on-axis magnetic fields of 3-5 T, the frequency of the electromagnetic radiation to heat electrons is in the range of (84-140) GHz. Additional heating can be provided by **I**on **C**yclotron **R**esonant **H**eating (ICRH).

Electromagnetic waves can only enter a plasma if their frequency is above the oscillating frequency of the electron in the plasma (eq. 2.5). The cut-off is reached when the plasma oscillates at the same frequency as the incident waves $\omega_{wave} = \omega_p$, hindering their propagation in the plasma. From eq. 2.4, a critical density n_{cutoff} can be deduced:

$$n_{cutoff}(\omega_{wave}) = \frac{\varepsilon_0 m_e}{e^2}\omega_{wave}^2 \tag{2.25}$$

Above this density, wave heating is only possible after mode-conversion of the waves (section 2.6).

Neutral beam injection A third important heating mechanism is the injection of a beam of highly energetic neutral particles (**N**eutral **B**eam **I**njection (NBI)). Here, atoms are first ionized and then accelerated using electric fields. After reaching a certain energy, they are neutralized and fed to the plasma via specific ports. The process of neutralization is necessary as otherwise the hot ions would be deflected from the magnetic field inside the device, preventing them from reaching the core of the plasma. A sketch of a typical NBI-setup and its coupling to the plasma is shown in Fig. 2.13.

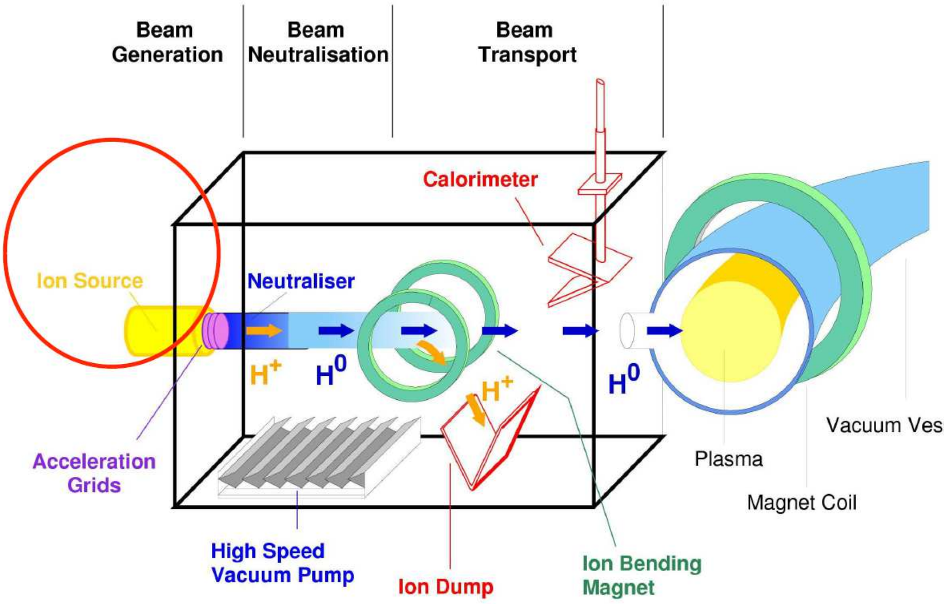

Figure 2.13: Setup of a NBI. Ions are created and accelerated before being neutralized again and fed to the plasma via ports. [43]

Typically, NBI is only used in bigger devices.

2.4. Criteria for a nuclear fusion plant

2.4.1. Fusion process

Two positively charged ions repel each other. Only if they move very fast (relative to each other) can they come close enough for short-ranged, attractive nuclear forces to act. The cross-section σ is a measure for the probability of a process (see section 2.5.1). It usually varies with the center-of-mass energy, $\sigma = \sigma(E)$. The fusion cross-section σ_{fus} for various fusion processes as a function of the relative energy between the two particles is shown in Fig. 2.14.

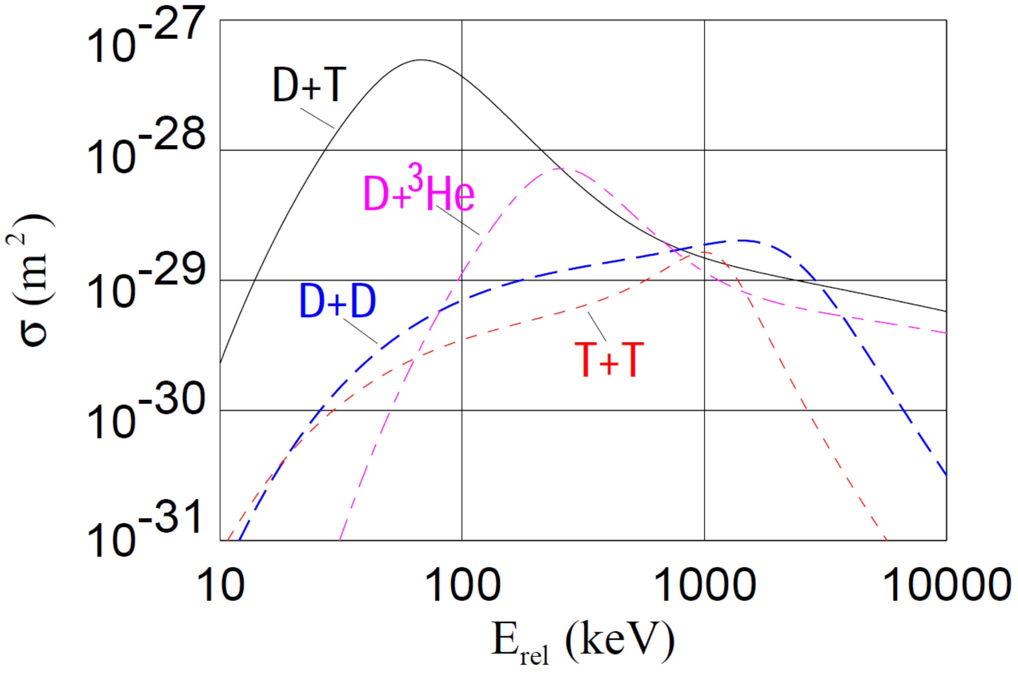

Figure 2.14: Various fusion cross sections σ_{fus} as a function of the relative energy of the two constituent particles. [44]

Fig. 2.14 highlights a few key points. σ_{fus} is typically very small, even at very high energies/temperatures. The substantially higher cross section for the process of DT-fusion is one of the key reasons why it is currently the most promising process for terrestrial use.

Assuming a thermal plasma (particles follow the Maxwell-Boltzmann distribution), a *reaction parameter* (eq. 2.39) can be defined as the product of the cross-section and the velocity, averaged over the distribution function. Fig. 2.15 shows the reaction parameter $< \sigma v >$ as a function of the (plasma) temperature. Once again it is obvious that the DT-fusion is more likely than other alternatives.

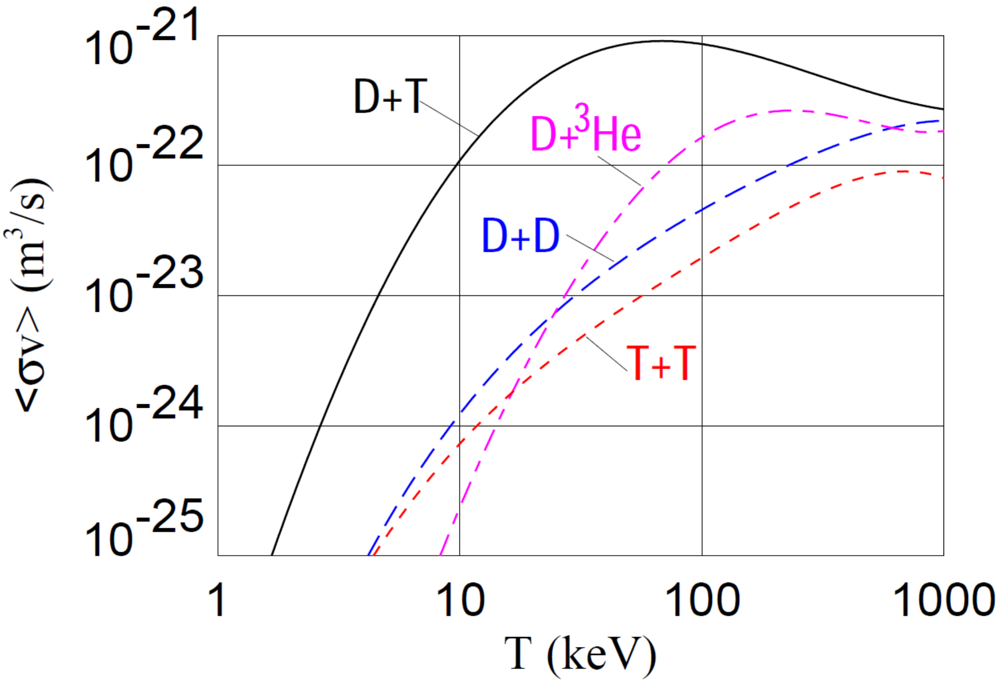

Figure 2.15: Reaction parameter as a function of the temperature. [44]

Using the reaction parameter $< \sigma v >$, the volume rate f, giving the reactions per unit volume and unit time, can be defined:

$$f = n_1 n_2 < \sigma v > \tag{2.26}$$

with n_1 and n_2 being the particle densities partaking in the process.

2.4.2. Lawson criterion

In 1955, British scientist John D. Lawson lay the groundwork to evaluate the technical and economical feasibility of a fusion power plant. [45] He looked at the energy balance of a reactor, comparing the energy gain from fusion processes to the energy sinks present in the system:

$$P_{net} = \eta \cdot (P_{fus} - P_{radiation} - P_{conduction}), \tag{2.27}$$

where P_{net} is the net power produced, P_{fus} is the power from fusion processes, $P_{radiation}$ is the power loss due to Bremsstrahlung effects and $P_{conduction}$ is the power lost due to thermal conduction. η is the efficiency with which the system can convert the fusion power into electric energy.

The confinement time τ_E of a reactor relates the energy confined within the plasma W to the power loss P_{loss}:

$$\tau_E = \frac{W}{P_{loss}} \tag{2.28}$$

It is the time after which the energy W drops to $\frac{1}{e}$ of its initial value after external heating is deactivated.

Assuming the particles to follow the Maxwell-Boltzmann distribution, the energy contained in the plasma can be estimated as:

$$W = 3nk_BT. \tag{2.29}$$

A reactor will be self-sustaining if the power used to heat the plasma will be bigger than the power lost:

$$P_{fus} \geq P_{loss}. \tag{2.30}$$

The fusion power can be obtained by multiplying the volume rate (eq. 2.26) with the energy gain per fusion reaction.

Deriving for DT-fusion and assuming a ratio of 1 Deuterium particle per Tritium particle, the densities will be (due to quasi-neutrality):

$$n_D = n_T = \frac{n_e}{2}. \tag{2.31}$$

In the case of DT-fusion, only the produced α-particle will contribute to the plasma heating (the neutron can be captured for external electricity conversion).

Plugging the definitions into eq. 2.30 and rearranging the terms eventually gives the Lawson-criterion:

$$n\tau_E \geq \frac{12}{E_{fus}} \frac{k_BT}{<\sigma v>}. \tag{2.32}$$

Note that eq. 2.32 is only valid for specific temperatures. Multiplying by the temperature gives a more significant criterion, the *triple product*:

$$nT\tau_E \geq \frac{12_B}{E_{fus}} \frac{T^2}{<\sigma v>}. \tag{2.33}$$

Fig. 2.16 shows the triple-product as a function of the (ion) temperature (blue lines). It has a minimum at around $(10-50)\ keV$, which corresponds to a temperature of roughly $10^8\ K$. Some TOKAMAK experiments are included in the plot as well. The reactor-like conditions section marks the section of temperatures and densities achievable in terrestrial devices.

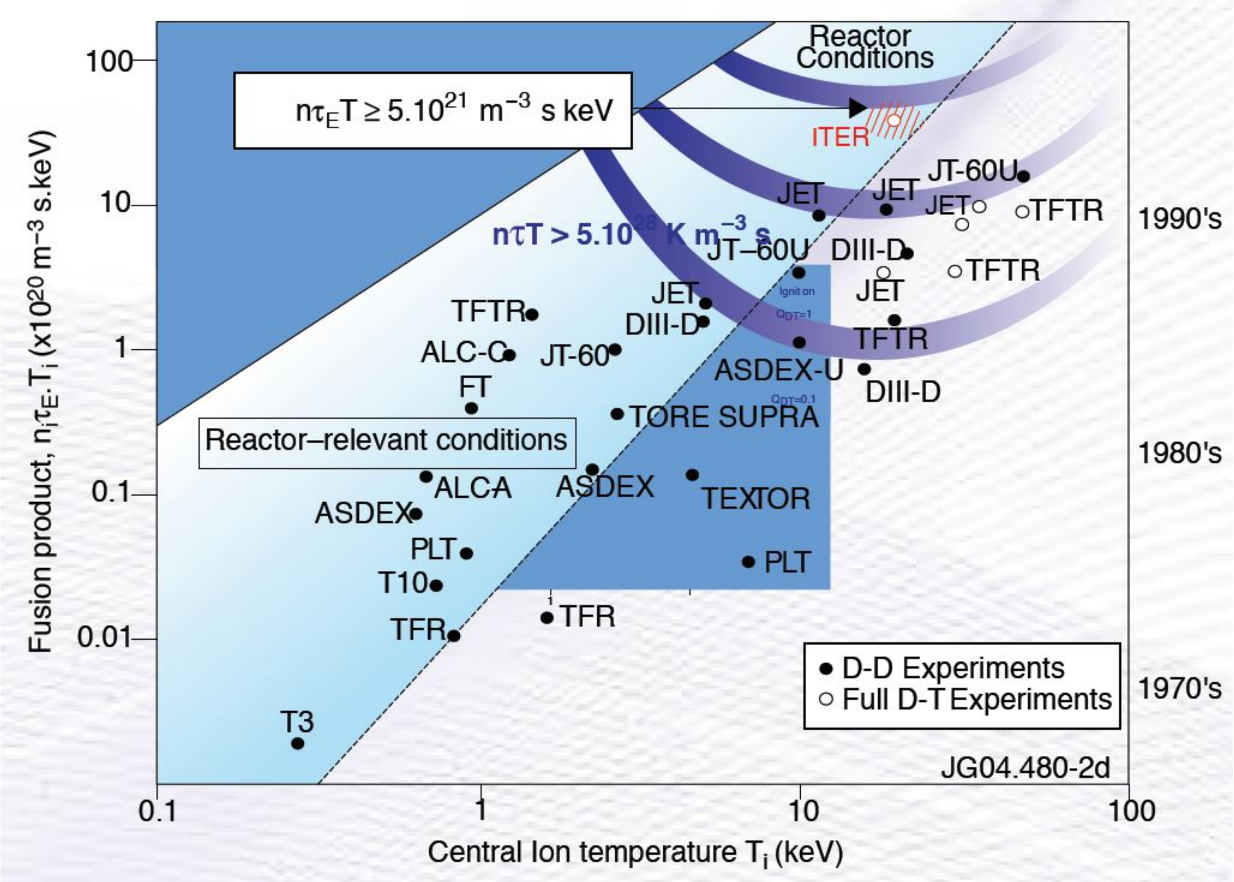

Figure 2.16: Triple product $nT\tau_E$ as a function of plasma temperature. Milestone experiments have been marked in this plots. [34]

The *fusion energy gain factor* Q relates P_{fus} to the power needed to upkeep the plasma P_{aux}. P_{aux} contains the power to uphold the magnetic field and diagnostics, (additional) heating and other auxiliaries.

$$Q = \frac{P_{fus}}{P_{aux}}. \tag{2.34}$$

If $Q = 1$, a reactor has reached the *break even point.* If the heating from the fusion α-particles alone is sufficient to heat the plasma, $Q \to \infty$ and the reactor is said to be *ignited.*

ITER aims to have $Q \geq 10$, [46] for a plant to be economically viable a factor of $30 \leq Q \leq 50$ is necessary. [25]

2.5. Particle interactions

Particles in a plasma partake in a variety of different interactions with each other. This section gives an overview with an emphasis on the ones used in this thesis.

2.5.1. Characterizing quantities for collisions

The concept of a cross-section is widely used in various descriptions of particle interactions. It can be visualized as follows: A particle travelling through a gas of (static) other particles will see an *effective* area per particle of $\sigma = \pi r^2$, r being the radius of the second particle species. The total cross-section is the sum of all individual particle cross-sections in a specific area. Fig. 2.17 illustrates the concept of this classical cross-section.

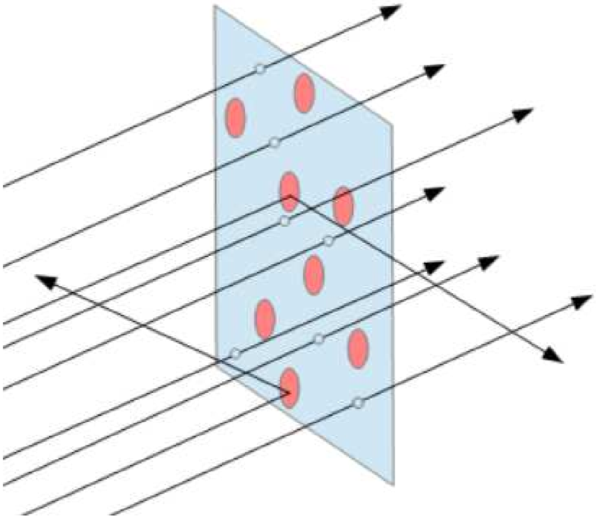

Figure 2.17: The cross-section of a specific process is the effective area (of all involved particles) seen by a particle travelling through a specified volume. [47]

σ thus is a measure of the probability of a process to happen. The cross-section typically depends on the particle's energy and is usually measured in units of *barn* (b): $1\, b = 10^{-22}\, m^2$. It is usually determined experimentally for specific processes.

The concept of a cross-section is closely related to the mean free pathlength λ_{mfp}. It gives the (average) distance a particle will travel between two subsequent collisions and has the dimension of length. It is defined as:

$$\lambda_{mfp} = \frac{1}{n_B \sigma} \tag{2.35}$$

with n_B being the density of the second particle species.

The collision frequency ν_A of particle species A with a second species B (assumed to be at rest) is given by:

$$\nu_A = n_B \sigma v_A \tag{2.36}$$

with v_A being the velocity of particle A. If both particles are at motion at the same time, the relative velocity between two particles is needed; however, for many applications, the motion of the second particle can be neglected. The collisional frequency gives the number of events experienced by a single particle per unit time.

The relaxation time is the inverse of ν_A and denotes the (average) time passing in between two collisions:

$$\tau_A = \frac{1}{\nu_A} = \frac{1}{n_B \sigma v_A}. \tag{2.37}$$

The reaction rate ω gives the number of events per unit volume and unit time:

$$\omega_{A+B} =< \sigma v > n_A n_B, \tag{2.38}$$

with $< \sigma v >$ being the reaction rate coefficient (eq. 2.39). It is defined using the (energy-dependent) cross-section $\sigma(v)$ as well as the velocity distribution $f(v)$ and integrating over a range dv:

$$< \sigma v >= \int f(v)\sigma(v)dv. \tag{2.39}$$

2.5.2. Elastic collisions

Typically, there are three different types of particles in a plasma: negatively charged electrons e^-, positively charged ions I^+ and neutral atoms (N^0). A collision between any two constituents is theoretically possible; however, in a plasma, the interaction is usually between charged particles due to the long-ranging Coulomb-force rather than head-on collisions.

The Coulomb-interaction between two charged particles depends on the relative distance between the two particles $r = |\vec{r_1} - \vec{r_2}|$. The Lagrangian of the system is given by [48]:

$$\mathcal{L} = \frac{m_1 \vec{v_1^2}}{2} + \frac{m_2 \vec{v_2^2}}{2} - U(r) \tag{2.40}$$

with $\vec{r_{1/2}}$ and $\vec{v_{1/2}}$ being of the position/velocity of the two particles.

Specifically if both particles are in motion, the **C**enter of **m**ass **s**ystem (CMS) (where $\sum_i \vec{p_i} = 0$) is a more adequate way to describe the interaction. A sketch comparing the lab system to the CMS is shown in Fig. 2.18.

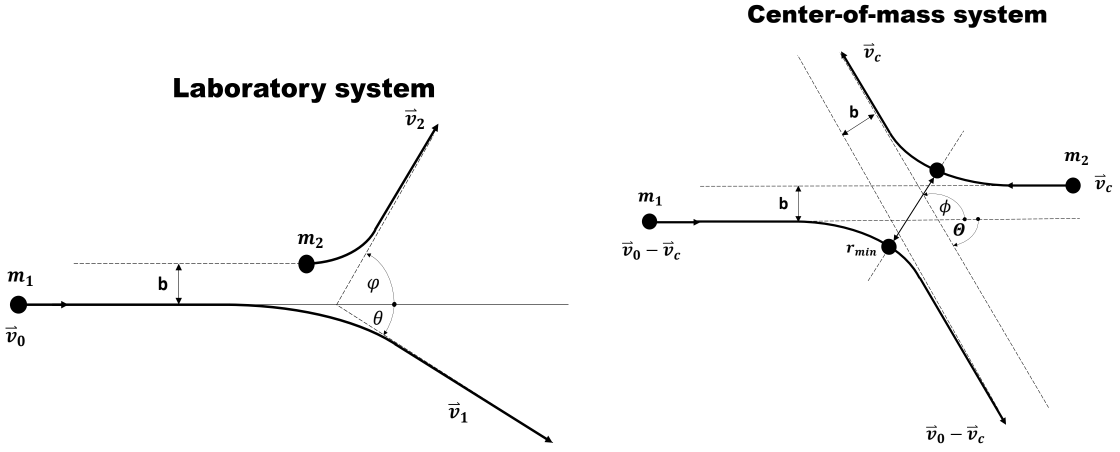

(a) Particle scattering in lab frame. **(b)** Particle scattering in Center-of-mass frame.

Figure 2.18: Schematic of particle interaction in the lab system and the **C**enter of **m**ass **s**ystem. Two interacting particles with masses m_1, m_2 will be scattered due to interaction with each other. The scattering angles φ, θ (lab-frame) and ϕ, Θ (CMS) will depend on the particles masses and the type of interaction.

The velocity and the position in the CMS are given by:

$$\vec{R} = \frac{m_1\vec{r_1} + m_2\vec{r_2}}{m_1 + m_2} \tag{2.41}$$

$$\vec{V} = \frac{m_1\vec{v_1} + m_2\vec{v_2}}{m_1 + m_2}. \tag{2.42}$$

Assuming the CMS to be at rest at the start, the Langrangian thus becomes:

$$L = \frac{\mu\dot{\vec{r}}^2}{2} - U(r) \tag{2.43}$$

and has the functional form of a single particle Lagrangian (with $\mu = \frac{m_1 m_2}{m_1+m_2}$ being the reduced mass).

In the CMS, the scattering can be described as the center of mass being scattered by a static potential. By computing the velocity of the center of mass after the collision, $\vec{V}'$, the velocities of the single particles after the collisions are:

$$\vec{v}_1' = \frac{m_2}{m_1 + m_2}\vec{V}' + \vec{V} \tag{2.44}$$

$$\vec{v}_2' = -\frac{m_1}{m_1 + m_2}\vec{V}' + \vec{V} \tag{2.45}$$

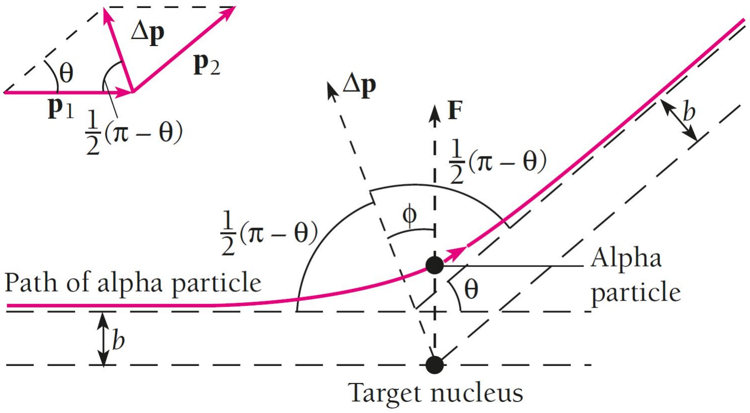

Figure 2.19: Schematic of the Rutherford scattering. The scattering angle θ of an incoming charged particle can be calculated as a function of the impact parameter b. [50]

Fig. 2.19 shows a situation where an incident α-particle is scattered by a (heavy) static target nucleus. The target is assumed to be at rest before the collision and the relative velocity is $\vec{v_{rel}} = \vec{v_1} - \vec{v_2} \approx \vec{v_2}$. Due to its significantly heavier mass, the target can be assumed to be at rest even after the collisions. The trajectory of the incoming particle however will be slightly scattered. Originally proposed by Ernest Rutherford to explain his famous gold leaf experiment [51], the model is known as Rutherford scattering model.

The model can be used in cases where one particle is significantly heavier than the other (as for electron-ion collisions) as well as to describe the scattering of the center of mass particle by a static potential.

Defining the *impact parameter* b as the distance of closest approach in a case where the particles would not be interacting (see Fig. 2.19), this scattering angle θ can easily be calculated: [52]

$$\theta = |\pi - 2\Phi| \tag{2.46}$$

$$\Phi = \int_r^\infty \frac{\frac{b}{r^2}}{\sqrt{1 - \frac{b}{r^2} - \frac{U(r)}{E_\infty}}}, \tag{2.47}$$

with $E_\infty = \frac{mv_\infty}{2}$ the particles kinetic energy before the collision; at infinite distance from the scattering center. For charged particles, the potential responsible for the interaction is the Coulomb potential U_c:

$$U_c(r) = \frac{\alpha}{r} = \frac{Q_1 Q_2}{4\pi\varepsilon_0}\frac{1}{r}, \tag{2.48}$$

with Q_1/Q_2 being the charge of the incoming/scattering particle and ε_0 the vacuum permittivity. With this potential, the integration of eq. 2.47 is elementary and the result yields: [52]

$$\Phi = cos^{-1}\left(\frac{\frac{\alpha}{2bE_\infty}}{\sqrt{1+\left(\frac{\alpha}{2bE_\infty}\right)^2}}\right). \tag{2.49}$$

In the elastic Rutherford scattering, energy can be transferred between the two constituent particles. Being an elastic collisions, the total momentum, (kinetic) energy and angular momentum are conserved. However, energy can be transferred between the two constituent particles. This energy transfer depends on the scattering angle θ:

$$\frac{E_1' - E_1}{E_1} = \frac{dE}{E_1} = \frac{4m_1m_2}{(m_1+m_2)^2}sin^2(\frac{\theta}{2}). \tag{2.50}$$

It can be seen immediately from eq. 2.50 that the energy transfer for electron-ion collisions is substantially lower than for collisions with particles of same mass (due to $m_{ion} >> m_e$).

The Rutherford model is a 2D-model. To account for 3D-effects, an additional polar scattering angle $0 \leq \varphi \leq 2\pi$ is necessary, describing where in space the scattering particle will be in relation to the test particles motion. Fig. 2.20 visualizes these 3D-effects: A particle, initially in the z-direction $\vec{v} = v\hat{e}_z$ will be scattered by the scattering angle (χ in the figure) and polar angle (ϕ in the figure).

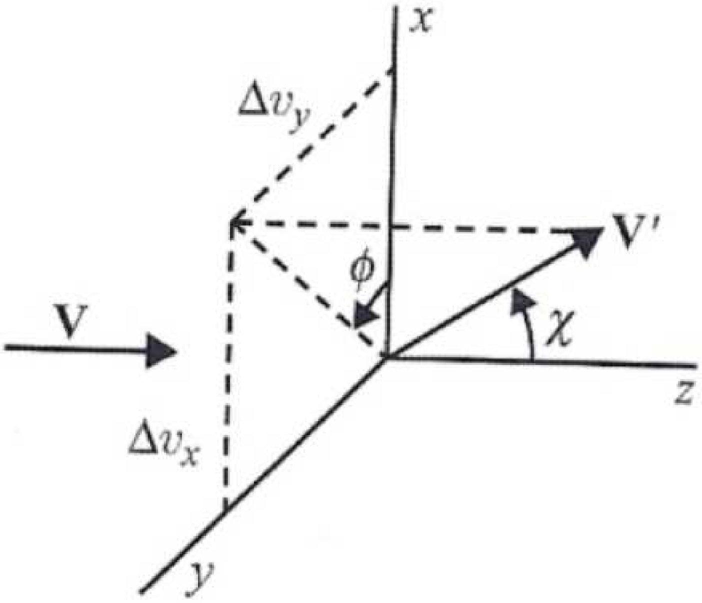

Figure 2.20: Coordinate system used to describe 3D-scattering. The scattering angle χ depends on the impact parameter, the angle ϕ depends on the position of the scattering particle in space. [25]

Fokker-Planck A particle in a plasma will undergo many small-angle Coulomb collisions (rather than single head-on collisions), altering its trajectory. This is sketched in Fig. 2.21.

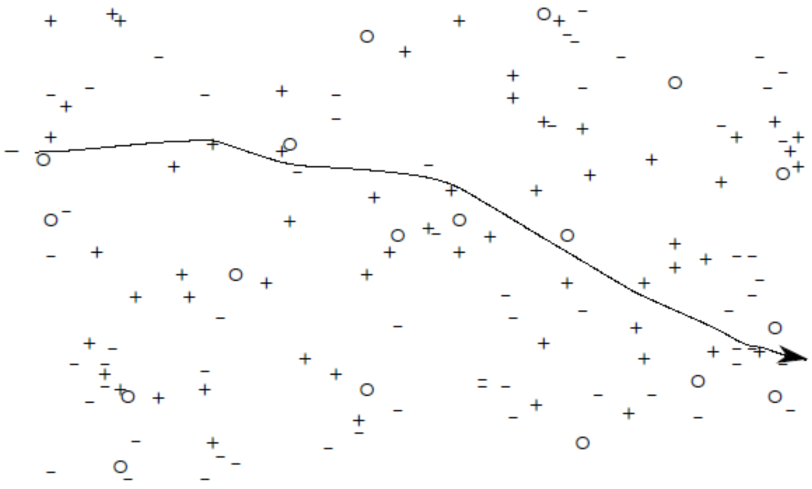

Figure 2.21: Schematic of a test particle trajectory in a plasma with electrons (-), positive ions (+) and neutral (circles). The trajectory will be altered as a consequence of many, small angle Coulomb collisions. [53]

The results of any *single* collision will be random. The change in either direction perpendicular to the direction of motion (assumed to be $\hat{e}_z$) over time will be:

$$\frac{<(\Delta v_x)>}{\Delta t} = \frac{<(\Delta v_y)>}{\Delta t} = 0. \tag{2.51}$$

The square will be non-zero however:

$$\frac{<(\Delta v_x)^2>}{\Delta t} = \frac{<(\Delta v_y)^2>}{\Delta t} \neq 0. \tag{2.52}$$

This implies diffusive properties, namely the particle being scattered in velocity space, converting its parallel component ($v_z = v_{||}$) gradually into a component perpendicular to its path $v_\perp$. In addition to the diffusion, a particle will experience drifts due to collisions, slowing the particle down (by transferring energy, eq. 2.50). Treating particles under these influences is known as *Fokker-Planck* (FP) approach.

The (average) velocity change over time is given by:

$$\frac{<(\Delta \vec{v})>}{\Delta t} = \frac{<(\Delta v_{||})>}{\Delta t}\hat{e}_z = -\nu_s(v)\vec{v} \tag{2.53}$$

$$\frac{<(\Delta \vec{v}\Delta \vec{v})>}{\Delta t} = \frac{1}{2}\frac{<(\Delta v_\perp)>}{\Delta t}(\hat{e}_x\hat{e}_y + \hat{e}_y\hat{e}_y) = \nu_{diff}(v)(v^2\mathbb{1}_3 - \vec{v}\vec{v}), \tag{2.54}$$

where $\nu_s(v)$ is a slowing-down rate and $\nu_{diff}(v)$ is the diffusion rate.

Assume a background species s', with the particles following the Maxwellian-distribution $f_{s'}(v)$:

$$f_{s'}(v) = \left(\frac{m_{s'}}{2\pi T_{s'}}\right)^{3/2} e^{-m_{s'}v^2/(2T_{s'})}, \tag{2.55}$$

with $m_{s'}$ being the particle species mass and $T_{s'}$ the temperature. A test particle of species s moving through this background will experience a change in velocity: [53]

$$\frac{d}{dt}(m_s\vec{v}) = -\nu_s^{s/s'} m_s\vec{v} \tag{2.56}$$

$$\frac{d}{dt}|\vec{v}-\bar{\vec{v}}|_\perp^2 = \nu_\perp^{s/s'} v^2 \tag{2.57}$$

$$\frac{d}{dt}|\vec{v}-\bar{\vec{v}}|_{||}^2 = \nu_{||}^{s/s'} v^2. \tag{2.58}$$

Eq. 2.56 is the momentum lost by the test particle, the other two equations describe its diffusion in velocity space. $|\vec{v}-\bar{\vec{v}}|^2$ is the diffusional spread tensor for the test particle in the respective direction. The rates $\nu_s^{s/s'}, \nu_\perp^{s/s'}$ and $\nu_{||}^{s/s'}$ are given by:

$$\nu_s^{s/s'} = -\left[\left(1+\frac{m_s}{m_{s'}}\right)\psi(x)\right]\nu_0^{s/s'} \tag{2.59}$$

$$\nu_\perp^{s/s'} = 2\left[\psi(x)+\psi'(x)-\frac{\psi(x)}{2x}\right]\nu_0^{s/s'} \tag{2.60}$$

$$\nu_{||}^{s/s'} = \left[\frac{\psi(x)}{x}\right]\nu_0^{s/s'}, \tag{2.61}$$

where $\psi(x)$ is the Maxwell-integral:

$$\psi(x) = \frac{2}{\sqrt{\pi}}\int_0^x dt\sqrt{t}e^{-t} \tag{2.62}$$

$$\psi'(x) = \frac{d\psi(x)}{dx} = \frac{2}{\sqrt{\pi}}\sqrt{x}e^{-x}. \tag{2.63}$$

The argument $x = \frac{v^2}{v_{T_{s'}}^2}$ here is the relative speed parameter. The standard collisional frequency $\nu_0^{s/s'}$ is given by:

$$\nu_0^{s/s'} = \frac{4\pi n_{s'} q_s q_{s'}}{(4\pi\varepsilon_0)^2 m_s^2 v_{T_{s'}}^3} ln\Lambda_{s/s'}. \tag{2.64}$$

The Coulomb-logarithm $ln\Lambda_{s/s'}$ relates the minimum and maximum possible impact parameters:

$$ln\Lambda_{s/s'} = \int_{b_{min}}^{b_{max}} \frac{db}{b} = ln(\frac{b_{max}}{b_{min}}). \tag{2.65}$$

The integral would diverge for both $b \to 0$ and $b \to \infty$. Out of physical considerations, the upper limit is typically chosen as

$$b_{max} = \lambda_D, \tag{2.66}$$

since for distances $d > \lambda_D$ the potential is effectively shielded and the particle will feel no force. The minimum impact parameter is where the Coulomb potential energy equals the particles kinetic energy, leading to a full 90°deflection of the particle:

$$b_{min} = \frac{Z_i e^2}{4\pi\varepsilon_0(m_s v_s^2)}. \tag{2.67}$$

For typical fusion-relevant plasmas, the Coulomb-logarithm usually takes on values $15 \leq ln\Lambda \leq 25$.

The energy loss rate of a particle can be described as a combination of the other processes:

$$\nu_E^{s/s'} = 2\left[\frac{m_s}{m_{s'}}\psi(x) - \psi'(x)\right]\nu_0^{s/s'} = 2\nu_s^{s/s'} - \nu_\perp^{s/s'} - \nu_{||}^{s/s'} \tag{2.68}$$

$$\frac{d}{dt}E_s = -\nu_E^{s/s'} E_s. \tag{2.69}$$

If a test particle collides with several particle species simultaneously, the total rate is the sum of the single rates, e.g.:

$$\nu_s^{tot} = \sum_{s'} \nu_s^{s/s'}. \tag{2.70}$$

2.5.3. Inelastic collisions

Contrary to elastic collisions, the kinetic energy is not conserved for inelastic collisions. A fraction of the kinetic energy is converted into other forms of energy, e.g. to excite or ionize atoms or molecules. The most important mechanism for a self-sustaining plasma is the process of ionization. Other inelastic collision processes include excitation of molecules, neutral and ionized atoms or the dissociation of molecules. Electrons can also be lost from the plasma due to recombination with ions or due to attachment of electrons to neutrals. [55, 54]

Ionization In the event of an ionization collision, an incoming electron removes an electron from an inner shell of the target atom, ionizing it:

$$e^- + N^0 \rightarrow e^- + e^- + I^+.$$

The ionization energy E_{ion}, which needs to be supplied by the incoming electron to release a bound electron, is the binding energy of the electron to be released. The total energy after the process is:

$$E_{tot} = E'_{inc} + E'_{ej} + E_{ion} = E_{inc} \tag{2.71}$$

and is equal to the energy of the incident electron before the process. The electron loses the ionization energy E_{ion} and the remaining energy is split up between the incident electron (after ionization) E'_{inc} and the electron ejected from the atom E'_{ej}.

In CNT, which is filled with nitrogen gas, the ionization energy of nitrogen molecules N_2 is the most common process; as opposed to ionization of single nitrogen atoms N. The ionization energy of nitrogen is $E_{ion,N_2} = 15.6\ eV$. [54]

Ionization processes are usually complex 3-body systems and cannot easily be solved analytically. An approach to include ionization processes in this work is presented in section 3.2.9.

Electron recombination Recombination processes are an important particle loss mechanism in plasmas. An electron e^- colliding with a positively charged ion I^+ can recombine:

$$e^- + I^+ \rightarrow N^0.$$

The change in particle density in a plasma after heating has been deactivated is known as the *afterglow*. It can be formulated as: [57]

$$\frac{dn}{dt} = -\alpha n_e n_i - \frac{n}{\tau} = -\alpha n^2 - \frac{n}{\tau}, \tag{2.72}$$

where α is the recombination coefficient and τ is the exponential decay time. In the case of a quasi-neutral plasma, the density of electrons and (singly charged) ions is the same $n_e = n_i = n$.

2.6. Electromagnetic waves in a plasma

2.6.1. Wave equation and vacuum solution

The electromagnetic field carried by photons can be derived by solving the Maxwell-equations in vacuum. This leads to a wave-equation for both the electric and magnetic field components of the form:

$$(\vec{\nabla}^2 - \frac{1}{c^2}\frac{\partial^2}{\partial t^2})\vec{E} = \Box\vec{E} = 0, \tag{2.73}$$

with the d'Alembert-operator

$$\Box = \frac{1}{c^2}\frac{\partial^2}{\partial t^2} - \vec{\nabla}^2.$$

One possible solution for eq. 2.73 is using plane waves, where the electric $\vec{E}$ and magnetic $\vec{B}$ fields are given by:

$$\vec{E}(\vec{r},t) = \vec{E}_0 e^{i(\vec{k}\cdot\vec{r}-\omega t+\varphi)} \tag{2.74}$$

$$\vec{B}(\vec{r},t) = \vec{B}_0 e^{i(\vec{k}\cdot\vec{r}-\omega t+\varphi)}. \tag{2.75}$$

Here, $\vec{k}$ is the wave-vector of the wave which points in its direction of propagation; $\omega = 2\pi f$ is the waves' angular frequency, φ is an (optional) phase and $\vec{E}_0/\vec{B}_0$ are the amplitude vectors. The angular frequency and the wave number $k = |\vec{k}|$ are related by the dispersion relation:

$$\omega = c|\vec{k}|, \tag{2.76}$$

with c the speed of light.

Both the electric as well as the magnetic field are perpendicular to the wave vector $\vec{k}$, forming a full triad:

$$\vec{E}\perp\vec{k}\perp\vec{B}. \tag{2.77}$$

2.6.2. Wave propagation in a plasma

To describe how a wave propagates in a plasma, a derivation for a cold plasma will be used. In this model, the thermal movement of the constituent particles is neglected and their distribution function is described using Dirac-functions. [25] For most applications this model is sufficient.

The dispersion relation, which for plane waves in vacuum was given by eq. 2.76, is more complicated inside a plasma and can be derived by solving the Maxwell-equations in the plasma medium. For a magnetized plasma, it can be written as: [42]

$$D(n, \frac{\omega_p^2}{\omega^2}, \frac{\Omega_{ce}}{\omega}, \Gamma) = tan^2\Gamma + \frac{P(n^2-R)(n^2-L)}{(Sn^2-RL)(n^2-P)} = 0, \tag{2.78}$$

where $n = \frac{ck}{\omega}$ is the index of refraction, ω_p is the plasma frequency (eq. 2.4), Ω_{ce} is the electron cyclotron frequency (eq. 2.10) and Γ is the angle between $\vec{k}$ and the magnetic field in the plasma $\vec{B}_0$. The other quantities are given by

$$P = 1 - \left(\frac{\omega_p}{\omega}\right)^2 \tag{2.79}$$

$$R = \frac{(P - \Omega_{ce}/\omega)}{(1 - \Omega_{ce}/\omega)} \tag{2.80}$$

$$L = \frac{(P + \Omega_{ce}/\omega)}{(1 + \Omega_{ce}/\omega)} \tag{2.81}$$

$$S = \frac{(R+L)}{2}. \tag{2.82}$$

Depending on the angle Γ, different solutions are obtained. For $\Gamma = 0$, the two solutions (for n) are:

$$n^2 = L \tag{2.83}$$

$$n^2 = R \tag{2.84}$$

and for $\Gamma = \pi/2$:

$$n^2 = P \tag{2.85}$$

$$n^2 = \frac{RL}{S}. \tag{2.86}$$

The solutions $n^2 = L$ and $n^2 = P$ are called the O-mode (*ordinary mode*) of the wave while the other solutions are called the X-mode (*extraordinary mode*) of the wave. The O-mode is characterized by the wave electric field being parallel to the background magnetic field

$$\vec{E}_w || \vec{B}_0,$$

while the X-mode is characterized by the wave electric field being perpendicular:

$$\vec{E}_w \perp \vec{B}_0.$$

The limits of propagation of the wave occur at $n^2 = 0$ (cut-off) and $n^2 \to \infty$ (resonance). At the cut-off the wave is reflected. At the resonance, since $n^2 \to \infty$, the waves' speed of propagation approaches 0 and is thus eventually absorbed by damping due to particle collisions.

For the $n^2 = L$-solution for the O-mode, the dispersion relation becomes:

$$c^2k^2 = \omega^2 - \omega_p^2. \tag{2.87}$$

In the case $\omega_p^2 > \omega^2$, the wave-number will become imaginary and the wave will evanesce quickly. Physically speaking, the electrons in the plasma oscillate fast enough to react to and cancel the incoming wave field. Typically, the cut-offs are described in terms of the cut-off density for a plasma by equating $\omega = \omega_p$, which leads to:

$$n_{co}(\omega) = \frac{\varepsilon_0 m_e}{e^2}\omega^2. \tag{2.88}$$

If a plasma is too dense for a given O-mode, the wave can only propagate after a mode-conversion, e.g. to the X-mode and eventually Bernstein waves. [58, 59]

For the corresponding X-mode, the dispersion relation becomes: [60]

$$c^2k^2 = \frac{(\omega^2 - \omega_R^2)(\omega^2 - \omega_L^2)}{(\omega^2 - \omega_{UH}^2)}, \tag{2.89}$$

with

$$\omega_R = \omega_{Right} = \frac{1}{2}(\omega_{ce} + \sqrt{\omega_{ce}^2 + 4\omega_p^2})$$
$$\omega_L = \omega_{Left} = \frac{1}{2}(-\omega_{ce} + \sqrt{\omega_{ce}^2 + 4\omega_p^2})$$

and the *upper hybrid* frequency

$$\omega_{UH} = \sqrt{\omega_{ce}^2 + \omega_p^2}.$$

If $\omega = \omega_R$, there is a *right-handed cutoff* and the wave is evanescent until $\omega = \omega_{UH}$. The wave can propagate for $\omega > \omega_{UH}$ until it reaches the *left-handed cutoff* at $\omega = \omega_L$. [61]

Cyclotron resonance: The theory of *cyclotron resonance* cannot be described using the cold plasma approach, since the particles are required to be in motion.

Charged particles spiral around magnetic field lines with their cyclotron frequency Ω_c (eq. 2.10). If an electromagnetic field of the same frequency is applied,

$$\omega = \Omega_c,$$

the resulting Lorentz-force acting on the particle will lead to an increase in energy. The same also happens at higher harmonics l:

$$\omega = l\Omega_c, \tag{2.90}$$

where $l = 1, 2, 3, ...$ is the harmonic number. Due to the different charge sign of electrons and positively charged ions, heating occurs either when the particle and wave are in phase (positive sign) or out of phase (electrons).

Due to the different masses of electrons and positive ions, their cyclotron frequencies are different and consequently the frequency of injected waves differs depending on which particle type one wants to heat.

3. Method

3.1. Influence of wave-electric field on emission current

The first candidate mechanism presented in section 1.4 was the enhancement of the emission current from the filament in the presence of the wave electric field. The current density $j = \frac{I}{A}$ ejected from a heated filament as a function of its temperature T and the effective electric field strengths $E = |\vec{E}|$ is given by: [62]

$$j(E,T) = BT^2 exp\left(-\frac{\Phi}{k_BT} + \frac{\sqrt{\frac{e^3E}{4\pi\varepsilon_0}}}{k_BT}\right), \tag{3.1}$$

where B is a material parameter and Φ is the material's work function. For the tungsten filaments used in the experiments, the material parameter is: [63]

$$B \approx 0.4\ \frac{A}{mm^2K^2}$$

and the work function: [64]

$$\Phi \approx 4.5\ eV.$$

As a first approach, the maximum possible influence of the wave electric field on this mechanism is investigated. The amplitude of a (wave) electric field E_0 is proportional to its intensity I: [74]

$$|E_0| = \sqrt{\frac{2I}{c\varepsilon_0}}, \tag{3.2}$$

with c being the speed of light. The microwaves enter the vessel through a cylindrical port with an effective radius of $r \approx 12.5\ cm$. Assuming all of the power of the magnetron ($P \approx 1,000\ W$) actually enters the vessel, the electric field amplitude created by the microwaves (right behind the entry port) was found to be:

$$|E_{0,max}| = \sqrt{\frac{2I}{c\varepsilon_0}} = \sqrt{\frac{2}{c\varepsilon_0} \cdot \frac{P}{r^2\pi}} \approx 3.9 \cdot 10^3\ \frac{V}{m}. \tag{3.3}$$

To put this in perspective to the emission current in absence of the microwaves, we still need (estimates of) the temperature of the emissive filament as well as the electric field created due to the bias voltage.

The power flowing through the filament was obtained by voltage and current measurements and was determined to be $P \approx 8\ W$. The probe will heat and radiate off energy until an equilibrium state is reached. The radiated power of an object is given by the Stefan-Boltzmann-law:

$$P = A\sigma\varepsilon T^4, \tag{3.4}$$

where A is the object's surface area, σ is the Stefan-Boltzman-constant, ε is the object's emissivity ($\varepsilon = 1$ for black bodies) and T its temperature. The surface area of the probe was calculated using the measured diameter and length of the filament and was found to be $A \approx 2 \cdot 10^{-6}\ m^2$. Tungsten filaments usually have an emissivity of around $\varepsilon \approx 0.38 - 0.4$ for most wavelengths.[1] As a consequence, the filament during operation has a temperature of around

$$T = \left(\frac{P}{\sigma A\varepsilon}\right)^{1/4} \approx 3450\ K, \tag{3.5}$$

which is consistent with literature data for different halogen light-bulbs.

The next step is to get an estimate for the electric field due to the bias voltage. The applied voltage is effectively shielded by the plasma anywhere away from the sheaths right next to the electrodes (see section 2.1). An electron emitted by the filament (acting as the cathode) will thus feel a potential of $\approx -100\ V$ before it is shielded by the plasma. The other half of the potential would be felt as the electron exits the plasma and approaches the vessel wall (=anode).

The electric field created by a certain potential is proportional to its gradient:

$$\vec{E} = -\vec{\nabla} V. \tag{3.6}$$

In our case we have the potential gradient change over the sheath:

$$E_{r,sheath} = -\frac{dV}{dr} = -\frac{-100}{\lambda_D} \approx 2 \cdot 10^5 \frac{V}{m}. \tag{3.7}$$

Results of the emission current density with/without the microwave influence are presented in section 4.1.

---

[1] `http://pyrometry.com/farassociates_tungstenfilaments.pdf`

3.2. Particle Tracing

The second candidate mechanism to be studied was the enhanced absorption of microwaves by the thermo-electrons emitted from the electron gun. Due to the bias applied, these electrons have substantially higher energies (and subsequently a higher Larmor radius r_L) than the thermal background electrons. The optical depth τ, is a measure for the effectiveness of microwave absorption. For the parameter range used in CNT, it is $\tau \propto r_L$; thus more energetic electrons can absorb the microwaves more efficiently.

To quantify this effect, the trajectories of single electrons in CNT were traced. The particles will be subject to many collision events, such as:

- Elastic collisions: Collisions between the electron and other charged particles. In these collisions, the electron will be deflected and transfers energy (to the colliding partner), changing its trajectory which could eventually lead to the electron leaving confinement.
- Ionization collisions: An electron colliding with a neutral atom can results in ionizing the atom, releasing an electron in the process and thus increasing the plasma density.
- Recombination: Electrons colliding with ions can recombine and the electron is essentially lost to the plasma.

In addition, the particles can absorb energy from the electric field created by the injected microwaves.

The result of collisions are random, meaning that despite identical initial parameters, the outcome will always be different. Simulating many individual particle trajectories, an estimate of the average number of ionization events per unit time and particle can be made and thus allows a prediction of the ionization rate for the total plasma. Comparing this ionization rate (and thus density increase) to measurements of the average density loss rate allows predictions of obtainable plasma densities. If simulations with different parameters are performed, it can be assessed if the mechanism can account for the observed increase in obtainable densities. The different simulation cases are essentially:

1. Plasma start-up with microwaves only: The background electrons are assumed to have a Maxwellian energy distribution centered around $E \approx 5\ eV$. Their initial position and direction of velocity vector are chosen to be random anywhere inside the plasma volume. The particles are then exposed to the microwave electric field and traced, until one of the exit criteria (section 3.2.11) is met.

   To get an estimate how many electrons are typically subject to heating, we take the density n (as measured in Fig. 1.3) and the plasma volume V_P:

$$N = n \cdot V_P \approx 2 \cdot 10^{16}\ m^{-3} \cdot 0.3\ m^3 = 6 \cdot 10^{15}. \tag{3.8}$$

2. Start-up with electron gun: The electrons emitted from the filament have energies of $E \approx 100\ eV$. They are all emitted from the location of the heated filament, roughly:

   $$\vec{r} = \begin{pmatrix} r \cdot cos(\varphi) \\ 0.2 \\ r \cdot sin(\varphi) \end{pmatrix},$$

   where the radial distance of the probe array was varied $0.2 \leq r \leq 0.4$ and the angle was $\varphi \approx 45°$. The initial pitch-angle α is randomized and the corresponding velocity components are computed from the local direction of the magnetic field.

   In the absence of microwave heating, the tracing can basically be stopped once an electrons' energy drops below the ionization energy E_{ion} necessary for a further ionization event.

   The emission current from the filament I_{em} can be estimated from its surface area A_f and the emission current density j_{em} (Fig. 4.1):

   $$I_{em} = A_f \cdot j_{em} \approx 2\ mm^2 \cdot 1360\ \frac{mA}{mm^2} = 2720\ mA.$$

   As a consequence, roughly $N = \frac{I_{em}}{e} = 1.7 \cdot 10^{19}$ electrons are emitted per second (with e being the electrons' charge). The number of electrons and the average ionization rate allows conclusions of the obtainable densities to be made.

   It should be noted here that only a small fraction of the emitted electrons will actually be confined in the plasma for extended periods of time; typically leaving confinement after a few revolutions inside the torus.

3. Electron gun combined with microwaves: Combination of the two aforementioned cases. The ionization rate of electrons emitted from the electron gun will change, while the ionization rate of background electrons (case 1) should roughly stay constant. Adding the two ionization rates and comparing them to the rates of either method alone should enable predictions on whether the proposed mechanism can explain the synergy or not can be made.

The analysis code was written in Fortran 90 and post-processing as well as visualization was done using Python.

3.2.1. Integration method

The equations of motion (eq. 2.8 for particles, eq. 2.12 and 2.13 for the GCM) are ordinary differential equations. These are solved using a Runge-Kutta-4 (RK4)-method. [66] For an initial value problem with a time-dependent function $y(t)$, defined as

$$y(t_0) = y_0 \tag{3.9}$$
$$\dot{y} = f(t, y), \tag{3.10}$$

the solution at a later timepoint with $\Delta t = h > 0$ using this approach is:

$$y_{n+1} = y_n + \frac{1}{6}(k_1 + k_2 + k_3 + k_4) \tag{3.11}$$
$$t_{n+1} = t_n + h, \tag{3.12}$$

with $n \in \mathbb{N}_0$. The single coefficients are given by:

$$k_1 = h \cdot f(t_n, y_n) \tag{3.13}$$
$$k_2 = h \cdot f(t_n + \frac{h}{2}, y_n + \frac{k_1}{2}) \tag{3.14}$$
$$k_3 = h \cdot f(t_n + \frac{h}{2}, y_n + \frac{k_2}{2}) \tag{3.15}$$
$$k_4 = h \cdot f(t_n + h, y_n + k_3). \tag{3.16}$$

The function is thus approximated using a weighted sum of intermediate solutions, with a greater weight being given to the increments at the midpoint. Fig. 3.1 sketches the procedure for a sample function.

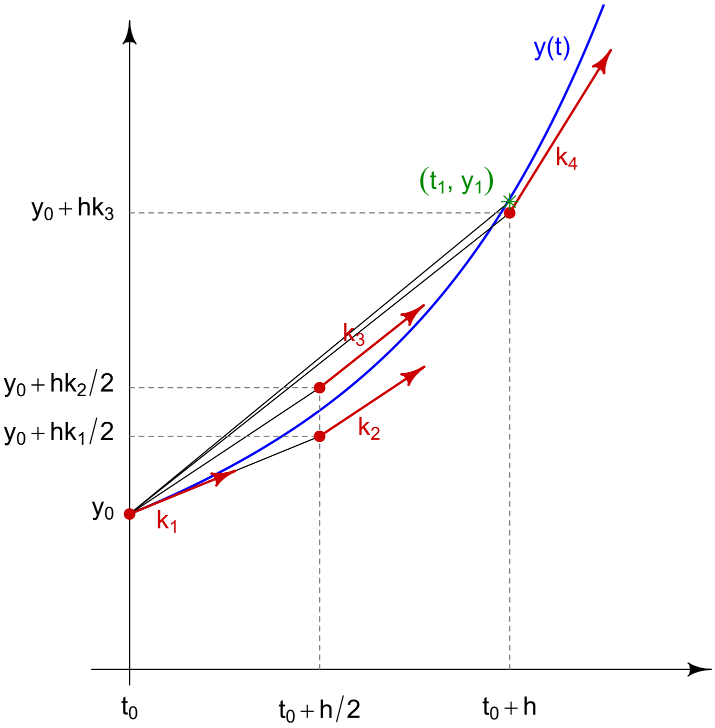

Figure 3.1: Runge-Kutta-4 integration method applied to a sample function $y(t)$. The function is shown in blue and the approximated solution $f(t_1)$ is shown in green. Intermediate RK4-steps are shown in red. [67]

3.2.2. Rotation matrices

In many applications, the solution to a problem is arithmetically easier in specific frames of reference. Rather than solving a problem in the lab frame, one can instead transform to a different reference frame, solve the problem and then transform the result back to the lab frame. For instance, collisional effects might be easier in a frame where the velocity points in the z-direction: $\vec{v} = v \cdot \hat{e}_z$. In order to transform the lab frame to this frame (and back), the rotation matrices R_x, R_y, R_z are necessary:

$$R_x(\alpha) = \begin{bmatrix} 1 & 0 & 0 \\ 0 & \cos(\alpha) & \text{-}\sin(\alpha) \\ 0 & \sin(\alpha) & \cos(\alpha) \end{bmatrix}$$

$$R_y(\beta) = \begin{bmatrix} \cos(\beta) & 0 & \sin(\beta) \\ 0 & 1 & 0 \\ \text{-}\sin(\beta) & 0 & \cos(\beta) \end{bmatrix}$$

$$R_z(\gamma) = \begin{bmatrix} \cos(\gamma) & \text{-}\sin(\gamma) & 0 \\ \sin(\gamma) & \cos(\gamma) & 0 \\ 0 & 0 & 1 \end{bmatrix}$$

.

If a rotation matrix $R_i(\varphi)$ is multiplied to a vector, the vector will be rotated about the respective axis i by the specified angle φ.

Note that the matrix multiplication is not commutative; thus when several rotations are necessary, the order needs to be considered.

3.2.3. Magnetic field

Devices such as CNT and CIRCUS [68] use solely (tilted) circular coils to create its magnetic fields. The magnetic field created by a circular coil lying in the xy-plane with radius a and current I (Fig. 3.2) is given by fairly simple analytical expressions: [69]

$$B_x = \frac{Cxz}{2\alpha^2\beta\rho^2}[(a^2+r^2)E(k^2) - \alpha^2 K(k^2)] \tag{3.17}$$

$$B_y = \frac{Cyz}{2\alpha^2\beta\rho^2}[(a^2+r^2)E(k^2) - \alpha^2 K(k^2)] = \frac{y}{x}B_x \tag{3.18}$$

$$B_z = \frac{C}{2\alpha^2\beta}[(a^2-r^2)E(k^2) + \alpha^2 K(k^2)]. \tag{3.19}$$

Here, $C = \frac{\mu_0 I}{\pi}$, μ_0 is the vaccum permeability, $\rho^2 = x^2+y^2$, $r^2 = x^2+y^2+z^2$, $\alpha^2 = a^2+r^2-2a\rho$, $\beta^2 = a^2+r^2+2a\rho$ and $k^2 = 1-\frac{\alpha^2}{\beta^2}$. x, y, z are the spatial coordinates where the magnetic field is computed. The functions $K(k^2)$ and $E(k^2)$ are the first and second (complete) elliptical integrals with argument k^2:

$$K(k^2) = \int_0^{\pi/2} \frac{d\Theta}{\sqrt{1-k^2 sin^2(\Theta)}} \tag{3.20}$$

$$E(k^2) = \int_0^{\pi/2} \sqrt{1-k^2 sin^2(\Theta)}d\Theta. \tag{3.21}$$

An example coil is sketched in Fig. 3.2.

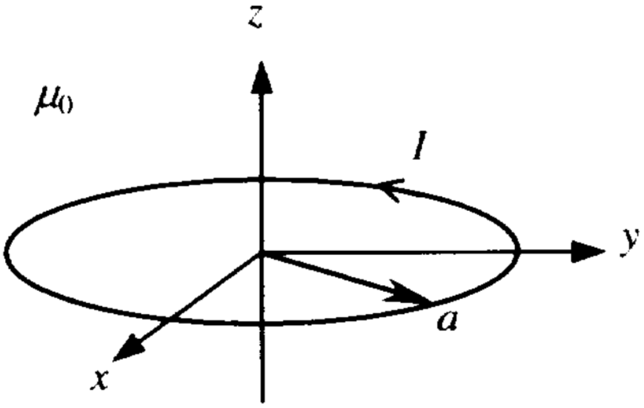

Figure 3.2: Circular coil with radius a and current I, for which the magnetic field $\vec{B}$ can easily be computed. [69]

The magnetic field of a tilted, circular coil centered at $\vec{r_C} = \begin{pmatrix} x_C \\ y_C \\ z_C \end{pmatrix}$ is obtained by computing eq. (3.17 - 3.19) with the specified parameters and then transform the resulting magnetic field vector $\vec{B}$. The tilt is obtained by rotating the result using rotation matrices (3.2.2) and the shift to the origin of the coil is obtained by simply shifting the coordinates $\vec{r}$ by the vector $\vec{r_C}$.

Fig. 3.3a illustrates the tilt of a coil about the y-axis. It is then shifted outwards to new position $\vec{r_C} = \begin{pmatrix} 0 \\ y_c \\ 0 \end{pmatrix}$. (Fig. 3.3).

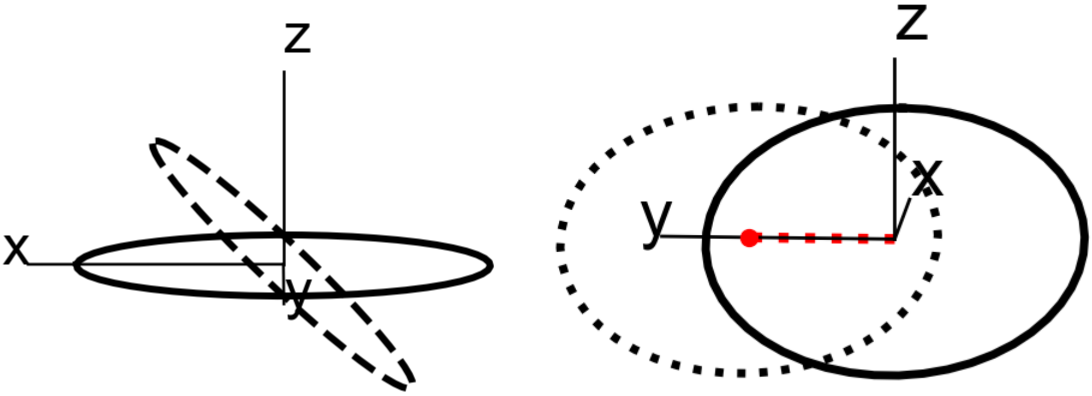

(a) An original circular coil (solid black line) is tilted about the y-axis by an angle θ (dashed black line).

(b) Shifting a tilted coil (solid black line) to a new position $\vec{r_C}$ (red dot).

Figure 3.3: Demonstration tilt/rotation of circular coils.

The IL-coils in CNT are exactly that: coils with a radius of $r_{IL} = 0.405\ m$ tilted by an angle of $\theta = 51°$ (for the synergy experiments) and shifted outwards by a distance of $y_{IL} = 0.313\ m$. The second IL-coil is a mirror image of the first. The VF-coils (with radius $r_{VF} = 1.08\ m$) are not tilted at all and are just shifted by $z_{VF} = 0.405\ m$. The parameters of the single coils are summarized in table 3.1.

Coil ID	Radius	Center position $\vec{r}_C$	Tilt	Current (kA)
IL 1	0.405 m	$\begin{pmatrix} 0 \\ 0.313 \\ 0 \end{pmatrix}$	$R_y(51\ °)$	39
IL 2	0.405 m	$\begin{pmatrix} 0 \\ -0.313 \\ 0 \end{pmatrix}$	$R_y(-51\ °)$	39
VF 1	1.08 m	$\begin{pmatrix} 0 \\ 0 \\ 0.405 \end{pmatrix}$	None	13
VF 2	1.08 m	$\begin{pmatrix} 0 \\ 0 \\ -0.405 \end{pmatrix}$	None	13

Table 3.1: CNT Coil parameters.

The current ratio C_r is the ratio of the current flowing through the IL-coils I_{IL} to the current flowing through the VF-coils I_{VF}:

$$C_r = \frac{I_{IL}}{I_{VF}} \tag{3.22}$$

As visible from Tab. 3.1, for the synergy experiments, the C_{ratio} was 3 and the current flowing through the VF-coils was 13 kA.

The CNT-coil setup used to compute the magnetic field in the simulation is shown in Fig. 3.4.

Note that the simulation lab frame is rotated by $\pi/2$ about the x-axis with respect to the conventional lab frame shown in Fig. 1.2a.

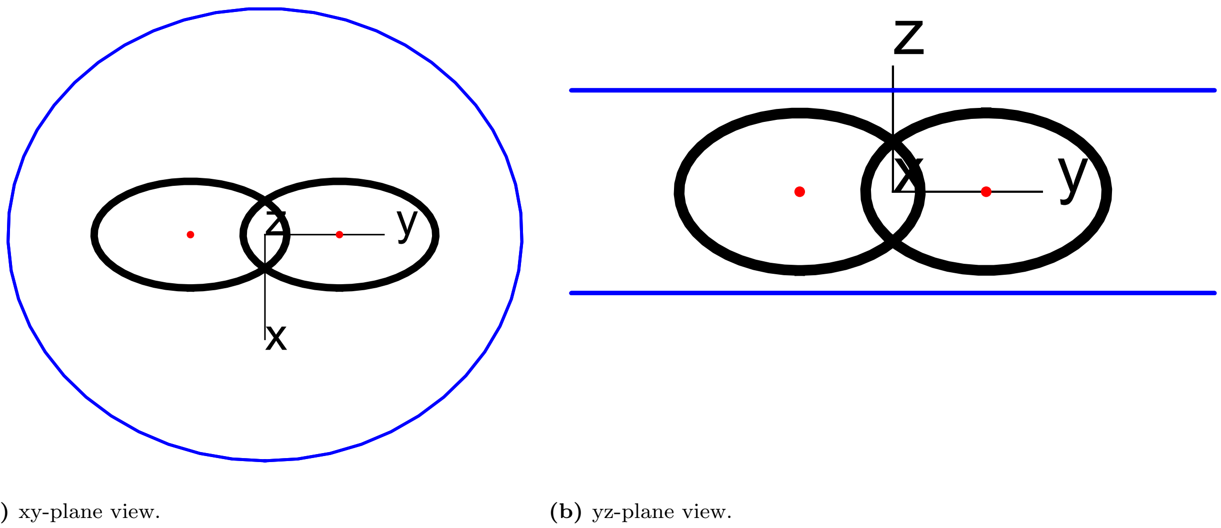

(a) xy-plane view.

(b) yz-plane view.

Figure 3.4: CNT coil setup to compute the magnetic field for the synergy simulations. The red lines are the IL-coils, the blue lines the VF-coils. The red dots mark the center of the IL-coils.

To compute the magnetic field $\vec{B}$ at a point $\vec{r}$, the point is transformed into the reference frame of Fig. 3.2. The resulting magnetic field is then transformed back into the initial frame.

In the presence of several coils, the resulting magnetic field at a point $\vec{r}$ is the sum of the magnetic field of each individual coil:

$$\vec{B}(\vec{r}) = \sum_i \vec{B}_i(\vec{r}) \tag{3.23}$$

3.2.4. Poincaré-Plots

An important feature of any magnetic confinement device is the concept of the magnetic *flux surfaces* (section 2.3.2). Specifically, the last closed flux surface (LCFS) is the surface furthest away from the magnetic axis which still creates a closed surface and confines particles. Thus, the LCFS determines the obtainable plasma volume.

A Poincaré-plot is a method the visualize flux surfaces for a given magnetic field: It represents the points where a magnetic field line penetrates a poloidal cross-section of the torus, giving a 2D-representation with coordinates (r, z) of the flux surfaces.

In a collision-less plasma, the trajectories of a particle are almost identical to the magnetic field lines. For this reason, this thesis uses the trajectory of (relatively) slow electrons to create a poincaré-plot. The puncture points of these particles are evaluated at several toroidal angles. Results are shown in section 4.3.

3.2.5. Tracing Mode

Depending on the information required, the code can either solve the particle equations of motion or the guiding center motion-equations. The advantage of the latter is, as previously mentioned, the possibility of bigger stepsizes, decreasing computation time. Some information might be lost using this approach however.

The EOM for the single particle are straight-forward; only the magnetic field $\vec{B}$ and the particle velocity are needed. An additional term $\vec{E}$ is added in the presence of an electric field (introduced by the microwaves, see section 3.2.12).

For the GCM, the velocity components $v_\perp, v_{||}$ are necessary. Since the magnetic moment $\mu = \frac{mv_\perp^2}{2B}$ is constant and the total kinetic energy conserved, the pitch-angle (eq. 2.17) will change depending on $\vec{B}(\vec{r})$.

To compute the gradient (and curvature) of $\vec{B}$, the magnetic field in its near environment $\vec{B}(\vec{r} + d\vec{r})$ is computed as well.

It is possible to switch between the two representations. To switch from the GCM to a single particle-approach, the initial velocity is transformed using the local magnetic field $\vec{B}(\vec{r})$ and a random gyro-phase $0 \leq \delta \leq 2\pi$. The velocity, in a frame where $\vec{B} = B \cdot \hat{e}_z$, is then:

$$v_x = v_\perp cos(\delta) \tag{3.24}$$

$$v_y = v_\perp sin(\delta) \tag{3.25}$$

$$v_z = v_{||}. \tag{3.26}$$

To get the velocity in the lab frame it is rotated such that $\hat{e}_z$ points in the direction of the magnetic field:

$$\hat{e}_z' \,||\, \vec{B}.$$

Vice-versa, to switch from the single particle motion to the GCM, rotate the magnetic field vector to align with the z-axis and then apply the same transformation to the velocity. The two velocity components are then:

$$v_\perp = \sqrt{v_x^2 + v_y^2} \tag{3.27}$$

$$v_{||} = v_z. \tag{3.28}$$

3.2.6. Random number generators (RNG)

Uniform random numbers Fortran and other programming languages use a **R**andom **N**umber **G**enerator (RNG) to create (pseudo-) random numbers. The standard Fortran-routine $r = rand(I)$ returns a uniform, (pseudo-)random number $0 \leq r < 1$, depending on the input integer I. In order to get different numbers (following a uniform random distribution), dynamic inputs I are created in the code. Typically, a combination of the current CPU-time `time` as well as loop-indices `j` are used. To ensure that numbers used for different purposes inside the code are different, a different combination of the variables are used.

Gaussian random numbers Gaussian random numbers can be transformed from uniform random numbers using the Box-Muller transform. [70] The method is fairly straightforward: two uniform random numbers u_0, u_1 are transformed to two Gaussian numbers r_0, r_1 as follows:

$$r_0 = \sqrt{-2 \cdot ln(u_1)} \cdot sin(2\pi u_0) \tag{3.29}$$

$$r_1 = \sqrt{-2 \cdot ln(u_1)} \cdot cos(2\pi u_0). \tag{3.30}$$

The result is a Gaussian distribution of variables with mean $\mu = 0$ and standard deviation $\sigma = 1$. Fig. 3.5 shows a set of uniform random numbers (blue, left side) which are transformed to Gaussian random numbers (black, right side).

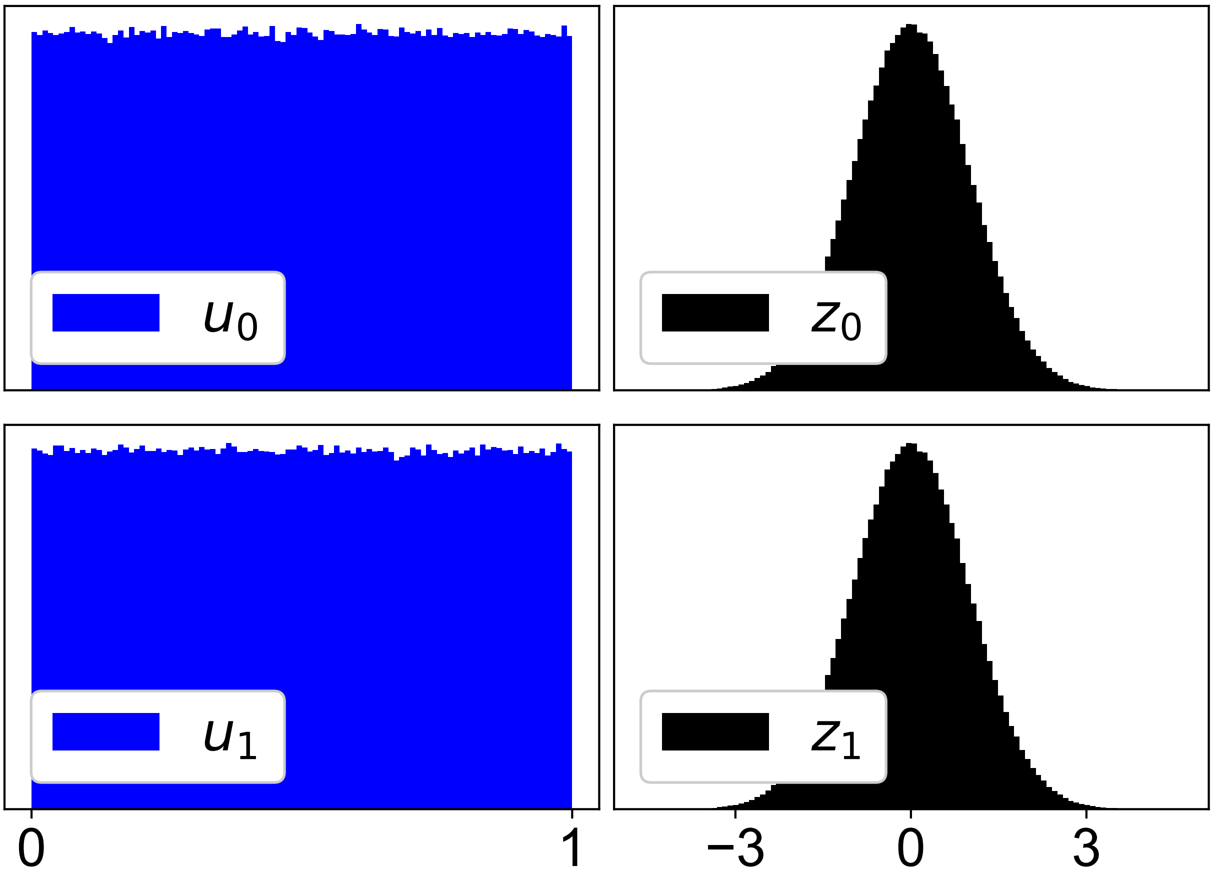

Figure 3.5: Histogram of uniform, random numbers u_0 and u_1 (blue) and Gaussian random numbers z_0 and z_1 (black), created using the Box-Muller method.

3.2.7. Interaction probability

The numerical procedure uses single time-steps of length Δt. The probability of a certain collision/process P_i to happen during a time step depends on the collisional frequency of that process ν_{coll} (section 2.5.1) and the length of the time-step Δt:

$$P_i = 1 - exp(-\nu_{coll} \cdot \Delta t) \tag{3.31}$$

During each step, a uniform, random number p_i

$$0 \leq p_i < 1$$

is generated (for each process). If the random number is smaller than the probability of a certain process, the process will take place:

$$\text{If } (p_i < P_i) \text{ then :} \qquad \text{process takes place.}$$

The collisional frequency ν_{coll} for each collision/process is to be determined. Despite being fairly straightforward for some processes; other frequencies might be harder to obtain and therefore estimates will be used. The frequencies or their estimates are mentioned in the subsequent sections.

3.2.8. Elastic collisions

Different approaches to simulate elastic collisions between the traced electron and background particles were used and tested over the course of this thesis. One commonality for all of them was that the change of velocity $d\vec{v}$ was calculated in a specific reference frame; namely one where $\vec{v} = v \cdot \hat{e}_z$. This reference frame will be termed *z-frame* from here on.

A detailed description on how to change to and from this frame of reference is given in Appendix B.

Rutherford scattering (electron-ion) The theory of elastic (Rutherford)-scattering collisions was presented in section 2.5.2.

Let's first consider $e^- - I^+$-collisions. Here, the motion of the (heavy) ions can be neglected. If a collision occurs, a random impact parameter

$$b_{min} \leq b \leq b_{max}$$

is chosen. Using this random impact parameter and the kinetic energy of the incident particle before the collision, E_∞, the scattering angle θ is computed using eq. 2.49 and 2.46. To account for 3D-effects, an additional (random) angle

$$0 \leq \varphi \leq 2\pi$$

is used. The velocity vector after the collisions in the *z-frame* is:

$$\vec{v}'_{zframe} = R_z(\varphi) R_y(\theta) \begin{pmatrix} 0 \\ 0 \\ v \end{pmatrix} . \tag{3.32}$$

Using the procedure from section B, the velocity (and position) after the collision in the lab-frame can be computed.

The dependence of the scattering angle θ as a function of the (random) impact parameter b is shown in Fig. 3.6. The energy of the incident electron was fixed at $E_\infty = 100\ eV$. At this energy and for CNT-parameters, the range of impact parameters was:

$$b_{min} \leq b \leq \lambda_D$$
$$7.3 \cdot 10^{-12}\ m \leq b \leq 1.6 \cdot 10^{-4}\ m.$$

The figure clearly shows that over a wide range of impact parameters, the deflection angle is very small.

Note that the angle is negative, since the charges of the incoming electron and the scattering ion are opposite and therefore the electron is attracted towards the ion.

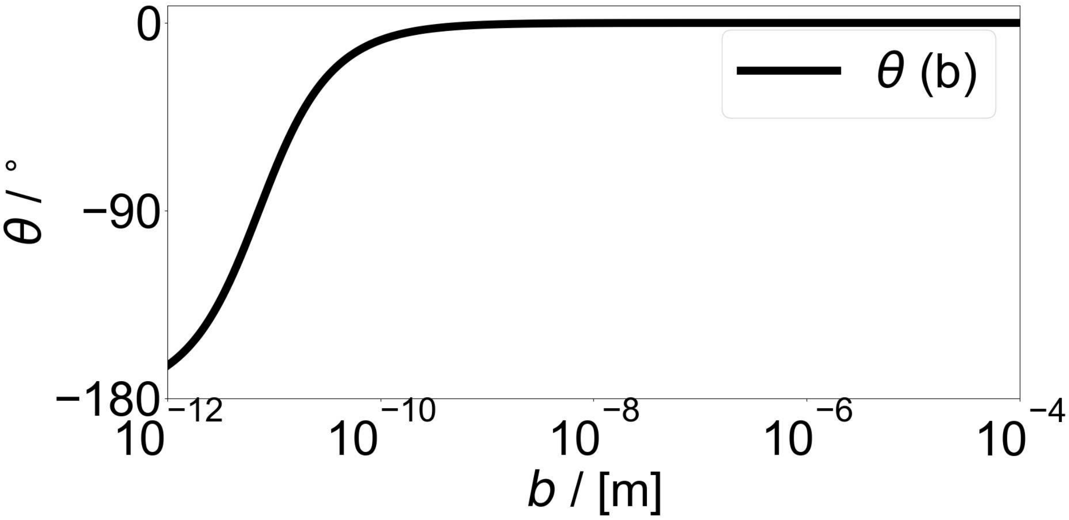

Figure 3.6: Deflection angle as a function of the impact parameter for fixed energy of incoming electron $E_{inc} = 100\ eV$.

To get the probability of a single, elastic collision, the collisional frequency is needed (see section 3.2.7). Typically, a particle undergoes numerous collisions before being deflected significantly; e.g. by a cumulative angle of 90°. The collisional frequency of a single particle with charge q, mass m and velocity v, colliding with a background species with charge q', mass m' and density n' is given by: [71]

$$\nu_{qq',90^o}(v) = \left(\frac{qq'n'}{\varepsilon_0 m}\right)^2 \frac{ln(\Lambda)}{4\pi(\mu/m)v^3 n'}, \tag{3.33}$$

where $\mu = \frac{m' \cdot m}{(m'+m)}$ is the reduced mass. For a bulk electron in CNT ($T \approx 5\ eV$) colliding with ions, the frequency is:

$$\nu_{ei,90^o}(E_e = 5\ eV) \approx 6.2 \cdot 10^4\ Hz.$$

This is consistent with previous estimates made for CNT: [60]

$$10^4\ Hz \leq \nu_{ei,90^o} \leq 10^6\ Hz.$$

Note that in eq. 3.33 the collisional frequency ν_{90^o} decreases rapidly with increasing v; therefore, at higher velocities, an electron is less likely to collide. Fig. 3.7 shows ν_{90^o} for a test particle in CNT, with energies between the bulk electron energy $E = 5\ eV$ and the thermionically emitted electrons $E = 100\ eV$.

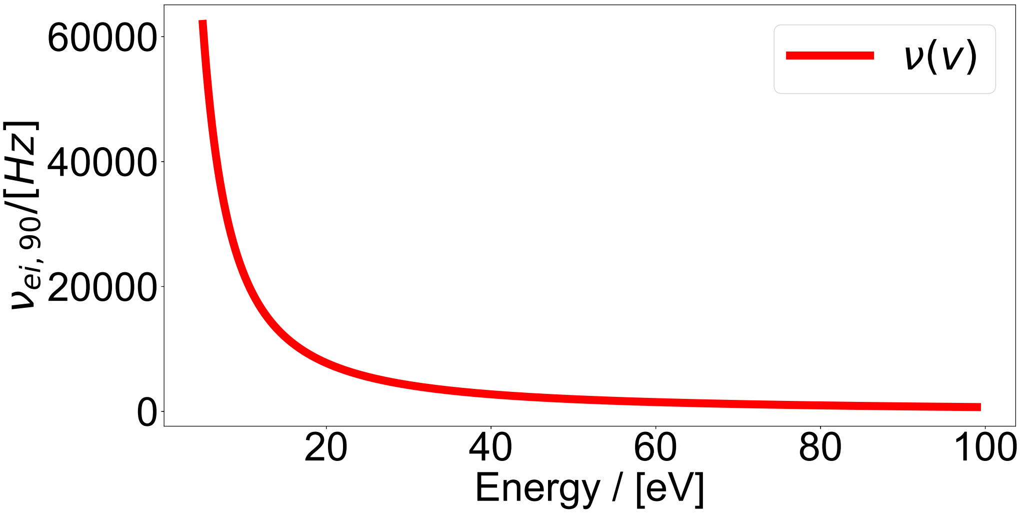

Figure 3.7: Collisional frequency $\nu_{ei,90^o}$ in CNT as a function of the test particle energy.

Again, $\nu_{ei,90^o}$ is the frequency of *cumulative* large-angle deflections, of order 90^o. This frequency is relatively low and is not very relevant to our problem: in order to model ionization and start-up in CNT, we are rather concerned with *individual* collisions, including those responsible for small deflections. For this reason, a study was performed to relate the frequency of a single collision ν_{sinlge} to $\nu_{ei,90^o}$.

In this study, the deflection angles of single encounters were summed up until their sum θ_{cum} reached 90° (or more). In order to count how many times this occurred for a given number of collisions, the sum was reset to 0 whenever reaching $\theta_{cum} \geq 90°$.

$$\theta_{cum} = \sum_i \theta_i$$

This procedure was repeated for a fixed number of collisions. The (average) number of collisions necessary for a single significant deflection was then evaluated.

Fig. 3.8 shows the resulting single scattering angles (black lines) and cumulative angles (red line) as a function of the number of collisions.

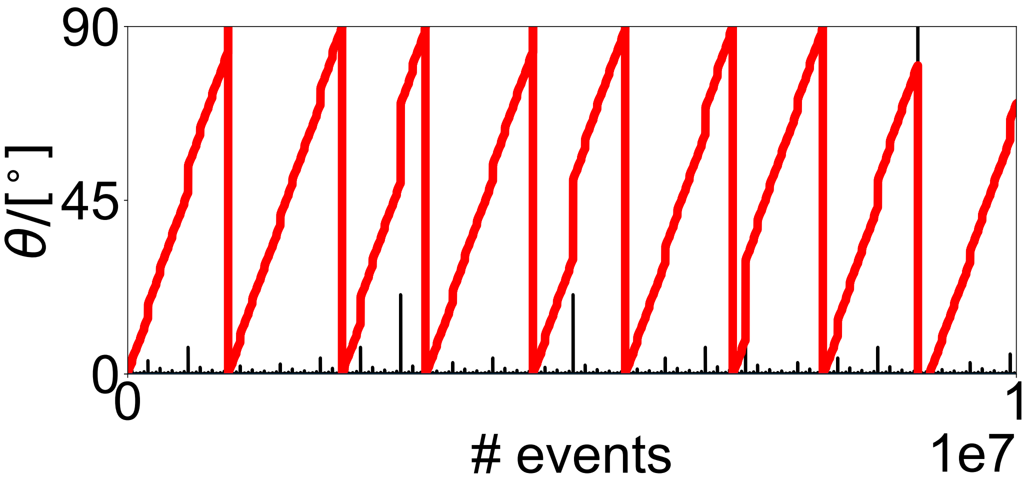

Figure 3.8: Single (black) and cumulative (red) scattering angles. The cumulative angle was reset to zero after surpassing 90°.

After a total of $n_{tot} = 10^7$ individual collisions, a number of $n_{90} \approx 8.7$ large deflections occurred, meaning that an average of

$$n_{cum} = \frac{n_{tot}}{n_{90}} \approx 1.15 \cdot 10^6$$

collisions are necessary for a full deflection. Following from this, the collisional frequency of a single collision event is:

$$\nu_{single} \approx 1.15 \cdot 10^6 \cdot \nu_{ei,90}(v). \tag{3.34}$$

The frequency (and thus the probability) is dynamically adjusted during each step in the code.

Rutherford scattering (electron-electron) For electron-electron collisions, many of the pre-assumptions made for the electron-ion collisions are not valid any more. The motion of the scattering electron is fast and non-negligible; thus, a conversion to the center of mass-system is usually necessary.

The scattering angle θ is computed in the center of mass-system, and the incident electron is scattered by an angle χ in the lab frame: [52]

$$\chi = \frac{\theta}{2}. \tag{3.35}$$

The calculation of the scattering angle in the center of mass is very similar to eq. 2.49; replacing the mass of the particle with the reduced mass $\mu = \frac{m_1 m_2}{(m_1+m_2)} = \frac{m_e}{2}$ and the speed by

$$v_{CoM} = |\vec{v}_1 - \vec{v}_2|. \tag{3.36}$$

The energy transfer (eq. 2.50) also simplifies to:

$$\frac{dE}{E_1} = sin^2(\frac{\theta}{2}). \tag{3.37}$$

An important step is finding the velocity of the scattering partner, $\vec{v}_2$. We assume the scattering particles' velocity to be taken from a Maxwellian distribution centered around $T_{bg} = 5\ eV = 5.8 \cdot 10^4\ K$. Every single velocity component of the particle has a Gaussian distribution with

$$\mu = 0$$
$$\sigma = \sqrt{\frac{k_B \cdot T}{m}}.$$

The speed distribution of the particles $v = \sqrt{v_x^2 + v_y^2 + v_z^2}$ will then be Maxwellian. The single velocity component distribution is shown in Fig. 3.9a; the speed distribution in Fig. 3.9b (blue histogram). It compares very well to the analytical Maxwell-Boltzmann formula (black line).

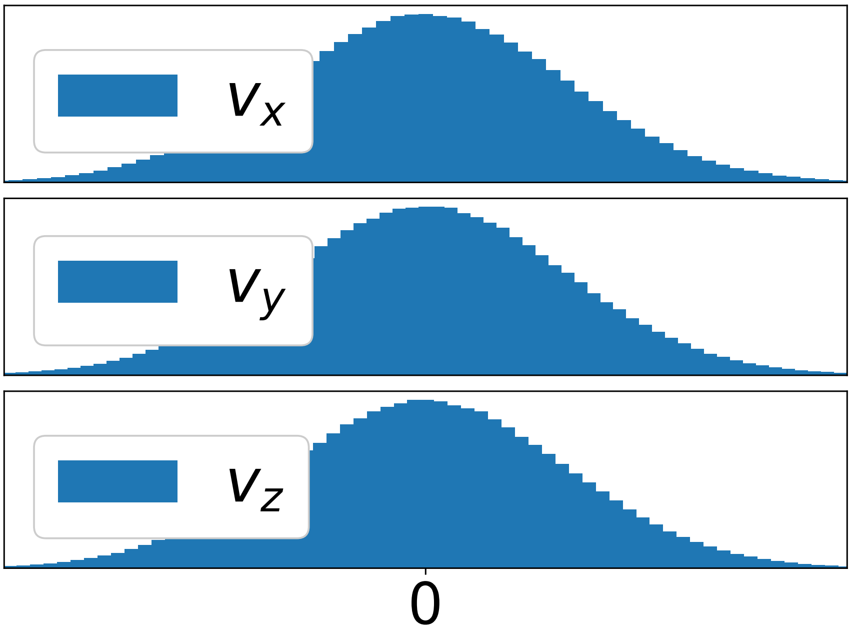

(a) Distribution of velocity components v_x, v_y and v_z for the background scattering particles.

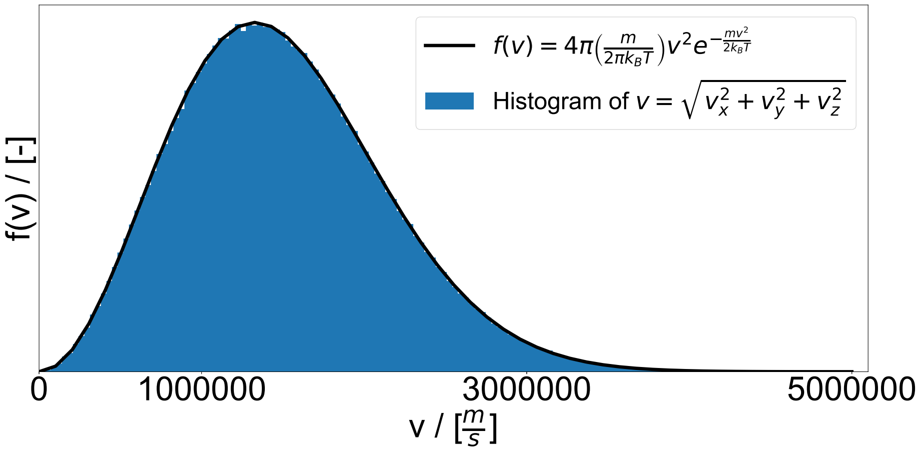

(b) Maxwell-Boltzmann distribution for the speed $v = \sqrt{v_x^2 + v_y^2 + v_z^2}$ of the background particles.

Figure 3.9: Velocity and speed of the scattering background electrons.

The rest is basically the same as for the electron-ion collisions. The initial velocity is first rotated to the *z-frame*. Since energy is transferred, the total speed of the particle is slightly lower than before:

$$v' = \sqrt{\frac{2E'}{m}} = \sqrt{\frac{2E(1 - sin^2(\frac{\theta}{2}))}{m}}. \tag{3.38}$$

The velocity after the collision in the *z-frame* is then:

$$\vec{v}'_{z-frame} = R_z(\delta) R_y(\chi = \frac{\theta}{2}) \begin{pmatrix} 0 \\ 0 \\ v' \end{pmatrix} . \tag{3.39}$$

Fokker-Planck-Approach As a consequence of many single collisions, a particle will experience a drag; slowing the particle down; as well as diffusion effects in the velocity space (section 2.5.2).

The rates at which a *test* particle is slowed down or diffuses (eq. 2.59-2.61) in the presence of a gas of *field* particles require the Maxwell-integral $\psi(x)$ and its derivative $\psi(x)$; with

$$x = \frac{v^2}{v_{T_s'}}$$

being the relative speed parameter and $v_{T_s'}$ being the thermal speed of the background (Maxwellian) species in consideration. The Maxwell-integral is typically solved numerically and most programming languages (including Fortran) already have built-in functions to solve the integral. Its value as a function of x is shown in Fig. 3.10.

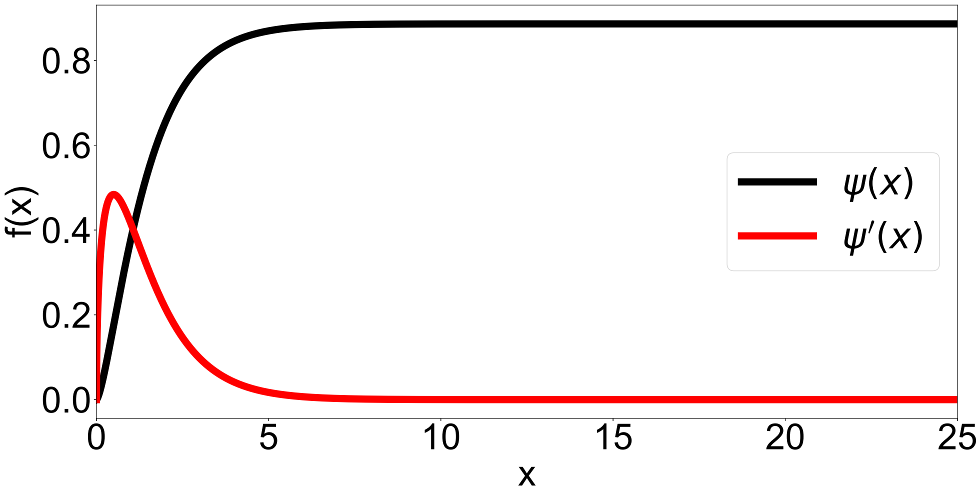

Figure 3.10: Maxwell-integral $\psi(x)$ and its derivative $\psi'(x)$ as a function of the relative speed parameter x.

The drift and diffusion rates as a function of the relative speed parameter for a background of electrons with a temperature of $T_e = 5\ eV$ are shown in Fig. 3.11. Some interesting observations can be made:

- Since the diffusion is mostly in the direction perpendicular to propagation, perpendicular diffusion $\nu_\perp$ is a lot higher than parallel diffusion $\nu_{||}$.

- With decreasing x, the energy loss rate ν_E decreases, since not as much energy can be transferred if the energy of the constituent particles is (nearly) equal. As x becomes smaller than 1, the field particles will be more energetic than the test particle, transferring energy *to* the test particle. Therefore, the energy loss rate becomes negative.

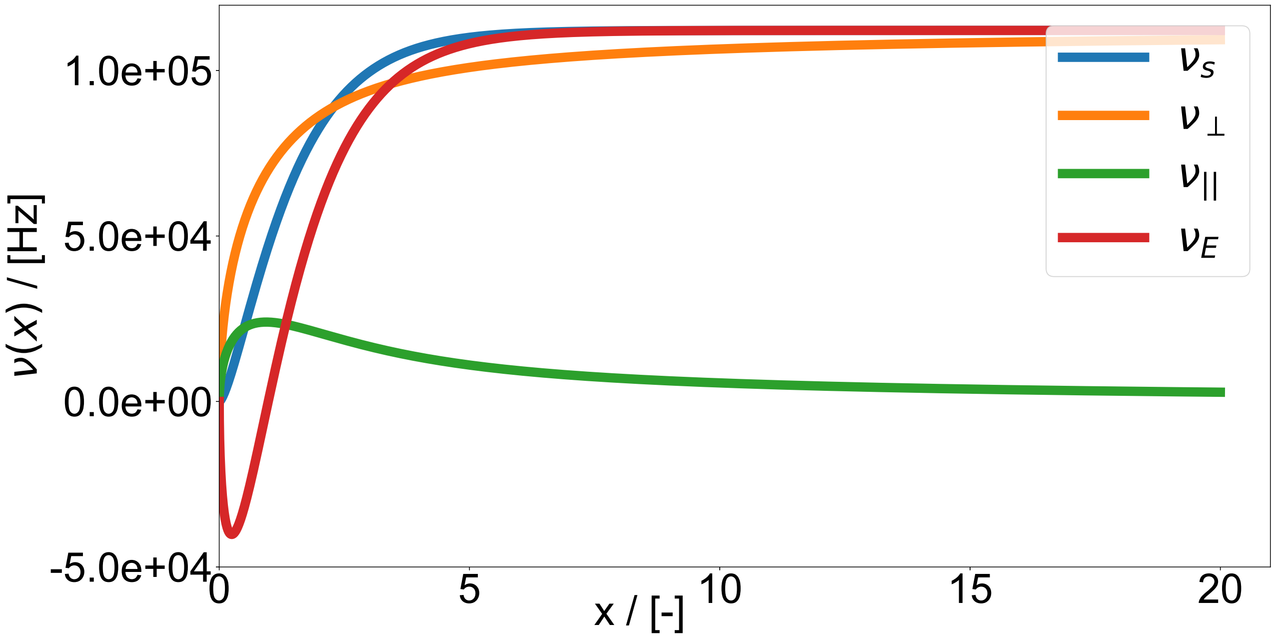

Figure 3.11: Slowing down rate ν_s, perpendicular diffusion rate $\nu_\perp$, parallel diffusion rate $\nu_{||}$ and energy loss rate ν_E as a function of the relative speed parameter x. The field particles are electrons with a temperature of $T_e = 5\ eV$.

The same rates for ions (at the same background temperature) is shown in Fig. 3.12. Note that since ions are much slower than the electrons $v_{ion} << v_e$, the relative speed parameter x usually takes on values much larger than for the electronic case. However, the values are basically constant for $x \geq 20$.

Some observations here include:

- The energy loss rate ν_E and the parallel diffusion rate $\nu_{||}$ are basically zero for most values of $x \geq 20$. This can be attributed to the fact that due to the ions' heavy masses, practically no energy is transferred in electron-ion collisions. The diffusion is mostly in the perpendicular direction.
- The values for the ionic perpendicular diffusion is much larger than for the electronic case:

$$\nu_{\perp,ion} >> \nu_{\perp,electron},$$

leading to the total perpendicular diffusion being mostly due to the effects of ions.

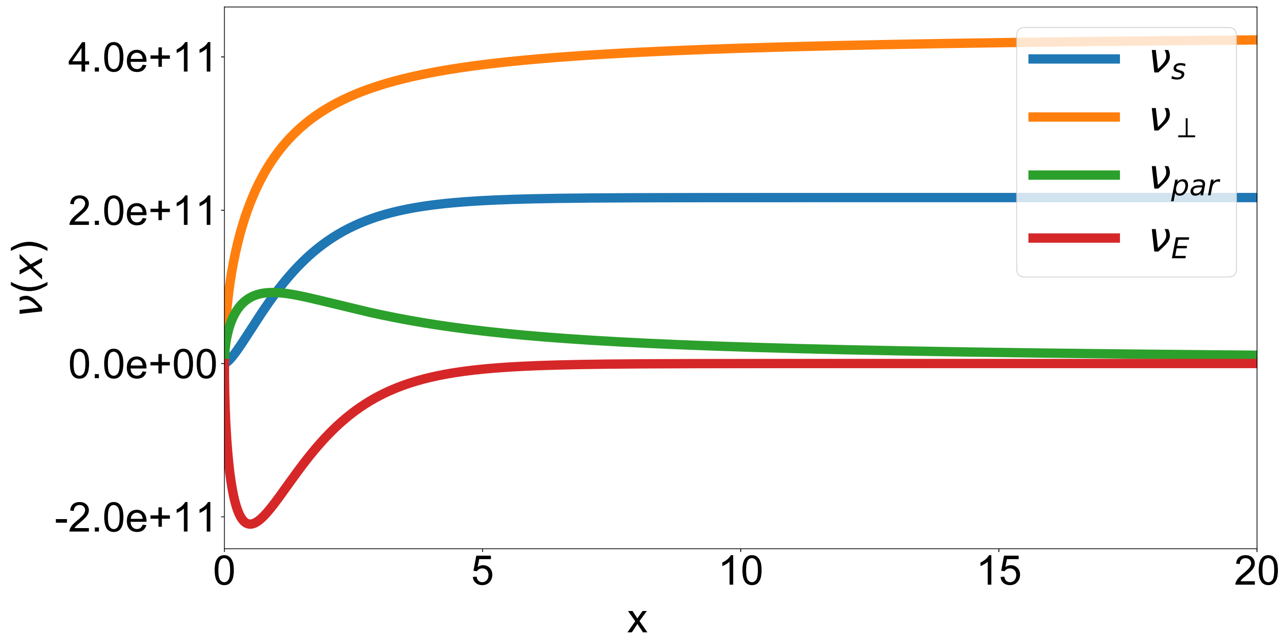

Figure 3.12: Slowing down rate ν_s, perpendicular diffusion rate $\nu_\perp$, parallel diffusion rate $\nu_{||}$ and energy loss rate ν_E as a function of the relative speed parameter x. The field particles are ions with a temperature of $T_{ion} = 5\ eV$.

Collisions with field ions mostly change a particles path, while collisions with field electrons also lead to energy transfer. The effect of collisions with both particle types can be combined into single collision rates by just summing the rates for each species:

$$\nu_s = \sum_{s'} \nu_s^{s/s'} \tag{3.40}$$

$$\nu_\perp = \sum_{s'} \nu_\perp^{s/s'} \tag{3.41}$$

$$\nu_{||} = \sum_{s'} \nu_{||}^{s/s'} \tag{3.42}$$

$$\nu_E = \sum_{s'} \nu_E^{s/s'}. \tag{3.43}$$

Assume that the velocity of a test particle initially points in the z-direction (z-*frame*). Under the influence of collisions with (Maxwellian) field particles, its velocity after a short time $t = \Delta t$ is given by: [53]

$$\vec{v}(t) = v_0(1 - \nu_E \frac{t}{2}) \begin{pmatrix} |\eta_2|\sqrt{\frac{\nu_\perp t}{2}} cos(2\pi\xi) \\ |\eta_2|\sqrt{\frac{\nu_\perp t}{2}} sin(2\pi\xi) \\ 1 + \eta_1\sqrt{\nu_{||} t} \end{pmatrix}, \tag{3.44}$$

where v_0 is the particle speed at $t = 0$; $0 \leq \xi < 1$ is a uniform random number and η_1/η_2 are Gaussian random numbers with $\mu = 0$ and $\sigma = 1$. The random numbers account for the random, Monte-Carlo nature of the single collision processes.

Eq. 3.44 eradicates the need to know the probability of a collision to happen by its nature of collective effects.

The big advantage of using eq. 3.44 is its simplicity as compared to simulating the single collision approach described before.

3.2.9. Electron impact ionization

The complex, 3-body system of an ionization collision is not easy to solve analytically. A Monte-Carlo approach to simulate ionization events was used in this thesis. [72]

For the process the atom is assumed to be at rest before and after the collision (which is reasonable due to its mass being $\approx 10^4$ times higher than that of the electrons). No energy is exchanged between the electrons and the atom/molecule.

The total energy is conserved:

$$E_{tot,in} = E_{tot,out} = E'_{inc} + E'_{ej} + E_{ion} = E_{inc}, \tag{3.45}$$

with E_{inc}/E'_{inc} being the (kinetic) energy of the incident electron before/after the collision and E'_{ej} being the (kinetic) energy of the ejected electron. The energy of the two electrons after the ionization collision is calculated using a uniform, random number R:

$$0 \leq R < 1 \tag{3.46}$$

$$E'_{ej} = \bar{E} \cdot tan\left[R \cdot tan^{-1}\left(\frac{E_{inc} - E_{ion}}{2\bar{E}}\right)\right] \tag{3.47}$$

$$E'_{inc} = E_{inc} - E'_{ej} - E_{ion}. \tag{3.48}$$

The energy E'_{ej} as a function of the incoming particle energy E_{inc} is shown in Fig. 3.13. For small values of the random parameter R, almost no energy is transferred. For $R = 1$, both of the two electrons take on half of the remaining energy $E_{inc} - E_{ion}$.

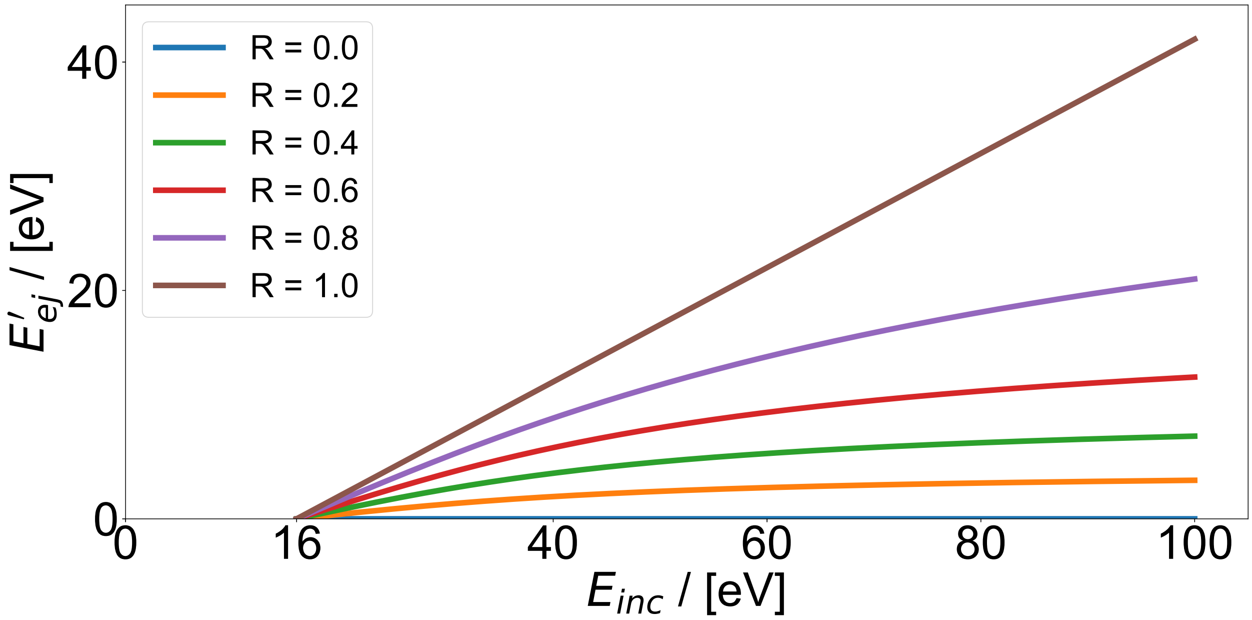

Figure 3.13: Energy of the secondary electron created during an ionization collision as a function of the incident particle energy. The parameter R is usually a uniform random number, here taking on discrete values.

After the energy of the constituent electrons has been assigned, the direction of the electrons has to be determined. For this, it is assumed that both particles follow the trajectory of the incident particle, scattered by an angle $\chi(E)$ relative to its initial direction $\vec{v}$:

$$\chi(E) = cos^{-1}\left[\frac{2+E-2(1+E)^R}{E}\right]. \tag{3.49}$$

The calculation of the angle uses the same random number R as before and is dependent on the energy, meaning both particles will be scattered by a different angle (unless for $R = 1$, where both are assigned the same energy).

The higher the energy of the incoming electron, the smaller the scattering angle will be. Additionally, the random parameter R greatly impacts the scattering angle: For small values, there is almost no scattering while for $R = 1$ the particles will be fully deflected with an angle of $\chi = 180°$.

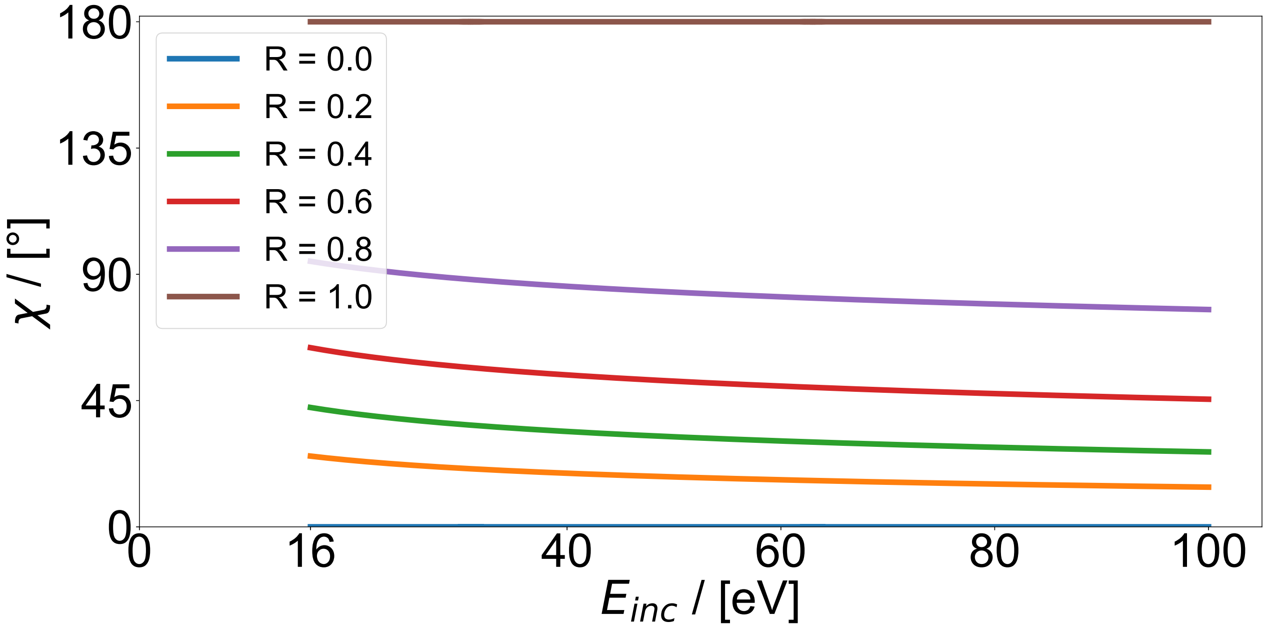

Figure 3.14: Ionization scattering angle χ as a function of the incident particle energy. The parameter R is usually a uniform random number, here taking on discrete values.

To account for three-dimensional effects, the same procedure as for elastic collision (section 3.2.8) was used by introducing an additional, random angle $0 \leq \delta \leq 2\pi$. In a frame where the particles' velocity only points in the z-direction (z-frame), the velocity is scattered by the angle χ about the y-axis and then by δ about the z-axis:

$$\vec{v}' = R_z(\delta) R_y(\chi) \vec{v}. \tag{3.50}$$

After the transformation, the new velocity is transformed back to the lab-frame.

For the ionization, the collisional frequency as a function of the cross-section $\sigma(E)$ is used (eq. 2.36):

$$\nu_{ion} = |v_{rel}| n_N \sigma_{ion} \tag{3.51}$$

where n_N is the density of neutral, background atoms and $|v_{rel}| = v_e - v_N \approx v_e$ is the relative velocity.

The ionization cross-section for Nitrogen is shown in Fig. 3.15.

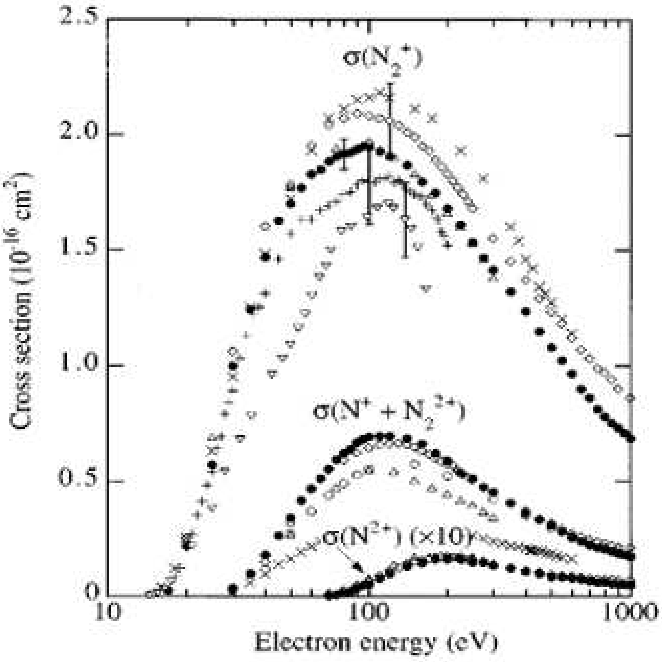

Figure 3.15: Ionization cross section for N_2^+ as a function of the incoming electron energy. [73]

The cross-section has a maximum at $E \approx 100\ eV$, which is approximately the average energy of the electrons emitted from the electron-gun. The neutral density can be obtained from the (background) pressure p_{bg} in CNT. The pressure for the synergy experiments was

$$p_{bg} = 10^{-5}\ Torr \approx 1.33 \cdot 10^{-3} Pa.$$

Assuming the background gas to be at room temperature $T_{bg} \approx 300\ K$, the particle density is obtained from the ideal gas equation:

$$n = \frac{p_{bg}}{k_B T_{bg}} \approx 3.22 \cdot 10^{17}\ m^{-3}, \tag{3.52}$$

with k_B the Boltzmann constant.

The code uses a part-wise linear fit of Fig. 3.15. The fit is shown in Fig. 3.16.

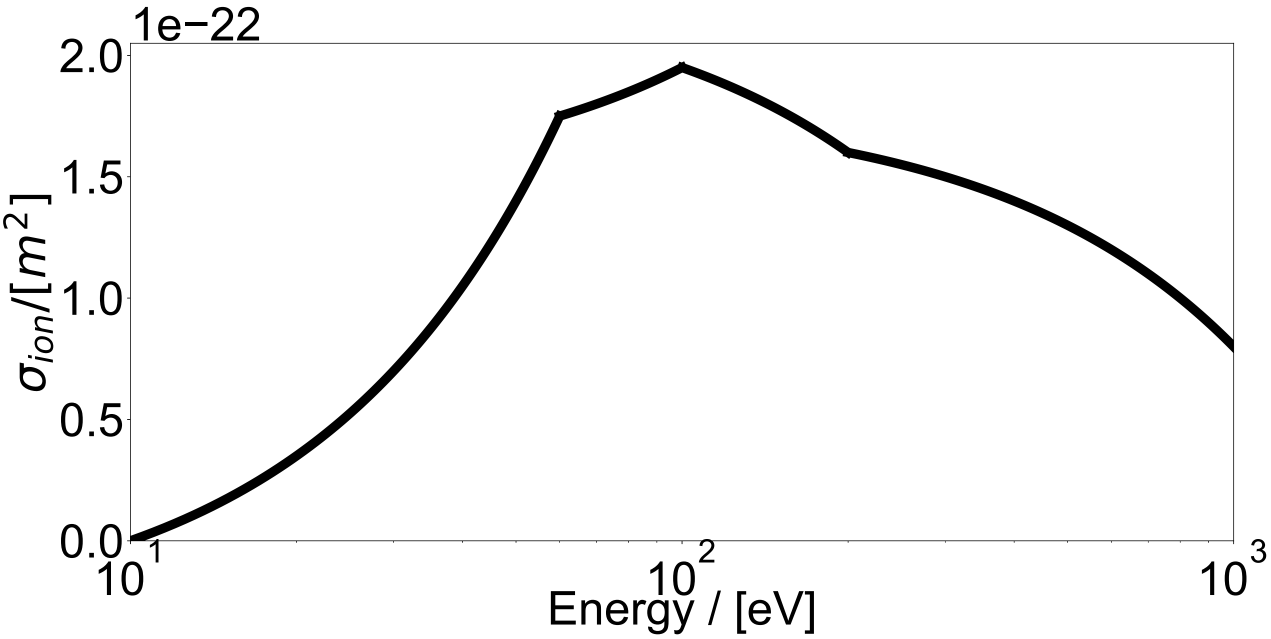

Figure 3.16: Part-wise linear fit of the ionization cross-section σ_{ion} from Fig. 3.15.

For typical step-size times, the ionization probability is fairly low and the particle will usually have finished several revolutions inside the torus before actually undergoing an ionization collision.

Continued tracing of secondary electrons The secondary electrons created during an ionization event are also subject to microwave heating and can partake in additional ionization collisions, creating even higher densities. Therefore, the energy, velocity and position of the secondary electrons are retained, serving as the initial values for a new simulation. In order to limit the amount of simulations to be performed, the code usually only starts tracing a secondary electron if its energy is above a certain threshold energy:

$$E_{sec} > E_{threshold}.$$

This threshold can arbitrarily be chosen; however, since a particle will only partake in ionization events if its energy is above the ionization energy of $E_{ion,N} \approx 16\ eV$, it makes sense to choose the threshold at or around this energy.

Fig. 3.17 shows a sample energy history (over time) for an electron with $E_{initial} = 200\ eV$ (black solid line) undergoing ionization events at certain timepoints and losing energy in the process. If the secondary electrons are above an energy threshold (here chosen to be $E_{threshold} = E_{ion} = 16\ eV$), they will continue to be traced, until their energy drops below the threshold (due to further ionization collisions).

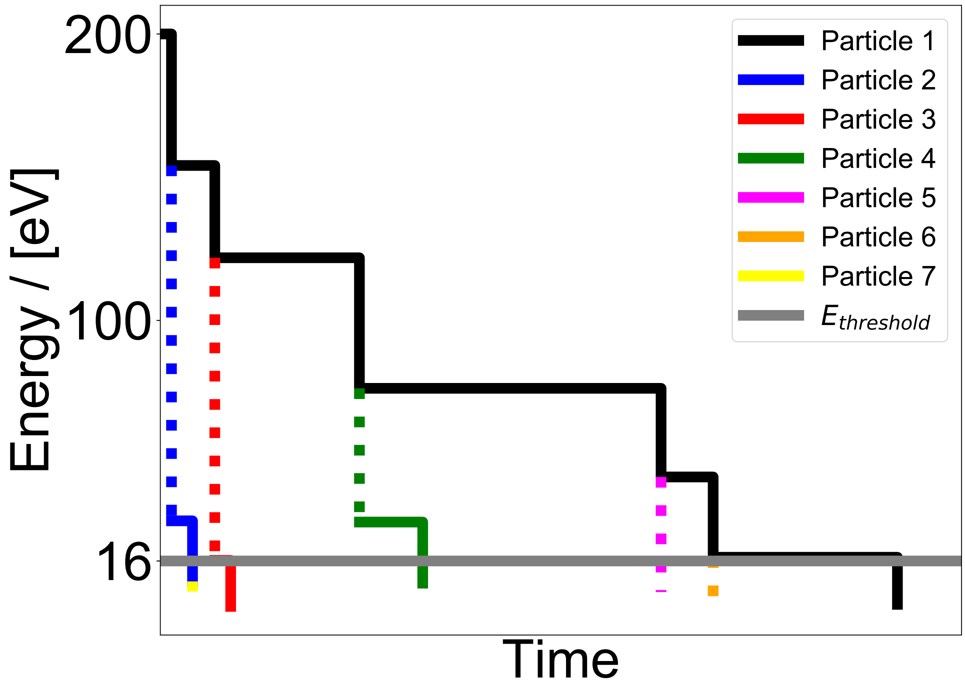

Figure 3.17: Energy of electrons as a function of time. When a particle undergoes a collision, it transfers energy to an atom to ionize it as well as energy to a secondary electron. The tracing for the initial and secondary created electrons continues until its energy drops below a certain threshold.

3.2.10. Electron recombination

Recombination effects are basically the opposite of ionization events; serving as a drain for electrons. If the electron recombines, it is essentially lost for further tracing and the code stops.

The recombination rate of a plasma can be determined using afterglow measurements. Once external heating is switched off, the plasma will decay at the rate of eq. 2.72. When ignoring the diffusive decay $\frac{n}{\tau}$, the density decays as:

$$\frac{dn_e}{dt} \approx -\alpha n^2. \tag{3.53}$$

Measurements in CNT were conducted as a function of the probe displacement, which effectively serves as the radial coordinate. The results are shown in Fig. 3.18.

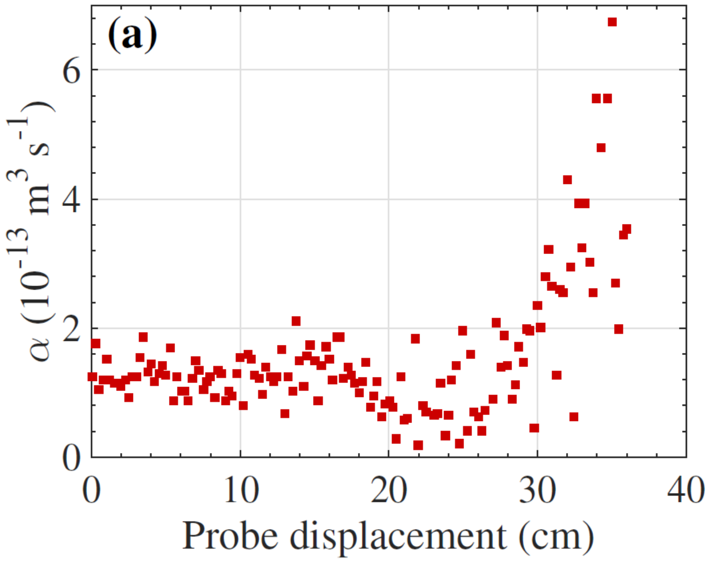

Figure 3.18: Recombination coefficient α in CNT, measured during afterglow experiments and as a function of the radial coordinate r. [60]

The region where α was mostly constant is the region inside the plasma. Here, the coefficient was averaged to be: [60]

$$\alpha \approx 1.25 \cdot 10^{-13} \, \frac{m^3}{s}.$$

The total recombination rate is thus:

$$\left(\frac{dn_e}{dt}\right)_{tot} = 1.1 \cdot 10^{19} \frac{1}{m^3 s}.$$

With an electron density of around $n_e \approx 2.7 \cdot 10^{16} \ m^{-3}$ for the experiments, this gives a decay rate of

$$\nu_{decay,single} = \frac{\left(\frac{dn_e}{dt}\right)_{tot}}{n_e} \approx 400 \ Hz.$$

This rate is then used to determine the probability of a such event during each step in the code.

3.2.11. Exit criteria

The code has three main exit criteria to decide when to stop tracing a particle:

1. **Particle leaving the simulation domain:** If a particle's position is outside a cylinder with $r = \sqrt{x^2 + y^2} = 0.72\ m$ and $h = \pm 0.5\ m$ (the ± indicating it extends in both direction around the origin); which roughly corresponds to the CNT vacuum-chamber; the code will conclude that the particle exited the vessel and will stop further tracing.

2. **Ionization with too little energy:** After undergoing an ionization event, if the particle energy falls below a certain threshold $E < E_{threshold}$, the tracing will stop (section 3.2.9).

3. **Recombination:** If the electron recombines with an ion, it is also effectively lost and tracing will stop (section 3.2.10).

3.2.12. Microwave modelling and absorption

As a first-order approach, we will assume that the interaction between the particle and the wave is simply due to the interaction of the particle with the waves electromagnetic field. [42] This means that the Lorentz-force $\vec{F}_L$ has an additional wave electric field $\vec{E}_w$ and a wave magnetic field $\vec{B}_w$. In practice, the wave magnetic field is negligible compared to the background magnetic field,

$$\vec{B}_0 >> \vec{B}_w,$$

and the Lorentz-force becomes:

$$\vec{F}_L = q(\vec{E}_w + \vec{v} \times \vec{B}_0). \tag{3.54}$$

The waves are modelled using a plane wave approach (eq. 2.74):

$$\vec{E}(\vec{r}, t) = \vec{E}_0 \cdot e^{i(\vec{k}\cdot\vec{r} - \omega t + \varphi)}. \tag{3.55}$$

The physical field, interacting with the wave, is the real part of eq. 3.55:

$$Re(\vec{E}(\vec{r}, t)) = cos(\vec{k} \cdot \vec{r} - \omega t + \varphi). \tag{3.56}$$

The amplitude of the waves' electric field depends on its intensity I (eq. 3.2):

$$E_0 = \sqrt{\frac{2I}{c\varepsilon_0}}, \tag{3.57}$$

where ε_0 is the vacuum permittivity.
The polarization of the wave influences its magnitude vector $\vec{E}_0$. In a frame where the wave vector points in the z-direction; $\hat{e}_z||\hat{k}$, the amplitude vector can be obtained using the polarization angle θ:

$$\vec{E}_0 = E_0 \cdot \begin{pmatrix} cos(\theta) \\ sin(\theta) \\ 0 \end{pmatrix}, \tag{3.58}$$

with $0 \leq \theta \leq 2\pi$.
In addition to the polarization, the direction of the wave, described by its wave-vector, can be expressed as a function of two direction angles $0 \leq \Lambda \leq 2\pi$ and $0 \leq \Gamma \leq \pi$:

$$\vec{k} = k \begin{pmatrix} cos(\Lambda)sin(\Gamma) \\ sin(\Lambda)sin(\Gamma) \\ cos(\Gamma) \end{pmatrix}. \tag{3.59}$$

The amplitude vector $\vec{E}_0$ finally has to be transformed using rotation matrices (section 3.2.2) and the angles defining the wave vector Λ and Γ.

Since the particle is moving with respect to the wave source, the longitudinal Doppler-effect needs to be accounted for. Resonant absorption occurs if the angular wave frequency is:

$$\omega_{wave} = \frac{l\Omega_{ce}}{\gamma} \pm \underbrace{k_{||}v_{||}}_{Doppler-broadening}, \tag{3.60}$$

where l is the harmonic number, γ is the relativistic factor (≈ 1 in CNT) and Ω_{ce} is the electron cyclotron frequency (eq. 2.10). The second term is the Doppler-broadening term with $k_{||}$ being the wave-number parallel to the magnetic field and $v_{||}$ being the particles' parallel velocity. The sign denotes whether the particle is moving towards the source (+) or away from it (-).
Since $\Omega_e = f(B)$ is a function of the magnetic field, the condition is only fulfilled at certain coordinates $\vec{r}$. The microwaves in CNT have a frequency $f = 2.45\ GHz$ such that eq. 3.60 is fulfilled for the on-axis magnetic field $B_0 = 87.5\ mT$.
The cut-off density n_{co} (eq. 2.88) for waves of said frequency is:

$$n_{co}(\omega \approx 1.5 \cdot 10^{10}\ Hz) \approx 7.5 \cdot 10^{16}\ m^{-3}.$$

Comparing this density with the results in Fig. 1.3, we can see that the measured densities for these specific experiments were below the cut-off density (for O-mode waves). Subsequent experiments focused on overdense microwave heating. Here, certain wave modes cannot propagate in the plasma and therefore mode conversions were facilitated, so that waves can propagate and further heat the plasma. [60]

Recent experiments showed that the first-pass absorption of microwaves in CNT is very low and the incident waves are typically reflected several times on the vessel walls before being absorbed. [21] It can therefore be assumed that the field is isotropic and unpolarized. In a simulation, the angles θ (eq. 3.58), Λ and Γ (eq. 3.59) as well as a random phase φ (eq. 3.55) can thus be randomized at the start of a simulation and fixing them for the rest of the simulation, such that the electric field only depends on the space $\vec{r}$ and time t.

The intensity of the wave was estimated using the coupled power of the microwave source divided by the area of the entry port window. The power of the source was $P_{wave} = 1\ kW$. However, due to the rudimentary set-up, it is believed that at most half of this power, $P_c \approx 500\ W$, actually coupled to the plasma.

The entry window had a diameter of $d \approx 25\ cm$. The initial estimate for the waves' intensity is thus:

$$I = \frac{P_c}{A} \approx 10\ \frac{kW}{m^2}. \tag{3.61}$$

The amplitude of the wave follows from eq. 3.2:

$$E_0 = \sqrt{\frac{2I}{c\varepsilon_0}} \approx 2770\ \frac{V}{m}. \tag{3.62}$$

This approach is only a crude estimate of the real wave intensity, which was not measured. The influence of the intensity as a parameter was studied in section 4.5.4.

The operation of the microwaves was done in pulses of $\tau_{pulse} \approx 6\ ms$ at a repetition rate of $f \approx 60\ Hz$. The time for an interval is $\tau_i = \frac{1}{f} \approx 16.6\ ms$, meaning that the heating will be activated for roughly 6 ms and then be deactivated for $\tau_i - \tau_{pulse} \approx 10.6\ ms$ before being switched on again.

4. Results

In this section, the approaches from chapter 3 are investigated and the results presented.

A flowchart of the final code, including all modules and a short description of their function, is given in Appendix C.

4.1. Emission current from filament

The emission current density from the filament (eq. 3.1) as a function of time is shown in Fig. 4.1. The blue line is the current obtained from the thermionic emission as well as the electric field introduced by the bias voltage E_b (eq. 3.7) of:

$$E_b \approx 2 \cdot 10^5 \ \frac{V}{m}.$$

The orange line additionally includes the wave electric field E_w, modelled as a sinusoidal wave:

$$E_w = E_0 sin(\omega \cdot t), \tag{4.1}$$

with the magnitude E_0 from eq. 3.3:

$$E_0 \approx 3.9 \cdot 10^3 \ \frac{V}{m}$$

and the angular frequency ω of the microwaves:

$$\omega = 1.54 \cdot 10^{10}.$$

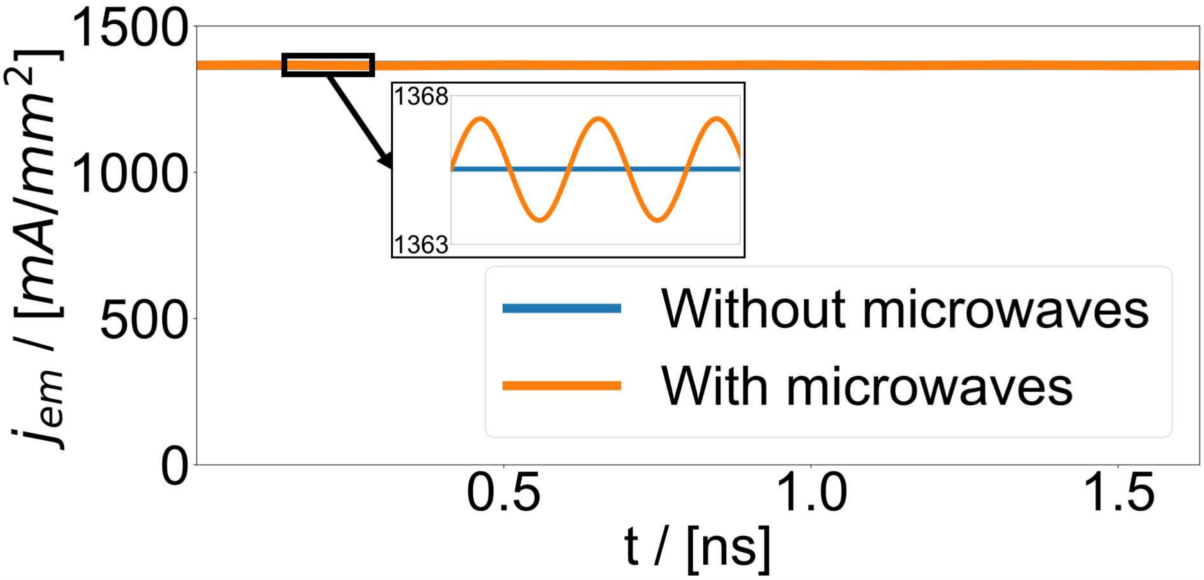

Figure 4.1: Emission current density from the emissive filament. The blue line is the current density in the absence of the wave electric field. The orange line includes the wave electric field.

Fig. 4.1 shows clearly that the added effect of the microwave electric field is very minuscule, even under very optimistic assumptions. Comparing the emission current density in the absence of the microwaves, j_0, with the maximal current in the presence of the microwaves j_w gives:

$$\frac{j_{wave;max}}{j} < 1.002.$$

The maximal added effect is smaller than 0.2 %. In reality, this effect is likely even smaller.

It can be concluded, that this candidate mechanism cannot explain the synergistic effects observed and can be discarded.

4.2. Particle tracing

4.2.1. Orbit comparison GCM to particle motion

Initially, most processes were tested in a simplified model; namely a homogeneous magnetic field pointing in the z-direction, $\vec{B} = B_0 \cdot \hat{e}_z$, rather than using the more complex magnetic field of CNT. This enables the isolation of any potential errors. Additional levels of complexity were subsequently added step-by-step in order to more closely simulate the physics of the CNT experiments.

The first step was to verify that the equations of motion are solved correctly. Fig. 4.2 shows the orbit of a single particle (blue line) in the uniform magnetic field. A magnetic field line is shown by the black, dotted line. Since the field is homogeneous, the GCM (red line) coincides with the magnetic field line.

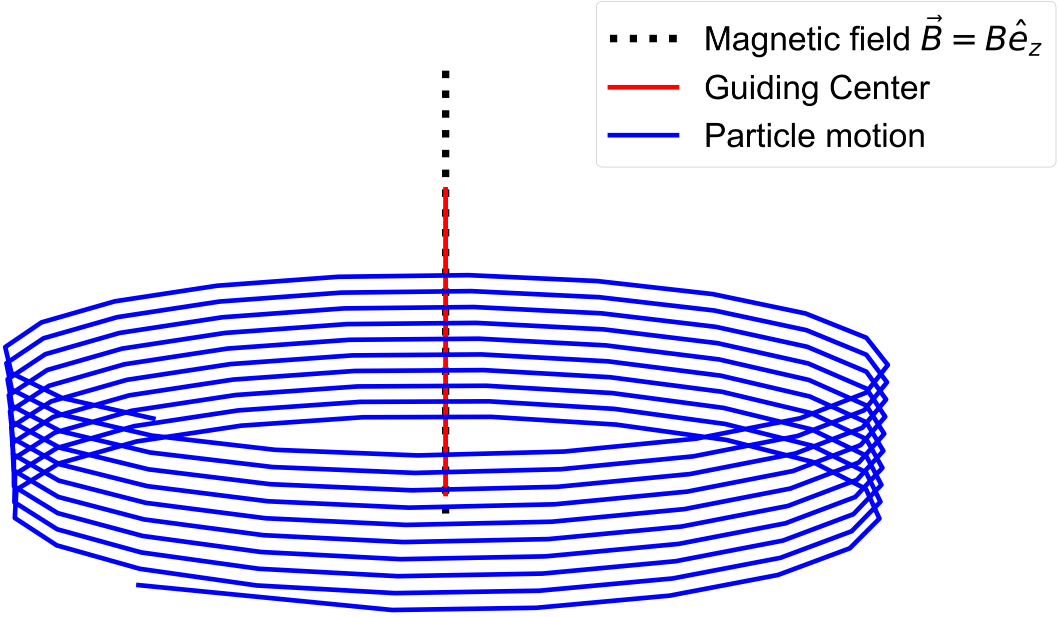

Figure 4.2: Particle motion (blue line) and Guiding Center motion (red line) in a homogeneous magnetic field $\vec{B} = B\hat{e}_z$. A magnetic field line is schematically shown in black.

In this first example, it is not really possible to verify that the Guiding Center-EOMs are solved correctly, as there is neither a curvature nor a gradient of the magnetic field present. To verify that both approaches deliver the same results, the orbits in CNT's magnetic field were compared. Fig. 4.3 shows the orbit of a particle (blue line) and its GCM (red line) in CNT. The CNT coils are shown in black. The particle had an initial energy of $E_{ini} = 5\ eV$ and a pitch-angle $\alpha = 15°$. Its starting position $\vec{r}_{ini}$ was:

$$\vec{r}_{ini} = \begin{pmatrix} 0 \\ 0.2 \\ 0 \end{pmatrix} m.$$

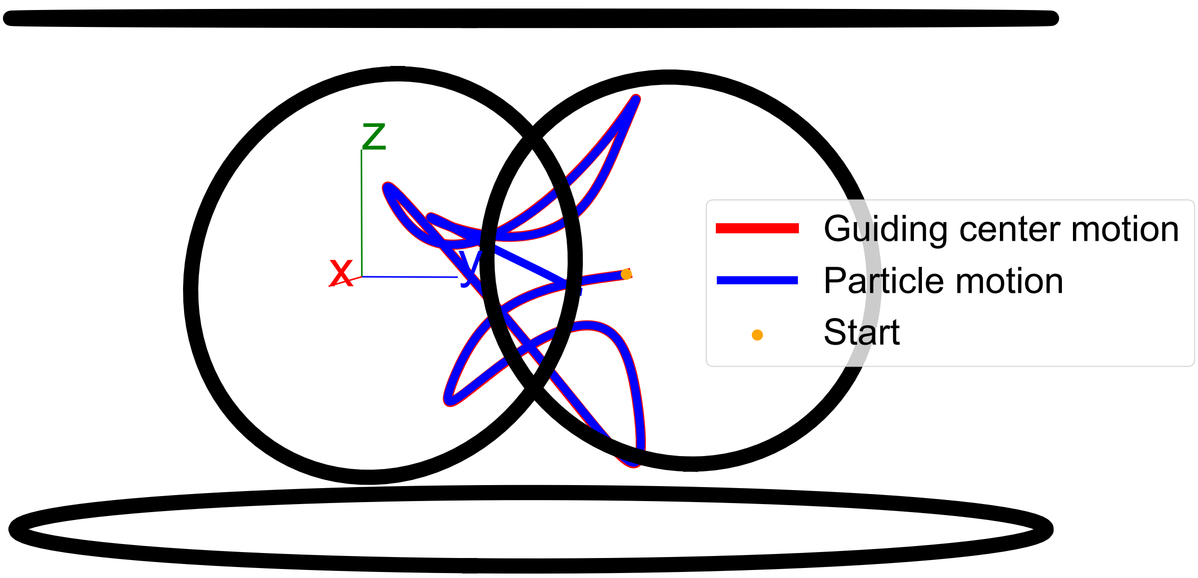

Figure 4.3: Orbit comparison of the particle motion (blue line) and the GCM (red line) in CNT's magnetic field. The CNT coils are depicted in black.

Fig. 4.3 shows that the trajectories follow the same path, at least to the limits of resolution used. Fig. 4.4 shows a close-up for the orbit at the beginning. The particle trajectory (blue) spirals nicely around the guiding center (red); confirming the expected results.

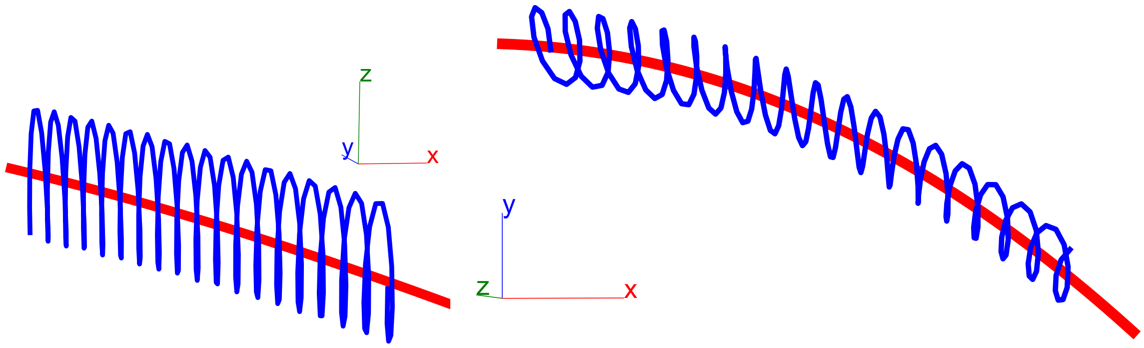

(a) Side view of the comparison GCM to particle motion.

(b) Aerial view of the comparison GCM to particle motion.

Figure 4.4: Close-ups of the orbit comparison between the GCM (red line) and the particle motion (blue line) from Fig. 4.3.

As mentioned previously, a major advantage of the GCM is the improved time-efficiency due to bigger step-sizes possible. However, despite the increased CPU-time necessary for simulating the single particle motion, the decision was made to favour solving the particles' motion rather than the GCM. The reason for this was in part because particle collision are easier to implement in the particle model (without loss of information due to averaging) as well as an easier implementation of the microwave heating.

4.2.2. Step size analysis

A study to find the optimal step size dt was performed. The ideal step size should be as big as possible (to reduce computation time) but also small enough for systematic or rounding errors to have little impact.

The step size dt was studied by tracing several particle for a fixed amount of time $t = 100\ \mu s$, with each simulation having a different step size. Since no collisions or electric fields are present, the energy of the particle should be constant $E = const.$

Fig. 4.5 shows the energy history for a few selected step sizes. It is immediately obvious that in the case $dt = 40\ ps$ the error is intolerably high.

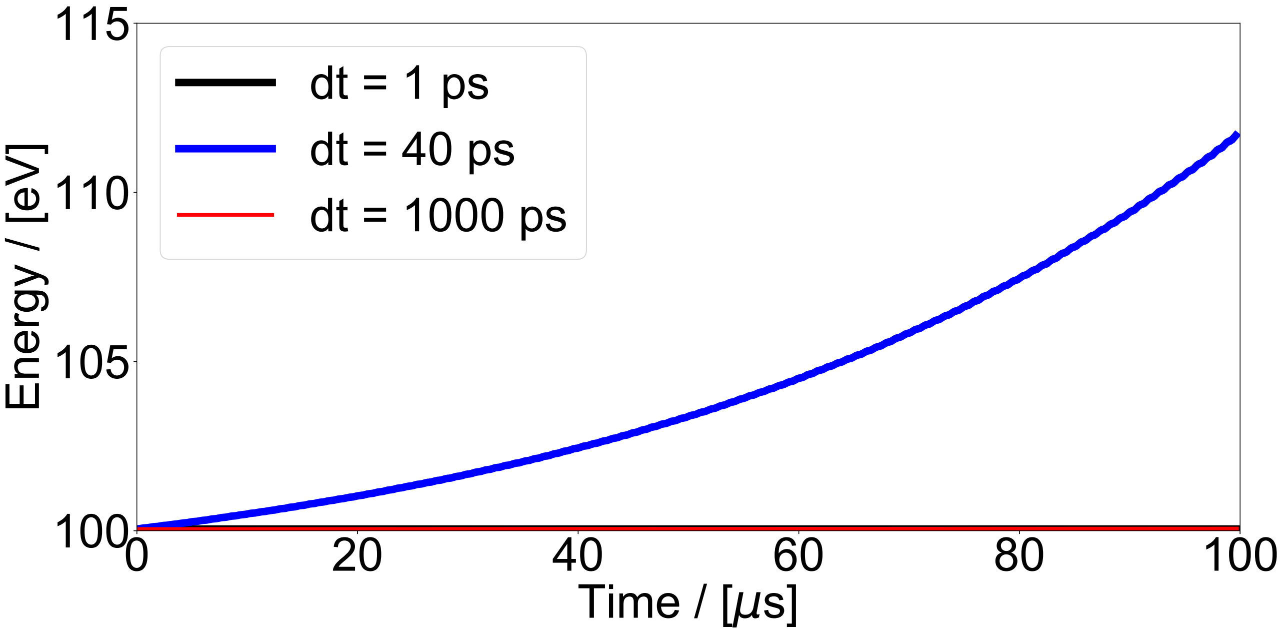

Figure 4.5: Energy history for particles with same initial conditions but different step sizes.

A criterion to compare uncertainties of different step sizes was introduced by taking the ratio

$$r = \frac{E(t = 100\ \mu s)}{E(t = 0\ \mu s)}.$$

Fig. 4.6 shows the ratio r for a range of step sizes dt.

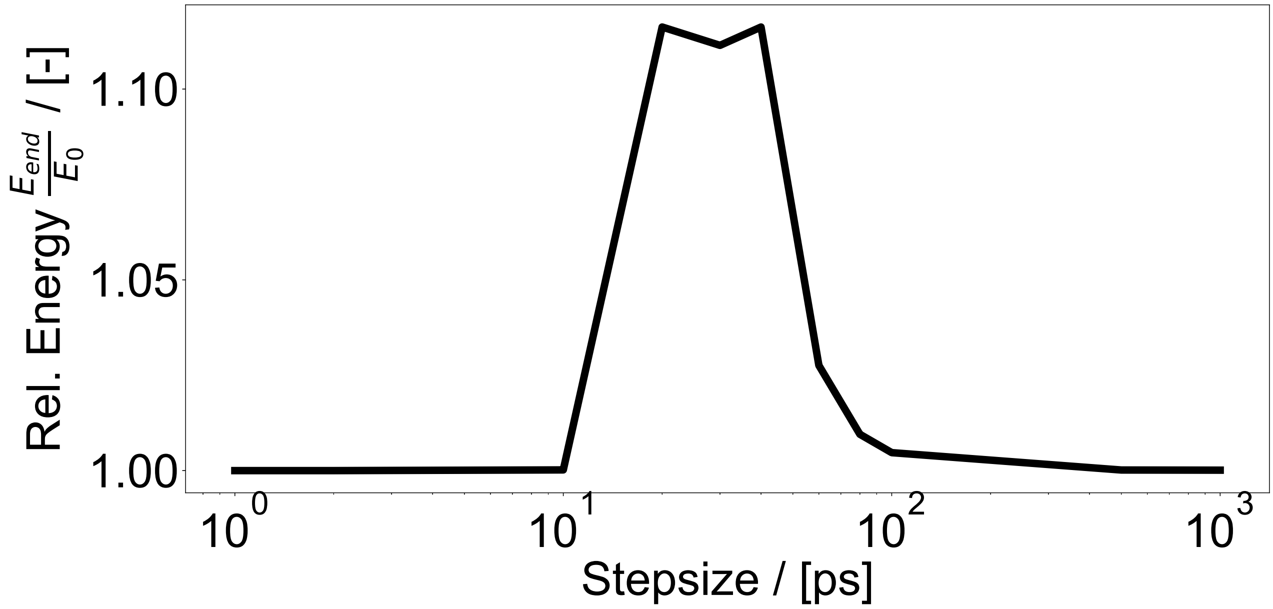

Figure 4.6: Ratio of energy after $t = 100\ \mu s$ to initial energy as a function of the step size used.

The different segments of Fig. 4.6 can be interpreted as follows:

- $1\ ps \leq dt \leq 10\ ps$: The solution is stable; with the end energy $E(t = 100\ \mu s)$ being only $10^{-11}\%$ larger than the initial energy $E(t = 0\ \mu s)$.
- $10\ ps < dt \leq 100\ ps$: Step sizes in this range are comparable to the duration of one gyro-motion τ_c:

  $$dt \approx \tau_c = \frac{1}{\omega_{ce}},$$

  and thus too few points are calculated during a single gyromotion; rendering the solution unstable. After the (relatively) short time of $100\ \mu s$, the energy of the particle has increased by about 10 %, compared to its initial energy.

  The numerical error in this segment is intolerable and such step sizes should be avoided.
- $dt > 100\ ps$: Step sizes in the range don't resolve the gyromotion of the particle. Comparing the particle position obtained using step sizes from this range to the position obtained from step sizes in the stable region shows that the position is still surprisingly accurate, to within $10^{-12}\ m$.

  Taking larger step sizes might be used as an alternative to the guiding center approach, if only the unperturbed particle orbit is of interest.

It was subsequently concluded that in simulations where particle phenomena; such as influence of collisions as well as particle-microwave interaction; are of interest, the optimal step size is

$$dt = 10\ ps = 10^{-11}\ s.$$

4.3. Magnetic field Poincaré-Plots

A Poincaré-Plots (section 3.2.4) of electrons in CNT is shown in Fig. 4.7. Each single contiguous magnetic surface represents the trajectory of an electron with an energy $E_{ini} = 5\ eV$ and its initial position in the range of:

$$0.2\ m \leq x_{initial} \leq 0.3\ m$$
$$y_{initial} = z_{inital} = 0\ m.$$

Each single plot shows a 2D-cut in the r/z-plane. The angle ϕ in the x/y-plane as well as the position in relation to the coils (blue line) is indicated above each plot. Because of mirror-symmetry, the results of only one half-period ($0° \leq \phi \leq 90°$) of the plasma are shown.

The LCFS is denoted by the black dots. Particles beyond this surfaces will not be confined; thus no particle orbit computation beyond the starting position of these orbits were performed.

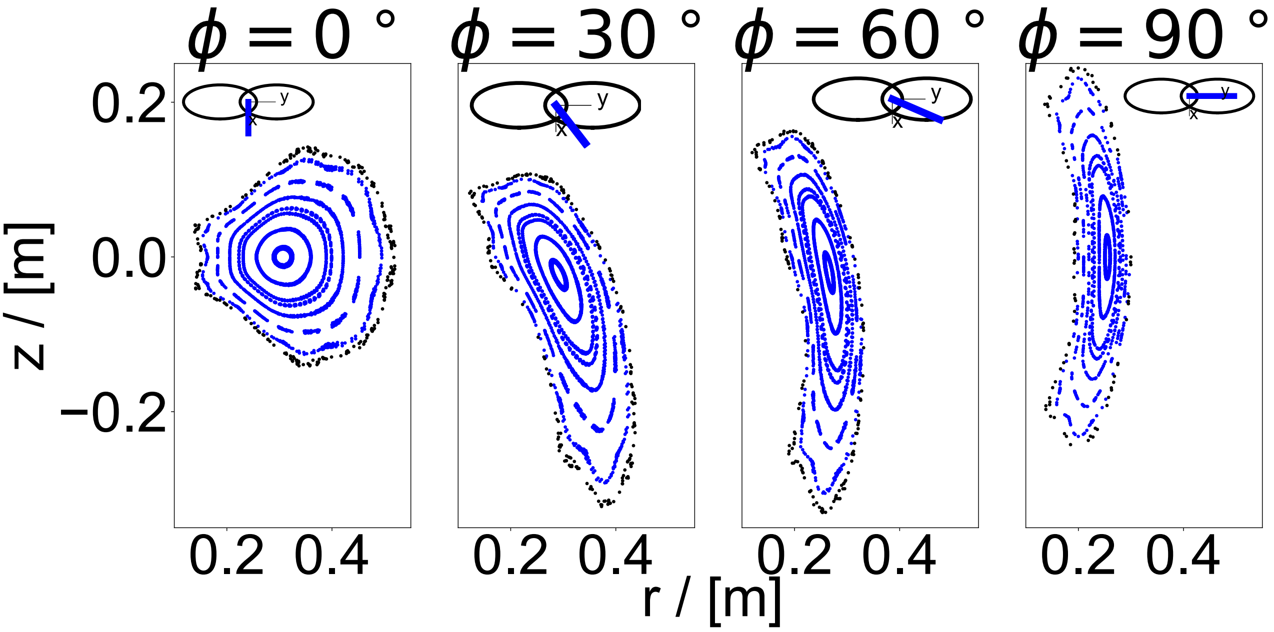

Figure 4.7: Poincaré-Plots for electron orbits in CNT. The angle ϕ marks the position of the cut plane in the xy-plane. Only one quartile ($0° \leq \phi \leq 90°$) is shown; the results for the other quartiles are mirror images of these plots. The black dots mark the LCFS.

4.4. Collisions

4.4.1. Electron-electron collisions

The effects of electron-electron collision onto the test particles' orbit in a homogeneous magnetic field is depicted in Fig. 4.8: The image shows an aerial xy-view, with the particles' (x, y)-coordinates in color.

The black line shows the unperturbed particle orbit, the blue line the particle orbit using the single, Rutherford collision models and the red line the particle orbit using the Fokker-Planck approach. As the test particle undergoes collisions, its Larmor radius r_L (eq. 2.9) will change with changing pitch-angle α (eq. 2.17). In the collision-less case (black), the radius is $r_L = const$. For the collisional cases, the radius is constantly changing. Since the collisions are random, the simulation will deliver different results every time it is performed and a single simulation cannot be used to quantify/compare the two collisional approaches.

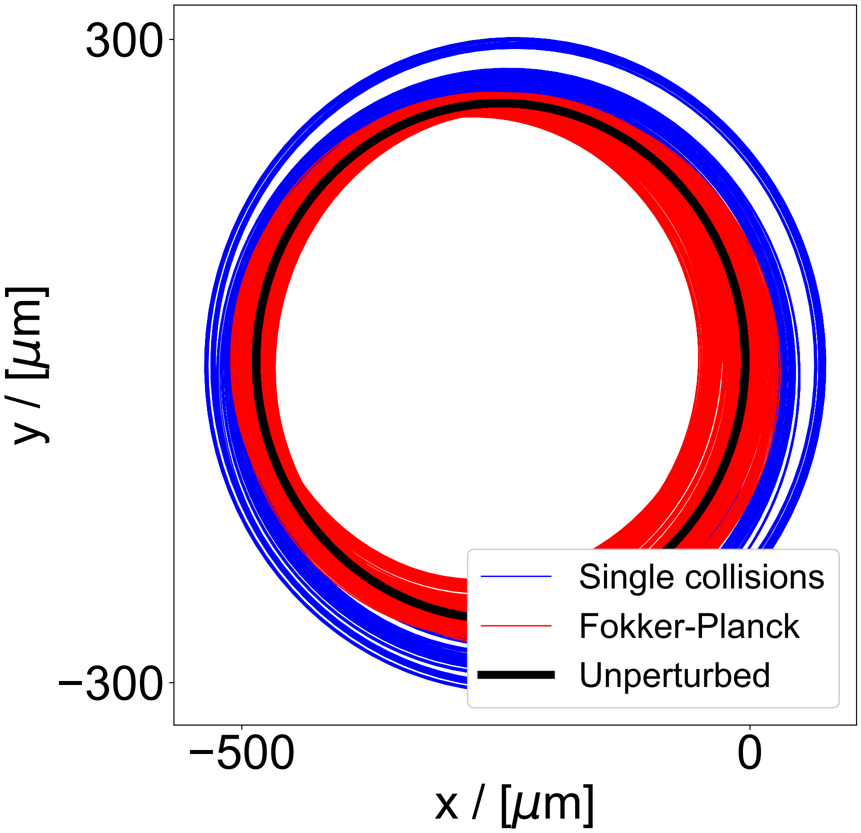

Figure 4.8: Aerial view of particle trajectory in uniform magnetic field $\vec{B} = B\hat{e}_z$. Under the influence of electron-electron collisions, the particles' trajectory is altered.

To quantify the effect of the collisions, the electron thermalization time τ_E^{ee}; being the time after which an electron's energy has dropped to $\frac{1}{e}$ of its initial value, was computed. It is comparable to the time for a significant deflection $\tau^{ei}_{90^\circ} = \frac{1}{\nu^{ei}_{90^\circ}}$: [52]

$$\tau^{ei}_{90^\circ} \approx \tau^{ee}_{E}.$$

For CNT, the time $\tau^{ei}_{90^\circ}$ was estimated to be: [60]

$$100\ \mu s \leq \tau^{ei}_{90^\circ} \leq 1\ \mu s.$$

Fig. 4.9 shows the energy history as a function of elapsed time for electrons affected by collisions using the Rutherford single collision model. In total, the energy history of 50 single electrons was computed. The electrons had identical initial positions and starting energies of $E_{init} = 100\ eV$.

The time for each single electrons' energy to drop below $\frac{1}{e}E_{init}$ was evaluated. The resulting mean thermalization time was

$$\tau^{ee}_{e,single} = (26.4 \pm 13.4)\ \mu s,$$

which lies within the previously estimated range.

It is noteworthy that the energy history is not very smooth but rather dominated by single, bigger energy losses. Fig. 3.6 helps explain this phenomenon: Most impact parameters will lead to very small deflection angles θ, resulting in negligible energy losses. Only very small impact parameters will lead to significant deflections and thus notable energy losses.

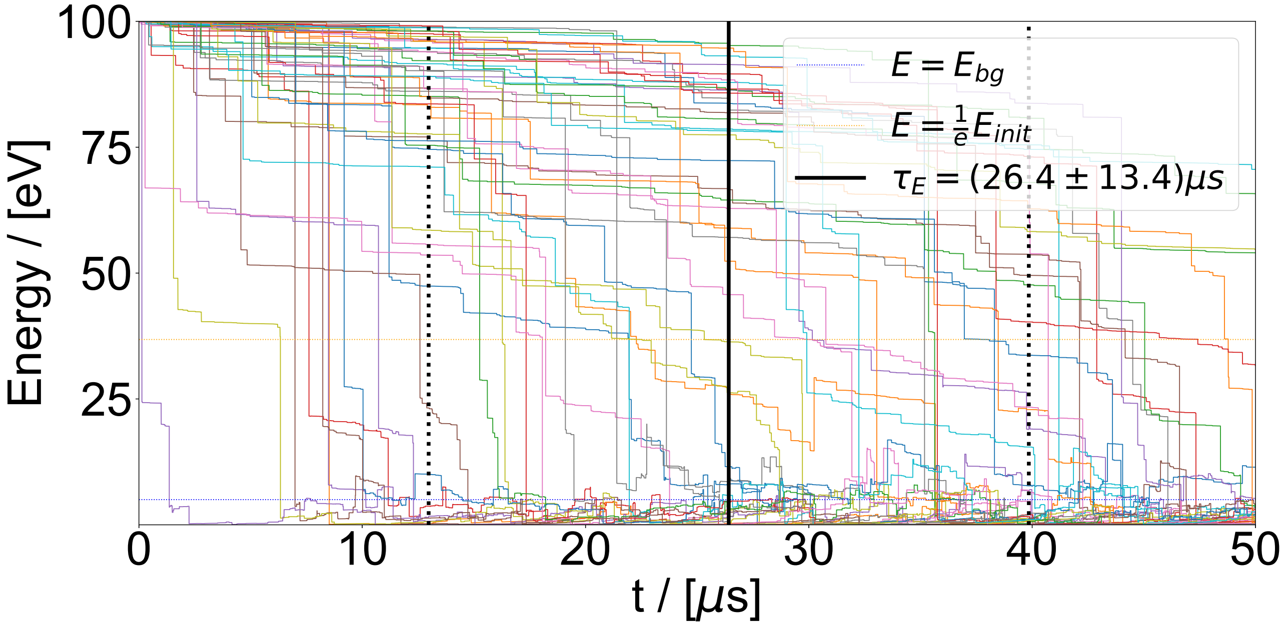

Figure 4.9: Energy history over time under the influence of electron-electron collisions. The approach of single, Rutherford electron-electron collisions was used for this study. A total of 50 single particles with identical initial energies (lines with different colors) were traced and the mean thermalization time τ_E was evaluated. The mean of τ_E is marked by a black vertical line, its uncertainty is marked by the black dotted lines.

Fig. 4.9 shows the same evaluation using the Fokker-Planck collisional approach. Here, a total of 30 single electrons with the same initial parameters as in the previous case were traced. Using this approach, the average thermalization time was:

$$\tau^{ee}_{e,FP} = (20.6 \pm 11.2)\ \mu s.$$

The value agrees well with the one obtained from the Rutherford collision approach and also lies within the expected boundaries.

The resulting energy history is a lot smoother and more closely resembles a random-walk process.

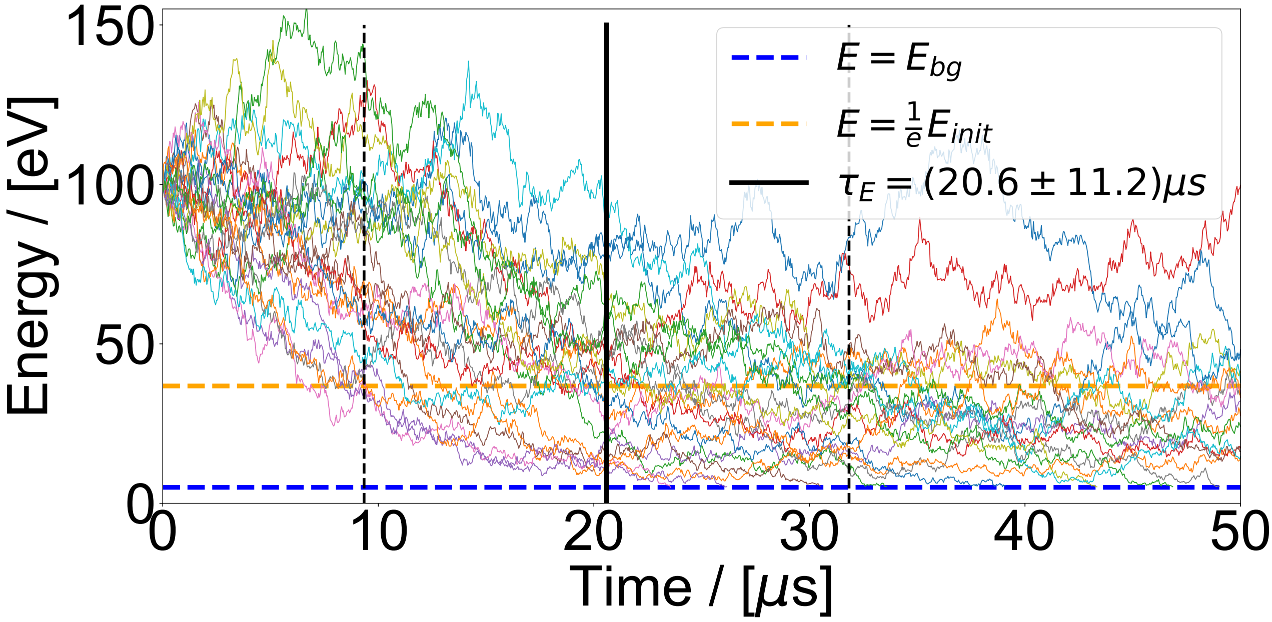

Figure 4.10: Energy history over time under the influence of electron-electron collisions. The Fokker-Planck collisional approach was used for this study. A total of 30 single particles with identical initial energies (lines with different colors) were traced and the mean thermalization time τ_E was evaluated. The mean of τ_E is marked by a black vertical line, its uncertainty is marked by the black dotted lines.

4.4.2. Electron-ion collisions

Collisions between electrons and ions will mostly scatter the electrons without (significant) energy transfer. Fig. 4.11 shows the same situation as in Fig. 4.8, except for the particle being subject to electron-ion collisions rather than electron-electron collisions. Due to the scattering, the pitch-angle α and subsequently the Larmor-radius r_L will slowly change. However, since the kinetic energy is (almost) constant, r_L will not change as drastically as in Fig. 4.8.

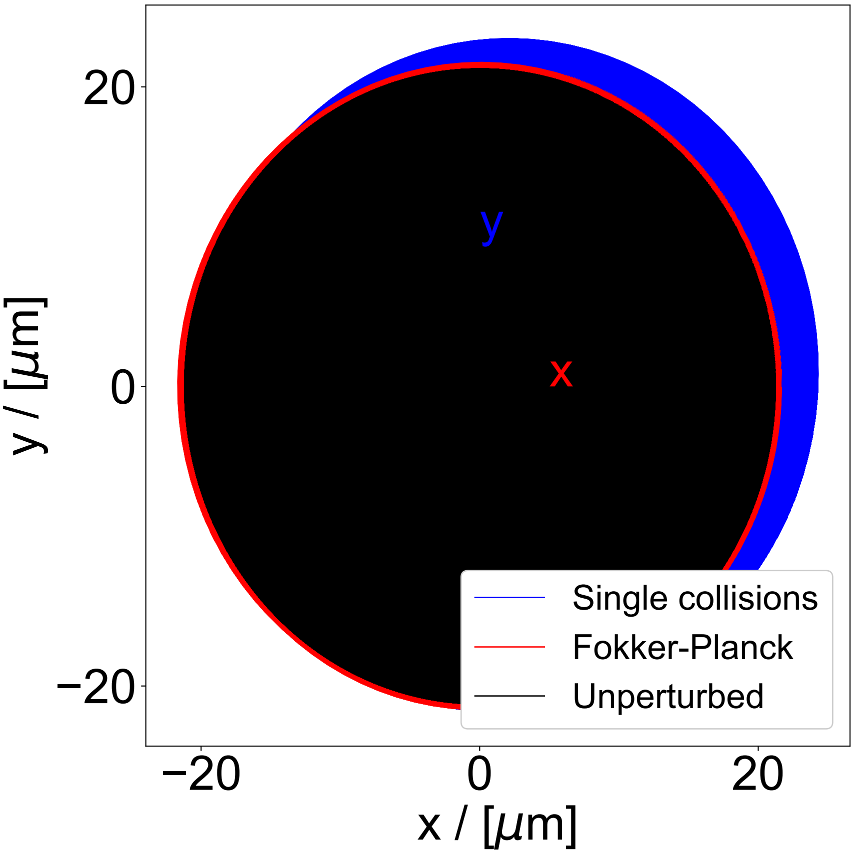

Figure 4.11: Same situation as in Fig. 4.8, expect for the electron to be subject to electron-ion collisions only.

Because of the easier formulation of the Fokker-Planck approach as well as the ability to easily include collisions between both types of particles simultaneously, this approach was favoured over the Rutherford single collision approach and was used from here onwards.

4.4.3. Effects on Poincaré-Plots

Fig. 4.12 shows a plot similar to Fig. 4.7 - a Poincaré-plot of a single electron. The particles' initial energy was $E_{init} = 100\ eV$ and its initial position was $\vec{r} = \begin{pmatrix} 0.28 \\ 0 \\ 0 \end{pmatrix}\ m$; close to the starting position leading to the LCFS in Fig. 4.7. The blue dots mark the trajectory of the unperturbed orbit, the black dots mark the trajectory under the influence of electron-ion (EI) collisions, and the red dots include the electron-electron (EE)-collisions. In both cases, the Fokker-Planck approach was used to model the collisions.

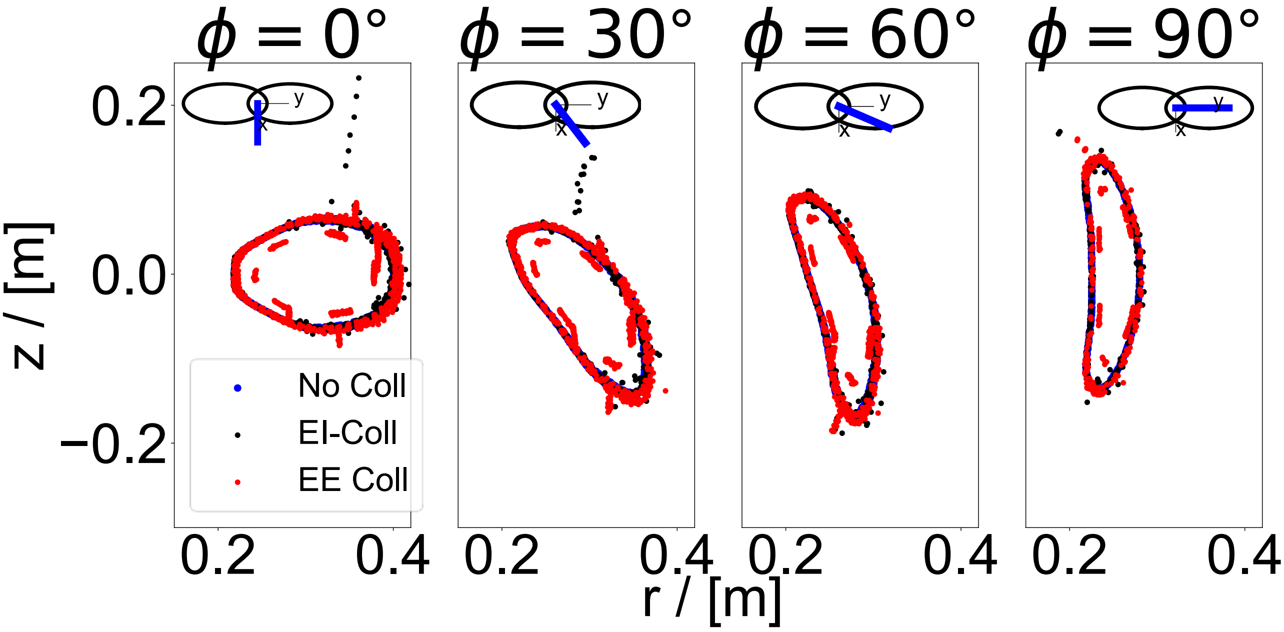

Figure 4.12: Poincaré-plot similar to Fig. 4.7, but in the presence of collisions with ions (black) or with other electrons (red), illustrating the deviation from non-collisional Poincaré plots (black).

An important difference between Fig. 4.12 and Fig. 4.8 and Fig. 4.11 is the non-uniform magnetic field: The particle will be scattered into regions with different magnetic fields, altering the orbit which eventually leads to the particle escaping confinement. This can be seen by the black dots leaving towards the top in Fig. 4.12. The blue dots from the collisionless case are hardly visible beneath the other dots; however, its main distinction is that here the particles are confined. Consequently, no blue dots can be found outside the interior, circular region.

Due to the energy loss, the particle under the influence of EE-collisions will experience magnetic mirror effects (section 2.3.1): As the particle loses energy (and consequently perpendicular velocity $v_\perp$), it can be reflected at regions with higher magnetic field strengths; despite not being reflected before. In Fig. 4.12, this is visible by the non-contiguous strips of dots inside the unperturbed surface - rather than following a full magnetic surface, the particle is reflected at certain positions. A close-up in 3D-geometry is shown in Fig. 4.13: At regions with magnetic fields, the particles is reflected and the particle will travel back in the direction it came from.

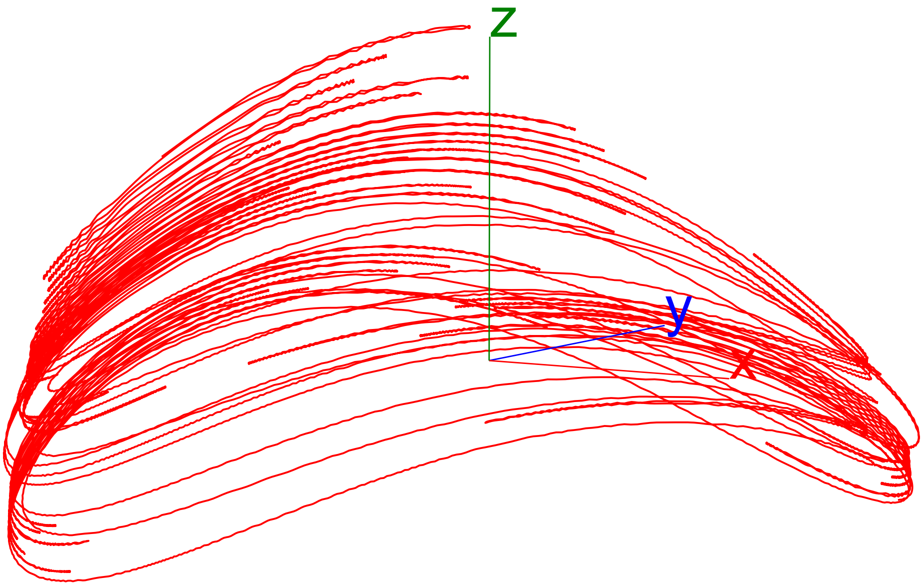

Figure 4.13: Electron orbit under the influence of electron-electron collisions. Due to decreasing energy, at locations with high magnetic fields the particle is reflected.

4.5. Microwave heating

The theory of microwaves and their propagation in a plasma as well as their different modes were introduced in section 2.6.2.

The modelling procedure was described in section 3.2.12 and has many parameters: The polarization angle θ, the wave phase angle φ, the angles defining the direction of propagation Γ and Λ as well as the waves' intensity I. For the intensity estimates were made. The other parameters are assumed to be random in their respective parameter range.

As in the case with collisions, modelling the influence of the microwaves was initially investigated using a simplified model with a homogeneous magnetic field $\vec{B} = B_0\hat{e}_z$.

First, the two main modes of wave propagation, O-mode and X-mode, were studied (sections 4.5.1 and 4.5.2). The next step was to study wave propagation parallel to the magnetic field in section 4.5.3. Finally, the aforementioned random parameters defining the wave were varied and their influence studied (section 4.5.4).

Particle momentum in presence of electric field The change in momentum of an electron in the presence of the electric field is given by

$$\frac{d\vec{p}}{dt} = -e\vec{E}. \tag{4.2}$$

Due to the negative charge sign, the relative phase between the particles' velocity and the electric field in order for optimal absorption to take place needs to be π.

4.5.1. X-mode heating

First, wave propagation perpendicular to the magnetic field is investigated ($\Gamma = \pi/2$). In the case of X-mode waves, the polarization angle is $\theta = 0$. The waves' phase-angle was $\varphi = 0$. In relation to the background magnetic field $\vec{B}_0$, the wave vector $\vec{k}$ and the wave electric field $\vec{E}_w$ were perpendicular:

$$\vec{k} \perp \vec{B}_0; \vec{E}_w \perp \vec{B}_0.$$

In the present model, the wave propagates in the y-direction $\vec{k} = k\hat{e}_y$ and the electric field oscillates in the x-direction $\vec{E}_w = E_w\hat{e}_x$. Since the field oscillates perpendicular to the magnetic field, only the perpendicular velocity component $v_\perp$ is affected by the field.

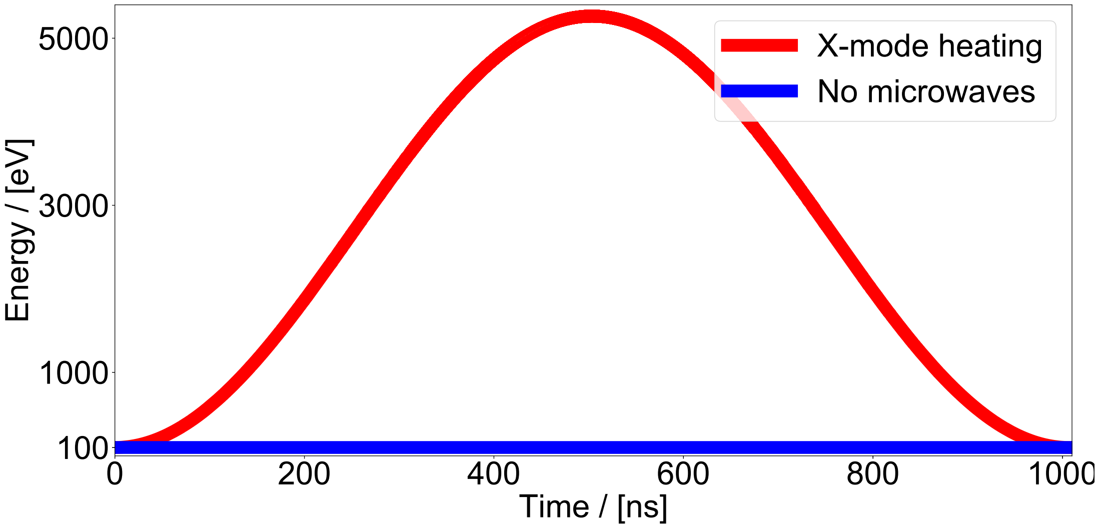

Figure 4.14: Energy history for a particle under the influence of a X-mode electromagnetic wave (red line). The blue line is the energy of a particle in the absence of microwaves.

Fig. 4.14 shows the energy as a function of time for two particles. The blue line depicts an electron in the absence of an electric field, the red line an electron in the presence of the above mentioned X-mode waves. While the energy of the unperturbed electron stays constant at $E_0 = 100\ eV$, the heated electron gains energy, until a maximum after around

$t \approx 500\ ns$ has been reached before decreasing again. This oscillatory behaviour continues further, but only one oscillation period is shown.

Using eq. 4.2, this phenomenon can be explained: Initially, the particle and microwave are out of phase and thus the electron gains energy. As the particle gains energy, its Larmor radius r_L increases and with it, the distance to the source of the microwaves (located at the origin) increases. The total phase of the wave $e^{i(\vec{k}\cdot\vec{r}-\omega\cdot t)}$ will change with position $\vec{r}$. At $t \approx 500\ ns$, this term has caused the relative phase between particle and wave to vanish and the particle starts losing energy to the wave.

Fig. 4.15 illustrates this: The particles' polar angle (in the horizontal plane) is shown in black. The phase of the incident microwave electric field is shown in red. Fig. 4.15a shows the phases at the start of the simulation. The relative phase between the two is π and resonant heating occurs. Fig. 4.14 shows the phases at a later time point; centered around the location of the maximum energy at $t = 500\ ns$. Here, the relative phase is 0 and the electron loses energy.

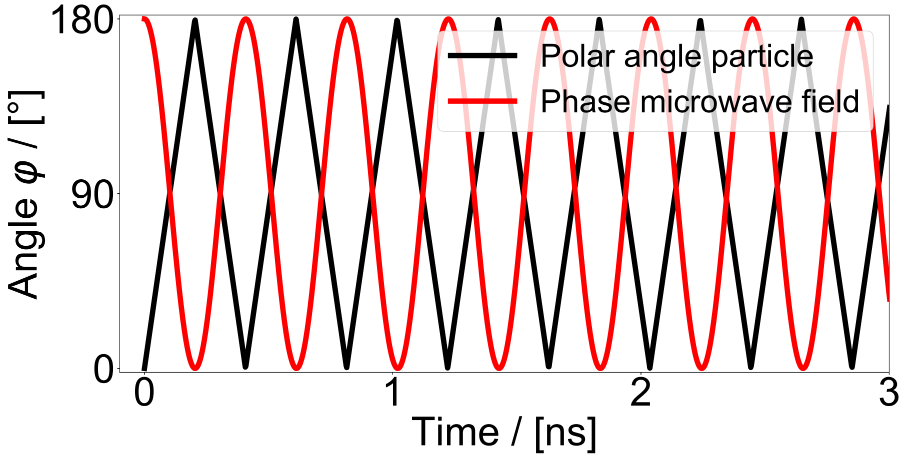

(a) Phase angle at the start of simulation.

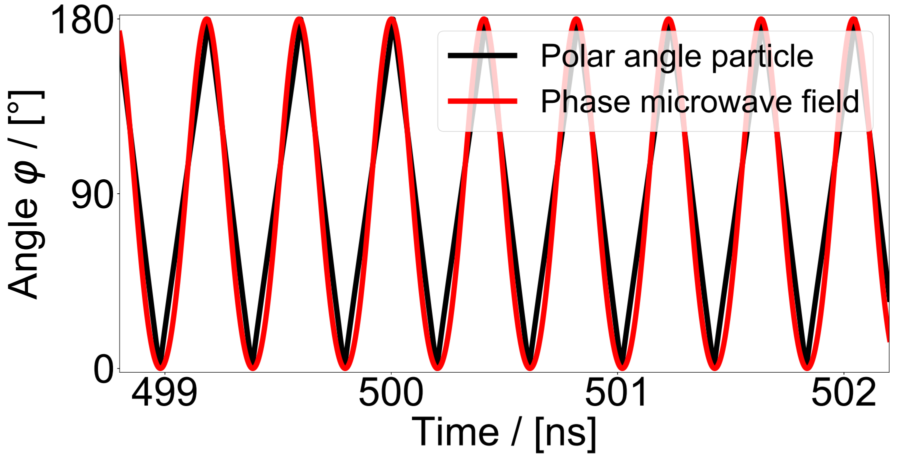

(b) Phase angle around $t \approx 500\ ns$, when the energy starts decreasing.

Figure 4.15: Polar angle of particle (black line) and phase angle of electric field (red line) as function of elapsed time.

4.5.2. O-mode heating

The (perpendicular) O-mode wave is characterized by its its electric field $\vec{E}_w$ being parallel to the magnetic field. In a first study, propagation perpendicular to the magnetic field was investigated:

$$\vec{k} \perp \vec{B}_0; \vec{E}_w || \vec{B}_0.$$

This is equivalent to a polarization angle of $\theta = \pi/2$. Here, $\vec{E} = E\hat{e}_z$ and heating only affects the parallel-component $v_{||} = v_z$ of the particles' velocity. The gyromotion takes place in the plane perpendicular to $\vec{B}_0$. During one oscillation of the wave, the particle gains as much energy (while $E_{w,z} < 0$) as it loses (while $E_{w,z} > 0$). This is exemplified in the small close-up in the upper left corner of Fig. 4.16. In addition to these fast oscillations there is also a long-range oscillatory behaviour, similar as in the X-mode case. The explanation for this behaviour is the same as for the X-mode case: The particle and the microwaves are initially in phase and the particle loses energy. The relative phase slowly shifts (with increasing $\vec{k} \cdot \vec{r}$) until the two are out of phase and the particle starts gaining energy. Once the relative phase is 0, the energy starts decreasing again.

An interesting observation is that the oscillation period in Fig. 4.16 (O-mode) seems to be half as long as in Fig. 4.14 (X-mode).

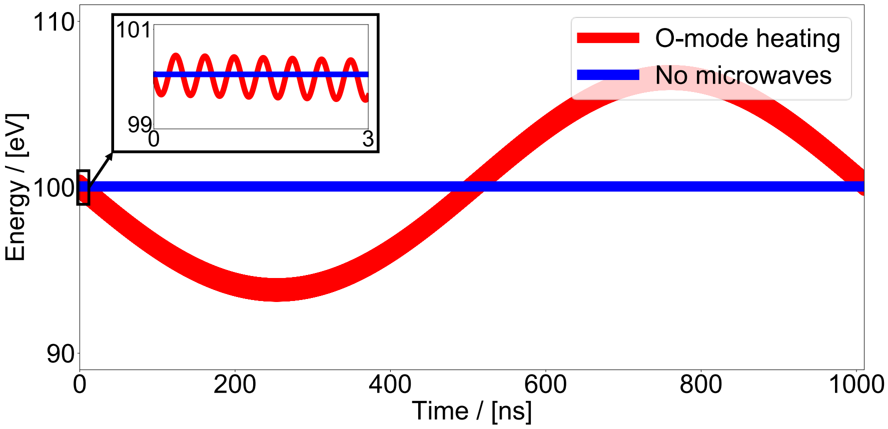

Figure 4.16: Energy history for a particle under the influence of an O-mode electromagnetic wave (red line). The blue line is the energy of a particle in the absence of microwaves.

4.5.3. Propagation parallel to magnetic field

In the case of parallel propagation ($\Gamma = 0$),

$$\vec{B}||\vec{k} = k\hat{e}_z,$$

the Doppler-shift needs to be accounted for. It can be derived from eq. 3.60 and is:

$$\omega = \omega_0 + k_{||}v_{||}. \tag{4.3}$$

In the previous studies there was no parallel-component of the wave-number $k_{||}$ and subsequently no (parallel) Doppler shift.

To study this mode of propagation, parallel X-mode waves were injected ($\theta = \pi/2$). The resulting particles' energy history is practically identical to Fig. 4.14, where perpendicular X-mode waves were injected. Therefore, it is not shown again.

To explain the (almost) identical results, compare the Doppler-shifted component $k_{||} \cdot v_{||}$ to the waves frequency ω_0:

$$\omega_0 = 2\pi \cdot 2.45 \cdot \;\; GHz \approx 14\; Ghz >> k_{||} \cdot v_{||} \approx 0.24\; GHz.$$

The Doppler-shift term is two orders of magnitude smaller than ω_0. Compared to the case of parallel propagation, the electric field will oscillate marginally faster, but the impact is hardly felt by the particle and therefore the energy histories are almost identical.

Since the Doppler-shift depends on the particles' parallel velocity, the effect is generally even smaller for less energetic particles.

4.5.4. Parameter variation

To study and compare the effect of heating with a given set of parameters, a criterion was introduced. This criterion is the slope of the energy-curve at the beginning of the curve (see for instance Fig. 4.14, 4.16):

$$\frac{dE}{dt}|_{t=t_0} = \frac{E(t_1) - E(t_0)}{t_1 - t_0}. \tag{4.4}$$

A constant time differential of $dt = t_1 - t_0 \approx 10\; ns$ was chosen, with $t_0 = 0\; ns$.

Polarization angle θ The polarization angle takes on values $0 \leq \theta \leq \frac{\pi}{2}$. The two extremal cases are the X-mode ($\theta = 0$) and the O-mode ($\theta = \pi/2$).

Using the heating criterion introduced in eq. 4.4, the heating as a function of the polarization angle θ is shown in Fig. 4.17. The initial particle energy was $E_{ini} = 100\; eV$.

X-mode heating is the most efficient, while O-mode heating even results in cooling (initially).

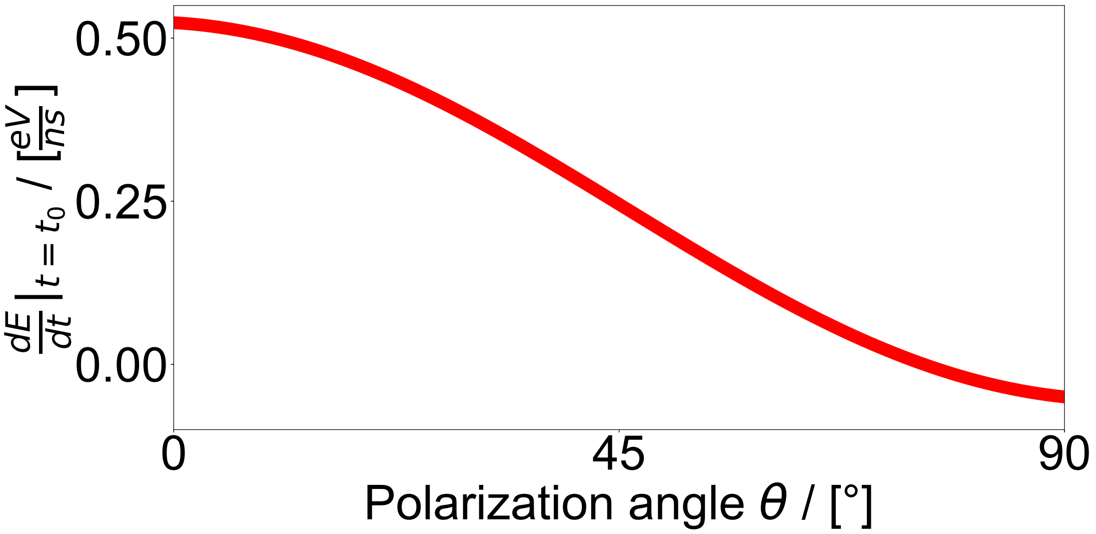

Figure 4.17: Heating power $\frac{dE}{dt}$ as a function of the polarization angle θ.

Angle Γ between $\vec{k}$ and $\vec{B}_0$ The angle Γ between the wave vector $\vec{k}$ and the magnetic field $\vec{B}_0$ was varied:

$$0 \leq \Gamma \leq \pi/2$$

The particles' initial energy was $E_{ini} = 100\ eV$ and the polarization angle was $\theta = 0$ (X-mode). An angle of $\Gamma = 0$ corresponds to the parallel propagation presented in the previous section 4.5.3, while an angle of $\Gamma = \pi/2$ corresponds to the perpendicular X-mode (section 4.5.1).

The heating power as a function of the angle Γ is shown in Fig. 4.18. The scale indicates that the direction of propagation hardly affects the heating power. An argument to explain this observation is very similar to the one already given in the previous section: The Doppler-shift, which changes as a function of $k_{||} = f(\Gamma)$, has only a very minor impact on the waves' angular frequency ω and thus the overall effect is only very small.

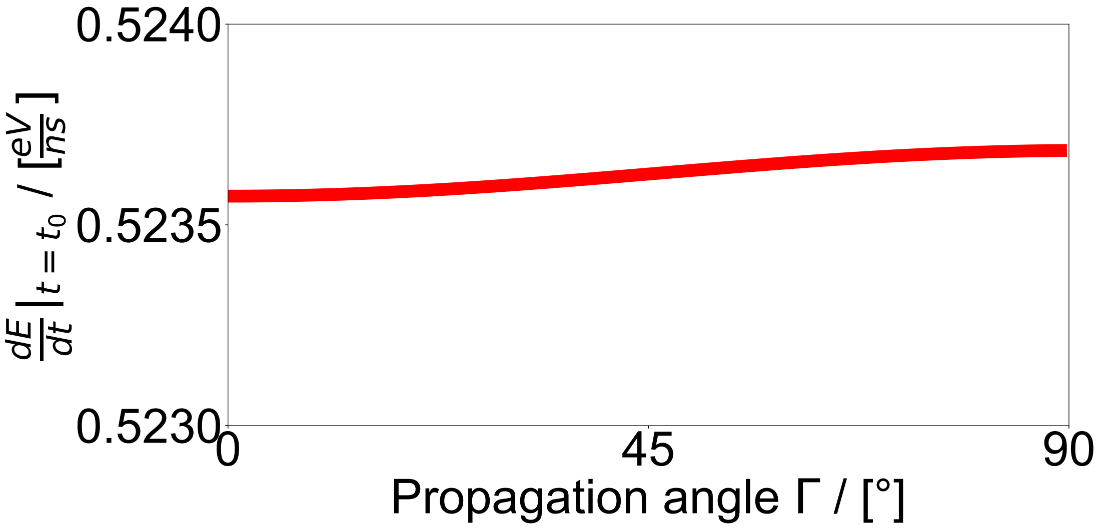

Figure 4.18: Heating power $\frac{dE}{dt}$ as a function of the angle of propagation of k Γ in the yz-plane.

Particles' initial energy E_{ini} The next parameter to be varied was the particles' initial energy E_{ini}. This ultimately relates to the synergy, as in theory, more energetic particles should absorb the microwave power more efficiently. For this study, perpendicular X-mode waves ($\theta = 0, \Gamma = 0$) were injected. The particles' initial energy was varied (with the particles' pitch-angle α staying constant):

$$5\ eV \leq E_{ini} \leq 250\ eV.$$

Fig. 4.19 shows the resulting heating power. It shows that more energetic particles indeed absorb more energy, as predicted. The amount of energy transferred to a particle is the force integrated over the path over which the force is applied:

$$E = \vec{F} \cdot \int d\vec{r}. \tag{4.5}$$

The gyrofrequency is the same for all particles; however, the distance covered during one gyromotion is larger for more energetic particles and thus more energy is absorbed.

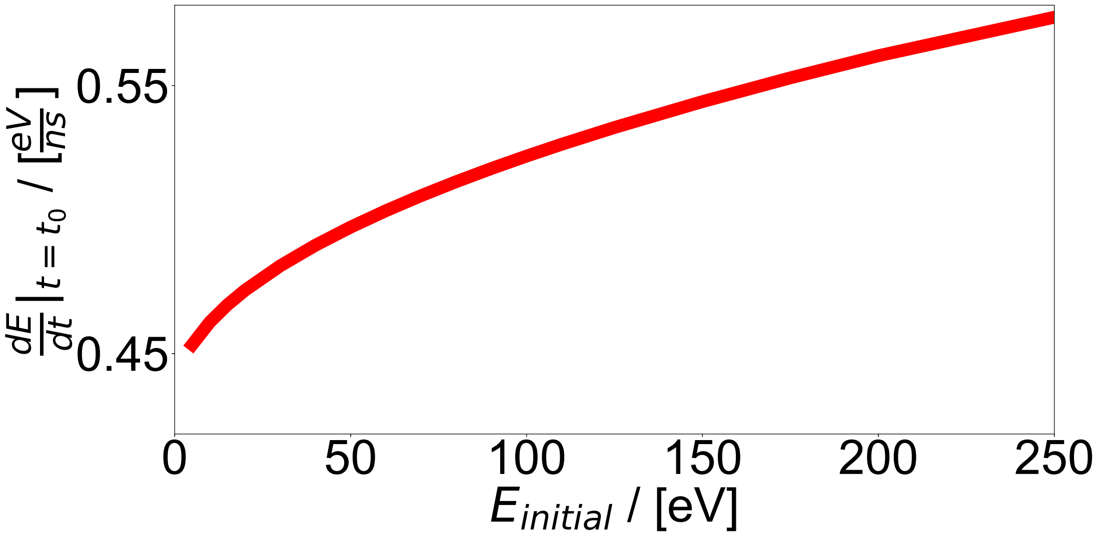

Figure 4.19: Heating power $\frac{dE}{dt}$ as a function of the particles' initial energy for X-mode heating.

Comparing the values for initial energies of $E_0 = 5\ eV$ (background thermal electrons) and $E_0 = 100\ eV$ (electrons from electron gun),

$$\frac{\frac{dE}{dt}_{100\ eV}}{\frac{dE}{dt}_{5\ eV}} = \frac{0.52}{0.45} \approx 1.16, \tag{4.6}$$

we see that the hot electrons (initially) absorb about 16 % more energy from the microwaves than the background electrons.

Wave intensity I The intensity of the wave was estimated using eq. 3.61. Since the estimate is very crude, the influence of this parameter on the heating power was studied.

As in the previous case, perpendicular X-mode waves were injected and the intensity I of the wave was varied. The particles' initial energy was $E_{ini} = 100\ eV$. Fig. 4.20 shows the heating power as function of intensity.

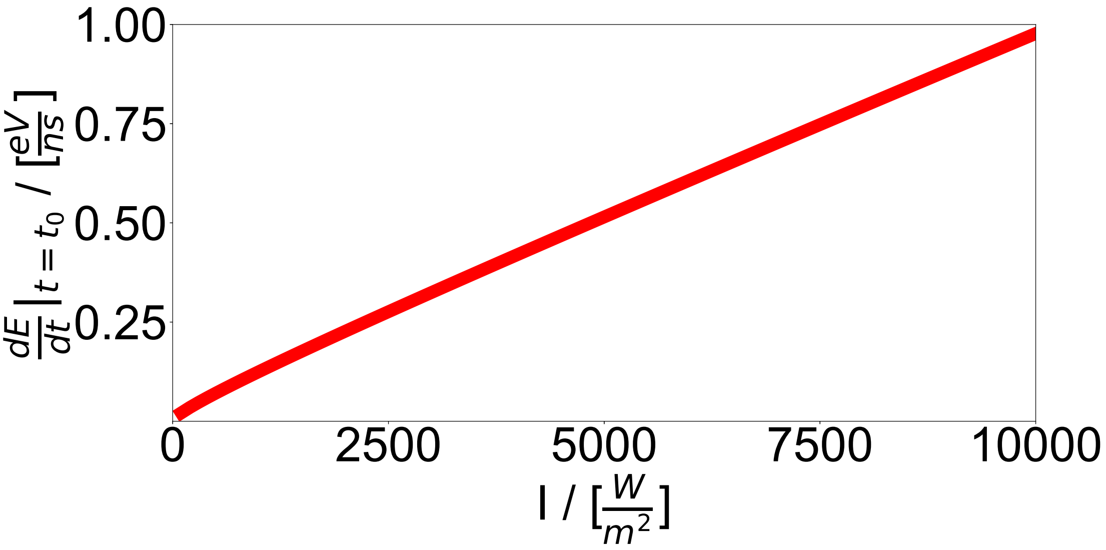

Figure 4.20: Heating power $\frac{dE}{dt}$ as a function of the intensity of the wave.

The dependency of the heating power on the used intensity is linear.

4.5.5. Wave sources in CNT

Due to the uniform, non-polarized wave field in CNT (section 3.2.12), two different means to implement the microwaves are proposed:

- Single source at the location of the entry window. The window was located on the top half-shell of CNT's vacuum vessel. In the simulation frame, the location can be approximated as:

$$\vec{r}_{window} = \begin{pmatrix} 0.0 \\ 1.0 \\ 0.0 \end{pmatrix}$$

  Fig. 4.21 shows the location in respect to the CNT-coils (black lines) and the vacuum vessel (grey surface).

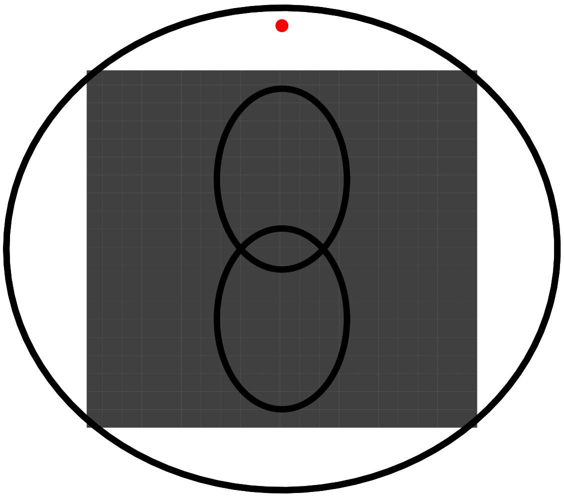

Figure 4.21: Approximate location of the entry port (red dot), from which the microwaves entered CNT in previous experiments. The CNT coils are sketched in black, the vessel is depicted by the gray surface.

At the start of a simulation, the various random angles to define direction and polarization of the wave (eq. 3.58, 3.59) are assigned.

- A second possibility is to use multiple sources, distributed along CNT's vessel walls. The polarization, direction of propagation and phase of each individual source are random. The intensity per source I_i is the total intensity I_{tot} divided by the total number of sources n_{tot}:

$$I_i = \frac{I_{tot}}{n_{tot}}.$$

The resulting total wave electric field $\vec{E}_{tot}$ at a given position $\vec{r}$ and time t is given by the sum of the single electric fields:

$$\vec{E}_{tot}(\vec{r},t) = \sum_{i=1}^{n_{tot}} \vec{E}_i(\vec{r},t). \tag{4.7}$$

Due to interference, the addition of any single source can either be constructive or destructive.

The ideal number of sources needs to be evaluated. Fig. 4.22 shows an example with $n_{tot} = 36 \cdot 17 = 612$ wave sources, evenly spread throughout CNT.

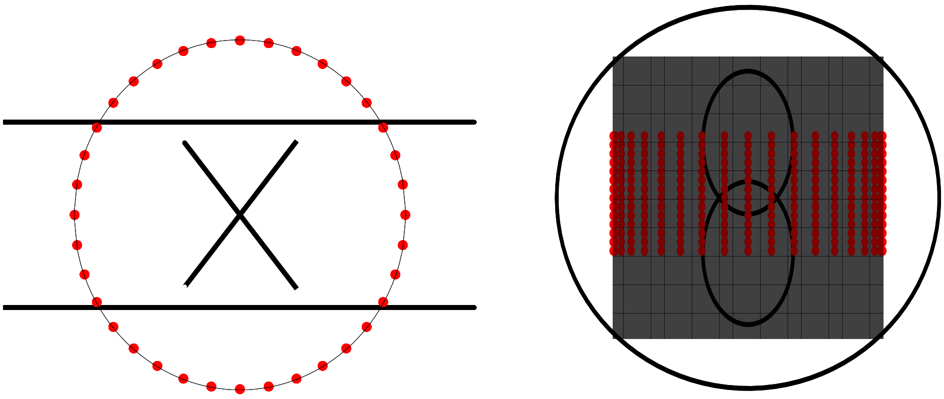

(a) Wave source distribution throughout CNT vessel - top view.

(b) Wave source distribution throughout CNT vessel - vertical cut view.

Figure 4.22: Example for distribution of wave sources (red dots) on CNT vessel wall. The gray region depicts the cylindrical part of the vessel. The black lines depict CNT's coils.

4.5.6. Pulsed microwaves operation

At the end of section 3.2.12, the pulsed operation of the microwaves was described. Fig. 4.23 illustrates this general behaviour. An electron is under the influence of a single microwave source, as presented in the previous section. The parameters φ, θ, Λ and Γ were randomly chosen at the start of the simulation and the values for this single simulation are given at the top of the figure.

For showcasing purposes, the pulse duration was artificially shortened by a factor 10^3, making the duration $\tau_{pulse} = 6\ \mu s$ and the interval length $\tau_i = \frac{1}{60 \cdot 10^3} \approx 16.6\ \mu s$. The heating is activated during the time intervals marked by the light blue box (solid black line) and deactivated anywhere else (dotted black line). It is plain to see that the particles' energy (red line) will change during the active microwave pulses while staying constant at other times.

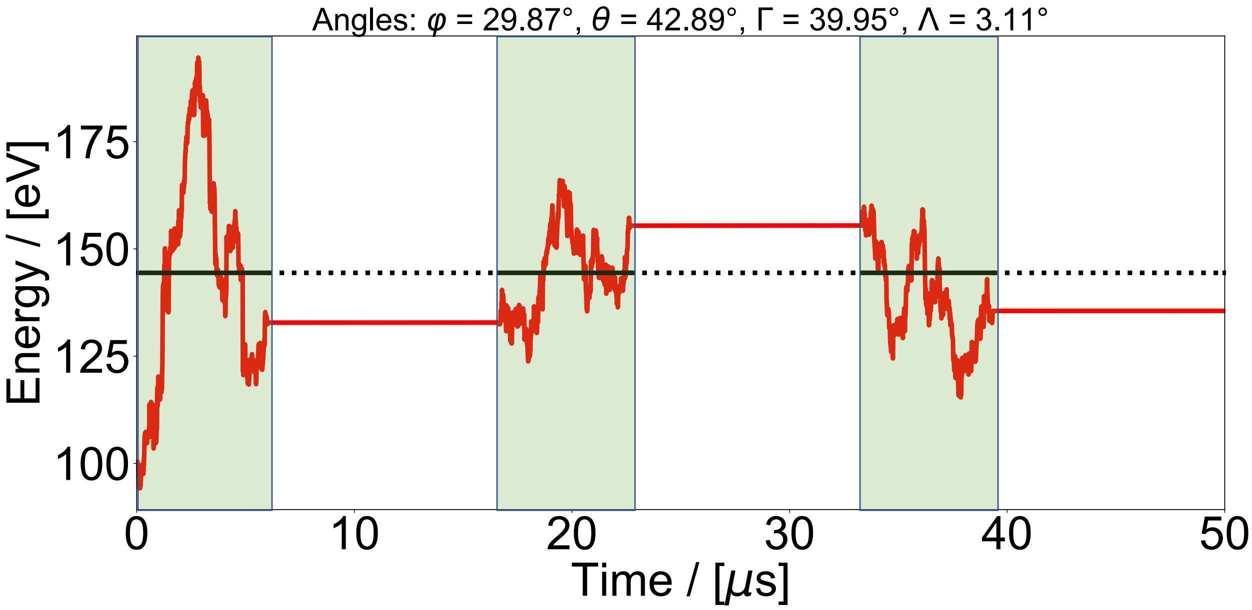

Figure 4.23: Energy history of a single electron under the influence of a pulsed microwaves. The random parameters defining the wave electric field are assigned at the start of the simulation and are stated at the top of the figure. For showcasing purposes, the pulse duration was $\tau_{pulse} = 6\ \mu s$ and the repetition rate was $f = 60\ kHz$.

4.5.7. Heating effect on particles

Due to the random nature of the microwave modelling, it is not straightforward to determine whether the waves actually lead to a net heating effect. To investigate and ensure that this is in fact the case, a study with 1000 single electrons was performed. Each electron had the same starting position and energy $E_{ini} = 100\ eV$, however the parameters defining the microwave electric field were chosen randomly for each single run.

Each single electron was traced for $t = 5\ \mu s$. After this time, the average particle energy was:

$$E_f = (139.19 \pm 113.71)\ eV.$$

This means, that the average energy gain $\bar{E}_g$ of the electrons was:

$$\bar{E}_g = \frac{E_f - E_{ini}}{dt} \approx 7.84\ \frac{eV}{\mu s}.$$

Fig. 4.24 shows the energy as a function of time (individual blue lines) for the single electrons.

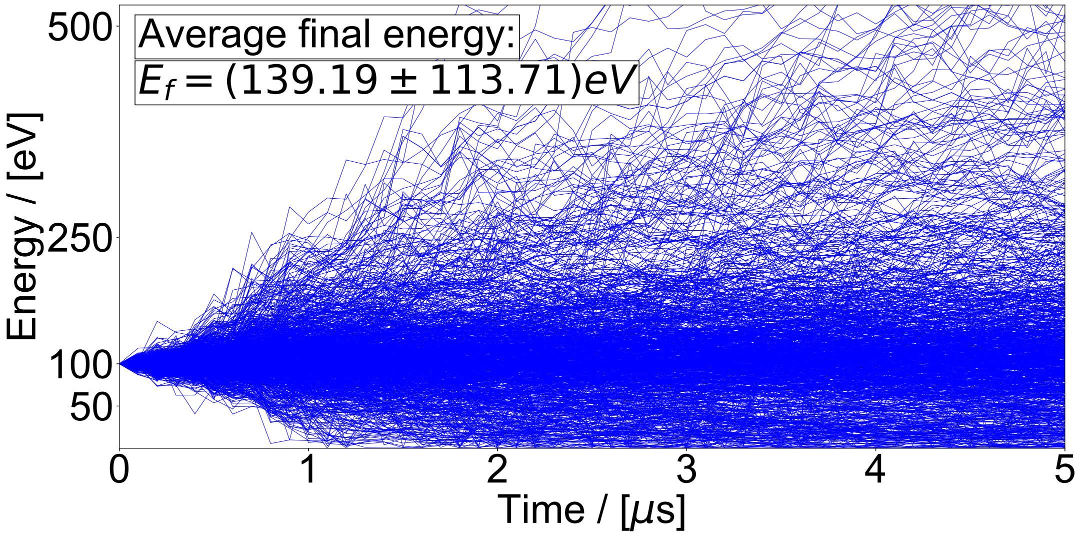

Figure 4.24: Energy history of a distribution of 1000 single electrons with identical starting position and energy. The parameters defining the random nature of the microwave are random for each single simulation. This study determined whether over a variety of single electrons there is a net heating effect.

5. Summary

Measurements in the Columbia Neutral Torus (CNT) showed a synergistic effect when simultaneously using a heated filament as well as microwave heating to start-up the plasma: the simultaneous use of the two methods led to measured densities higher than the sum of the measured densities when using each method alone (Fig. 1.3).

Candidate mechanisms to explain this synergy included the enhancement of the emission current from the filament in the presence of a wave electric field, as the electric fields influences the field emission.

Using first-principle estimates, it was shown that even under very optimistic assumptions, the influence is so small that it cannot explain the synergy. Fig. 4.1 shows the emission current in the absence and presence of this time-dependent microwave electric field. It was found, that the increase in the emission current density in the presence of the wave electric field is smaller than 0.2%. In reality, this effect is believed to be even smaller and thus this candidate mechanism was rejected.

A second proposed mechanism is an enhanced microwave absorption of the more energetic electrons emitted by the filament, as compared to background electrons used in start-up using only microwaves. To quantify this effect, a code was developed to trace single electrons in CNT's magnetic field. The trajectories of many individual, non-interacting electrons are to be traced in the presence/absence of the microwave electric field. The corresponding ionization rates (number of ionization events per unit time and unit volume) can thus be obtained. Increased ionization rates would explain higher electron densities.

A flowchart and description of the single modules present in the code are presented in appendix C.

The code uses a simple analytical expression and rotations to compute the magnetic field created by CNT's four circular coils (section 3.2.3). The magnetic field is used to solve the particles' equations of motion. The code also has the option to solve the equations of motion of the gyro-averaged guiding center.

The influence of different step sizes in the code was evaluated and results are shown in Fig. 4.6. The optimal step size for simulations were particle phenomena are of interest was found to be $dt = 10^{-11}\ s$. If only the basic trajectory is of interest, simulations with $dt \geq 10^{-9}\ s$ can be used. With this step size, the gyromotion of the particle cannot be resolved.

Besides calculating the particles' orbit, the code includes the effect of collisions between the test particle and other particles inside the plasma (section 3.2.8). Initially, the effect of single, binary collisions was included using the Rutherford scattering model. An improved formulation using a Fokker-Planck approach was then used. Rather than simulating each collision individually, this approach calculated the average, collective effect of collisions over a certain time interval dt. An additional benefit is that the effect of ion-electron collisions (leading mostly to diffusion of the test particles' momentum) as well as electron-electron collisions (resulting in energy and momentum transfer) can be combined into a single formula.

A Monte-Carlo approach to simulate ionization collisions was introduced (section 3.2.9). In the case of an ionization event, determined by its probability $P = 1 - exp(-\nu_{ion} \cdot dt)$, the electron will lose an amount of energy equal to the ionization energy E_{ion} of the colliding particle. The remaining energy will then be split between the initial electron and the one created in the process using a uniform random number R. In addition, the orbit of the initial particle will be scattered by an angle χ. If the energy of either particle after the collision exceeds a certain threshold $E > E_{threshold}$, the tracing of said particle will continue; otherwise it will stop.

An additional criterion to stop tracing is electron recombination. During each step, the particle will partake in a recombination event with a certain probability $P = 1 - exp(-\nu_{recomb} \cdot dt)$. If an electron recombines, it will be lost and the tracing will stop.

The effect of collisions on the particles' orbit was demonstrated (Fig. 4.8,4.11,4.12). The mean thermalization time τ_E^{ee}, which is the time after which a particles' energy collisionally drops to $\frac{1}{e}$ of its initial value, was evaluated. For the Rutherford collision model, it was found to be

$$\tau_{e,Rutherdorf}^{ee} = (26.4 \pm 13.4)\ \mu s.$$

For the Fokker-Planck approach, it was:

$$\tau_{e,FP}^{ee} = (20.6 \pm 11.2)\ \mu s.$$

The results of both approaches agree and both lie within the expected limits of $100\ \mu s \leq \tau_e^{ee} \leq 1\ \mu s$.

A method to include microwave heating was introduced (section 3.2.12). The electric field created by the microwaves is modelled using a plane wave approach. The electric field interacts with the particle via the Lorentz-force (eq. 3.54).

In a simple model with a homogeneous magnetic field $\vec{B} = B_0 \hat{e}_z$, the wave heating was investigated. Different wave modes, such as X-mode heating (section 4.5.1) as well as O-mode heating (section 4.5.2) were injected and the resulting heating of the particle were studied. Using a criterion for the relative heating power $\frac{dE}{dt}$ (eq. 4.4), different parameters of the wave were varied and investigated (section 4.17).

The heating is most effective when X-mode waves (polarization angle $\theta = 0$) are injected (Fig. 4.17).

Γ is the angle between the wave vector $\vec{k}$ and magnetic field $\vec{B}_0$. If there is a component $k_{||}$ parallel to $\vec{B}_0$, the angular frequency of the wave is Doppler-shifted (eq. 4.3). Γ has only a small effect on the heating power of the particle (Fig. 4.18), implying that the effect of the (parallel) Doppler-shift is only very small in CNT.

More energetic particles can absorb more energy from the microwaves (Fig. 4.19), as was predicted in the beginning of the thesis. The heating power for filament-emitted electrons ($E \approx 100\ eV$) is 16% higher than that of background electrons ($E \approx 5\ eV$).

The heating power as a function of the wave intensity I used changes linearly (Fig. 4.20).

The microwaves were injected into CNT in short pulses of $\tau_{pulse} = 6\ ms$ at a repetition rate of $f = 60\ Hz$. Fig. 4.23 shows this basic principle (with adjusted τ_{pulse}, f).

Despite the wave electric field depending on many random parameters, there should be a net heating effect on the electrons. This was studied by looking at the energy history of 1000 single electrons with different, random wave electric field parameters (Fig. 4.24). It was found that on average, an electron gains

$$\bar{E}_g \approx 7.84\ \frac{eV}{\mu s}$$

due to the interaction with the wave electric field.

6. Outlook

This project has laid the the foundation to study the synergy mechanism proposed in section 1.4. The tools for this purpose have been developed and tested. A full study, as proposed at the beginning of section 3.2, still needs to be performed in order to quantify if the proposed effect can explain the observed synergy.

A method to implement microwaves into the simulation was presented (section 4.5). Further studies of how particles behave under the influence of these microwaves inside CNT, are necessary. Two different methods of implementing the wave sources were presented in section 4.5.5. Either one should be investigated further to determine which approach is more suitable for the current studies. Additionally; if the second proposed mechanism is chosen, the optimal number and distribution of wave sources is to be determined.

If the proposed mechanism accounts for the increased densities observed in CNT, potential applications can be studied. Especially for small devices, such as CNT, using more energetic electron guns can further facilitate plasma start-up and increase the obtainable densities.

To give an estimate on the resources necessary for completion: Test runs with the full code showed that on average, the tracing of a single particle for a duration of $t \approx 1\ \mu s$ takes about $t_{CPU} \approx 10\ s$ of CPU-time. The ionization frequency (eq. 3.51) is roughly

$$\nu_{ion} \approx (10^4 - 10^5)\ Hz,$$

corresponding to an ionization roughly every

$$\tau_{ion} = \frac{1}{\nu_{ion}} \approx (10 - 100)\ \mu s.$$

In the absence of microwaves, it can be assumed that an electron with $E_{ini} = 100\ eV$ will undergo on average 2-5 ionization collisions before its energy drops below the ionization energy of $E_{ion} = 16\ eV$. For an average simulation run with

$$\tau_{sim} \approx \tau_{ion} \cdot (2 - 5) \approx (20 - 500)\ \mu s$$

and using above values for the CPU-time, a said simulation will take a total of

$$t_{CPU} = 10 \cdot (20 - 500) = (200 - 50000)\ s$$

to complete. Assuming that 100-1000 simulations are necessary for a meaningful statistics, a full run would take *at least*

$$t_f \approx (100 - 1000) \cdot 200\ s \approx (4.16 - 14.6)\ hours$$

of CPU-time.

This is just a single of the three cases presented at the start of section 3.2. Assuming the other cases will need even longer (as background electrons first need to gain energy from the microwaves before being able to partake in an ionization collisions), the computational resources alone might take up to several weeks.

Taking into account pre-processing, interpretation and post-processing of data as well accounting for any problems or bugs one might encounter along the way, it is estimated that it would require somewhere between 3 to 9 more months in order to finish.

List of Figures

References

[1] World population growth. `https://ourworldindata.org/world-population-growth`. Accessed: 2019-12-09.

[2] Energy use (kg of oil equivalent per capita. `https://data.worldbank.org/indicator/EG.USE.PCAP.KG.OE?` Accessed: 2019-12-09.

[3] Sbp statistical review of world energy, 68^{th} edition. Technical report, BP, 2019.

[4] Developing countries 2019. `http://worldpopulationreview.com/countries/developing-countries/`. Accessed: 2019-12-09.

[5] Selim Jahan et. al. *Human Development Indices and Indicators. 2018 Statistical Update.* United Nations Development Program, 2018.

[6] Kenneth S. Krane. *Introductory Nuclear Physics.* John Wiley & Sons, 1987.

[7] The use of thorium in nuclear power reactors. Technical report, U.S. Atomic Energy Commission, 1969.

[8] Ralph W. Moir and Edward Teller. Thorium-fueled underground power plant based on molten salt technology. *Nuclear Technology*, 151(3):334–340, 2005.

[9] Robert F. Hargraves & Ralph Moir. Liquid fluoride thorium reactors - an old idea in nuclear power gets reexamined. *American Scientist*, 98(4):304, August 2010.

[10] Kenneth S. Krane. *Modern physics, 3rd edition.* John Wiley & Sons, 2012.

[11] John L Johnson. Stellarator and heliotron devices. *Nuclear Fusion*, 39(2):293–294, feb 1999.

[12] T.S. Pedersen & A.H. Boozer. Confinement of nonneutral plasmas on magnetic surfaces. *Physical Review Letters*, 88(20), 2002.

[13] Thomas Sunn Pedersen, Allen H. Boozer, Jason Paul Kremer, Remi Lefrancois, Wayne T. Reiersen, Fred Dahlgren, and Neil Pomphrey. The columbia nonneutral torus: A new experiment to confine nonneutral and positron-electron plasmas in a stellarator. *Fusion Science and Technology - FUSION SCI TECHNOL*, 46:200–208, 07 2004.

[14] John W. Berkery, Thomas Sunn Pedersen, Jason P. Kremer, Quinn R. Marksteiner, Remi G. Lefrancois, Michael S. Hahn, and Paul W. Brenner. Confinement of pure electron plasmas in the columbia non-neutral torus. *Physics of Plasmas*, 14(6):062503, 2007.

[15] T. Sunn Pedersen, J. P. Kremer, R. G. Lefrancois, Q. Marksteiner, N. Pomphrey, W. Reiersen, F. Dahlgren, and Xabier Sarasola. Construction and initial operation of the columbia nonneutral torus. *Fusion Science and Technology*, 50(3):372–381, 2006.

[16] Sunn Pedersen et al. Confinement of plasmas of arbitrary neutrality in a stellarator. *Physics of Plasmas*, 11(5):2377–2381, 10 2003.

[17] X Sarasola and T Sunn Pedersen. First experimental studies of the physics of plasmas of arbitrary degree of neutrality. *Plasma Physics and Controlled Fusion*, 54(12):124008, nov 2012.

[18] K C Hammond, A Anichowski, P W Brenner, T S Pedersen, S Raftopoulos, P Traverso, and F A Volpe. Experimental and numerical study of error fields in the CNT stellarator. *Plasma Physics and Controlled Fusion*, 58(7):074002, may 2016.

[19] K. C. Hammond, R. R. Diaz-Pacheco, Y. Kornbluth, F. A. Volpe, and Y. Wei. Onion-peeling inversion of stellarator images. *Review of Scientific Instruments*, 87(11):11E119, 2016.

[20] K. C. Hammond, S. A. Lazerson, and F. A. Volpe. High-β equilibrium and ballooning stability of the low aspect ratio cnt stellarator. *Physics of Plasmas*, 24(4):042510, 2017.

[21] K C Hammond, R R Diaz-Pacheco, A Köhn, F A Volpe, and Y Wei. Overdense microwave plasma heating in the CNT stellarator. *Plasma Physics and Controlled Fusion*, 60(2):025022, jan 2018.

[22] Paul W. Brenner. *Confinement of non-neutral plasmas in stellarator magnetic surfaces.* PhD thesis, Columbia University in the City of New York, 2011.

[23] M. Bornatici. Electron cyclotron emission and absorption in fusion plasmas. *Nuclear Fusion*, 23(9):1153–1257, 1983.

[24] J.E. Harry. *Introduction to Plasma Technology.* Wiley VCH, 2010.

[25] Gerald Kamelander. Lecture notes: *Grundlagen der Plasmaphysik*, February 2018.

[26] Mohsin Raza. *Oxygen vacancy stabilized zirconia (OVSZ); synthesis and properties.* PhD thesis, Université de Mons, 03 2017.

[27] Bellan P. *Fundamentals of plasma physics.* Cambridge Press, 2006.

[28] D. J. Helander, P. & Sigmar. *Collisional transport in magnetized plasmas.* Cambridge University Pressl, 2002.

[29] Leonard Freeman. Is magnetic moment variant or invariant in a plasma? 03 2012.

[30] U. Stroth. *Plasmaphysik*. Springer Verlag, 2011.

[31] Toroidal coordinates. `http://fusionwiki.ciemat.es/wiki/Toroidal_coordinates`. Accessed: 2019-12-12.

[32] Justin Barton, W. Wehner, Eugenio Schuster, Federico Felici, and O. Sauter. Simultaneous closed-loop control of the current profile and the electron temperature profile in the tcv tokamak. *Proceedings of the American Control Conference*, 2015:3316–3321, 07 2015.

[33] H. Zohm. *Magnetohydrodynamic Stability of Tokamaks*. Wiley VCH, 2014.

[34] Mlynar Jan. Focus on: Jet. the european centre of fusion research. Technical report, Association EURATOM, 2007.

[35] Cesario R. et al. Cardinali A., Castaldo C. Radio-frequency current drive for thermonuclear fusion reactors. *Scientific Reports*, 8(10318), 2018.

[36] Lhd helical coil. `https://www-lhd.nifs.ac.jp/pub/index_e.html`. Accessed: 2019-02-20.

[37] Wendelstein 7-x erreicht weltrekord. `https://www.ipp.mpg.de/de/aktuelles/presse/pi/2018/04_18`. Accessed: 2019-12-12.

[38] Wendelstein 7-x. `https://www.ipp.mpg.de/2815232/konzeptentwicklung`. Accessed: 2019-02-20.

[39] A. Dinklage, C. Beidler, P. Helander, Golo Fuchert, H. Maaßberg, K. Rahbarnia, T. Pedersen, Y. Turkin, R. Wolf, A. Alonso, T. Andreeva, Boyd Blackwell, S. Bozhenkov, Birger Buttenschön, A. Czarnecka, Florian Effenberg, Y. Feng, Joachim Geiger, Matthias Hirsch, and Venanzio Giannella. Magnetic configuration effects on the wendelstein 7-x stellarator. *Nature Physics*, 14, 08 2018.

[40] J. Wesson. *TOKAMAKS*. Clarendon Press-Oxford, 2004.

[41] Routly P. McR. Cohen R.S., Spitzer L. The electrical conductivity of an ionized gas. *Physical Review*, 80(2), 1950.

[42] R Prater. Heating and current drive by electron cyclotron waves. *Physics of Plasmas*, 11:2349–2376, 04 2004.

[43] Neutral beam injection. `https://www.ipp.mpg.de/90419/nbi_old`. Accessed: 2019-12-12.

[44] Ralph Dux. Lecture notes: *Plasmaphysik und Fusionsforschung. Teil II: Fusionsforschung*, February 2002.

[45] J D Lawson. Some criteria for a power producing thermonuclear reactor. *Proceedings of the Physical Society. Section B*, 70(1):6–10, jan 1957.

[46] Milestones around the world. `https://www.iter.org/sci/BeyondITER`. Accessed: 2019-12-13.

[47] FerdiBf. Skizze zum wirkungsquerschnitt. `https://commons.wikimedia.org/w/index.php?curid=52305232`. Accessed: 2019-02-13.

[48] L.D. Landau and E.M. Lifshitz. *Mechanics, 3rd edition*. Butterworth Heinemann, 1981.

[49] Robert Wittmann. *Miniaturization Problems in CMOS Technology: Investigation of Doping Profiles and Reliability*. PhD thesis, TU Vienna, 2007.

[50] Arthur Beiser. *Concepts of modern physics, sixth edition*. McGraw-Hill Higher Education, 2003.

[51] Dr. H. Geiger and E. Marsden. Lxi. the laws of deflexion of a particles through large angles. *The London, Edinburgh, and Dublin Philosophical Magazine and Journal of Science*, 25(148):604–623, 1913.

[52] Christopher Albert. Lecture notes: *Plasma Physics*, October 2016.

[53] J.D. Callen. Lecture notes: *Fundamentals of Plasma Physics*, July 2006.

[54] Kennedy L.A. Fridman A. *Plasma physics and engineering, second edition*. CRC Press, 2011.

[55] Giblody H.B. Massey H., Burhop E. *Electron and Ion Impact Phenomena*. Clarendon, 1974.

[56] J. A. Dean. *Lange's Handbook of Chemistry*. McGraw-Hill, 1999.

[57] Jiri Pavlu Jana Safranovka, editor. *Recombination in He/Ar Afterglow Plasma at Low Temperatures*. MATFYZPRESS, May 2012.

[58] H. P. Laqua, H. Maassberg, N. B. Marushchenko, F. Volpe, A. Weller, and W. Kasparek. Electron-bernstein-wave current drive in an overdense plasma at the wendelstein 7-as stellarator. *Phys. Rev. Lett.*, 90:075003, Feb 2003.

[59] Francesco Volpe. *Electron Bernstein emission diagnostic of electron temperature profile at W7-AS Stellarator.* PhD thesis, Ernst-Moritz-Arndt-Universitaet Greifswald, 2003.

[60] Kenneth C. Hammond. *Heating and stability of neutral CNT stellarator plasmas.* PhD thesis, Columbia University in the City of New York, 2017.

[61] Francis F. Chen. *Introduction to Plasma Physics and Controlled Fusion.* Springer, 2015.

[62] Jon Orloff. *Handbook of Charged Particle Optics.* Crc Press Inc, 2008.

[63] J. Laimer. Lecture notes: *Plasmatechnologie und -chemie*, September 2017.

[64] C. Davisson and L. H. Germer. The thermionic work function of tungsten. *Phys. Rev.*, 20:300–330, Oct 1922.

[65] Energy in electromagnetic waves. `https://courses.lumenlearning.com/physics/chapter/24-4-energy-in-electromagnetic-waves/`. Accessed: 2019-12-24.

[66] J.C. Butcher. *Numerical Methods for Ordinary Differential Equations.* John Wiley & Sons, Ltd., 2008.

[67] Runge-kutta slopes. `https://upload.wikimedia.org/wikipedia/commons/7/7e/Runge-Kutta_slopes.svg`. Accessed: 2019-02-13.

[68] A.W. Clark, M. Doumet, K. Hammond, Yosef Kornbluth, D. Spong, Ryan Sweeney, and Francesco Volpe. Proto-circus tilted-coil tokamak–torsatron hybrid: Design and construction. *Fusion Engineering and Design*, 89:2732–2737, 11 2014.

[69] Immer C. Youngquist R. Simpson J., Lane J. Simple analytic expressions for the magnetic field of a circular current loop. Technical report, NASA, 02 2001.

[70] Hubert Nguyen. *Gpu Gems 3.* Addison-Wesley Professional, first edition, 2007.

[71] Kenro Miyamoto. *Fundamentals of plasma physics and controlled fusion.* Iwanami Book Service Centerr, first edition, 1999.

[72] V. Vahedi and M. Surendra. A monte carlo collision model for the particle-in-cell method: applications to argon and oxygen discharges. *Computer Physics Communications*, 87(1):179 – 198, 1995. Particle Simulation Methods.

[73] B G. Lindsay, H C. Straub, Ken Smith, and R Stebbings. Absolute partial cross sections for electron-impact ionization of h-2, n-2, and o-2 from threshold to 1000 ev. *Physical Review A - PHYS REV A*, 54:2146–2153, 09 1996.

[74] W. von der Linden E. Arrigoni. Lecture notes: *Elektromagnetische Felder und Elektrodynamik*, March 2015.

[75] S. Ma, R.D. Sydora, and J.M. Dawson. Binary collision model in gyrokinetic simulation plasmas. *Computer Physics Communications*, 77(2):190 – 206, 1993.

Appendices

A. Useful formulas

Lorentz-force acting on particle in presence of electric/magnetic fiels:

$$\vec{F}_L = q(\vec{E} + \vec{v} \times \vec{B}) \tag{A.1}$$

Debye length:

$$\lambda_D = \sqrt{\frac{\varepsilon_0 k_B T}{ne^2}} \tag{A.2}$$

Plasma-frequency:

$$\omega_{pe} = \sqrt{\frac{n_e e^2}{m_e \varepsilon_0}} \tag{A.3}$$

Cyclotron frequency:

$$\Omega_c = \frac{|q|B}{m} \tag{A.4}$$

Plasma-cutoff-density:

$$n_{cutoff} = \frac{\varepsilon_0 m_e}{e^2} \omega_{wave}^2 \tag{A.5}$$

Larmor-radius:

$$r_L = \frac{mv_\perp}{|q|B} \tag{A.6}$$

Coulomb-logarithm:

$$ln(\Lambda) = ln(\frac{b_{max}}{b_{min}}) = ln(\lambda_D \cdot \frac{4\pi\varepsilon_0(mv^2)}{e^2}) \tag{A.7}$$

Particle magnetic moment:

$$\mu = \frac{mv_\perp^2}{2B} \tag{A.8}$$

Plasma-β:

$$\beta(\vec{r}) = \frac{p_{plasma}}{p_{magn}} = \frac{nk_B T}{B^2(\vec{r})/2\mu_0} \tag{A.9}$$

Particles' pitch-angle:

$$\alpha = tan^{-1}(\frac{v_{\perp}}{v_{||}}) \tag{A.10}$$

Doppler-shifted wave frequency:

$$\omega_{wave} = \frac{l\Omega_{ce}}{\gamma} + k_{||}v_{||} \tag{A.11}$$

General form for electric field of a plane wave:

$$\vec{E}(\vec{r},t) = \vec{E}_0 e^{i(\vec{k}\cdot\vec{r}-\omega t+\varphi)} \tag{A.12}$$

Wave-number for electric wave:

$$|\vec{k}| = \frac{\omega}{c} \tag{A.13}$$

Wave propagation modes:

- O-mode:

$$\vec{E}_w || \vec{B}_0$$

- X-mode:

$$\vec{E}_w \perp \vec{B}_0$$

Electromagnetic amplitude (as function of its intensity I):

$$|E_0| = \sqrt{\frac{2I}{c\varepsilon_0}} \tag{A.14}$$

Current density for a heated, biased filament:

$$j(E,T) = BT^2 exp\left(-\frac{\Phi}{k_B T} + \frac{\sqrt{\frac{e^3 E}{4\pi\varepsilon_0}}}{k_B T}\right) \tag{A.15}$$

Probability for collision event to take place in a time-interval dt:

$$P = 1 - exp(-\nu_{coll} \cdot \Delta t) \tag{A.16}$$

Collisional frequency:

$$\nu = |v_{rel}| n_2 \sigma(E) \tag{A.17}$$

B. Switching to and from z-frame

Switching to the z-frame For the GCM, which averages over the gyrophase, only the velocity components $v_{||}$ and $v_\perp$ are known at a specific point. First up, the magnetic field vector $\vec{b}$ is rotated to align with the z-axis:

$$\begin{aligned}
\vec{b} &= \frac{\vec{B}}{B} && \text{(B.1)}\\
\phi_{GCM} &= f_R(b_x, b_y) && \text{(B.2)}\\
\vec{b}^* &= R_z(-\phi_{GCM}) \cdot \vec{b} && \text{(B.3)}\\
\psi_{GCM} &= \frac{\pi}{2} - rotangle(b_y^*, b_z^*) && \text{(B.4)}\\
\vec{b}^{**} &= R_y(-\psi_{GCM}) \cdot \vec{b}^* = \hat{e}_z. && \text{(B.5)}
\end{aligned}$$

The function f_R`(opp,adj)` computes the angle φ between its two arguments. Depending on the (2D)-value of its components (and thus the respective quartile, see Fig. B.1), the value of the angle φ will differ by an additive factor. The base value is simply:

$$\psi = tan^{-1}\left(\frac{abs(opp)}{abs(adj)}\right),$$

and an extra factor is added according to the quartile, as shown in table B.1.

Quartile	**opp**	**adj**	φ
0	0	> 0	0
0	0	< 0	π
0	> 0	0	$\frac{\pi}{2}$
0	< 0	0	$\frac{3\pi}{2}$
1	> 0	> 0	ψ
2	< 0	> 0	$\psi + \frac{\pi}{2}$
3	< 0	< 0	$\psi + \pi$
4	> 0	< 0	$\psi + \frac{3\pi}{2}$

Table B.1: Value of the function $\varphi = f_R(opp, adj)$, depending on input parameters.

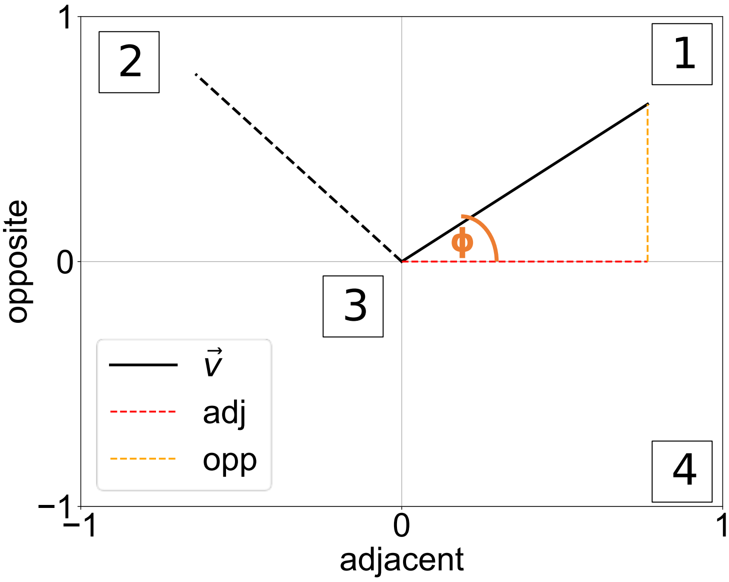

Figure B.1: Quartiles used in the calculation of the rotation angle φ in the $f_R(opp, adj)$ function.

Fig. B.2 depicts how an initial, arbitrary vector $\vec{b}$ (orange dotted line) is rotated to align with the $\hat{e}_z$-axis ($\vec{b}''$, blue dotted line).

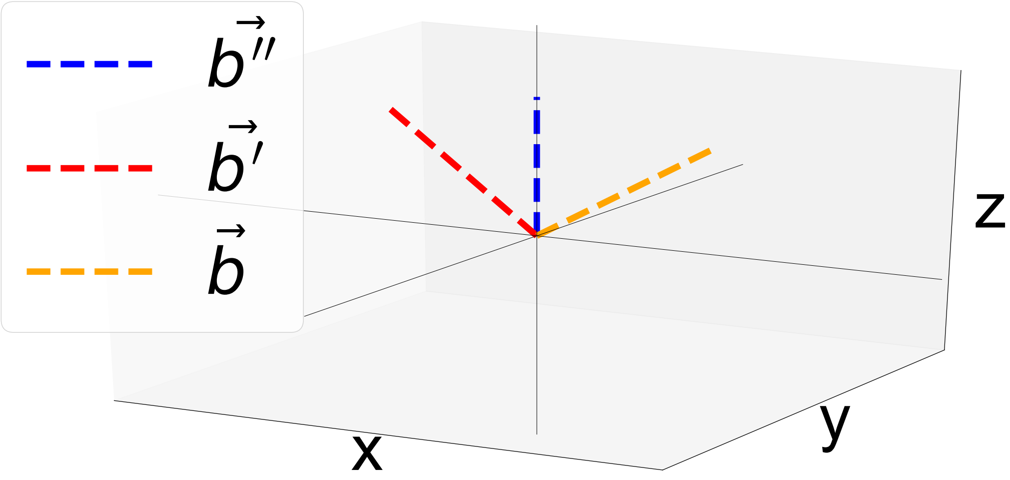

Figure B.2: Demonstration of the 3D-vector rotation. An arbitrary magnetic field vector $\vec{b}$ (orange dotted line) is rotated to align with the $\hat{e}_z$-axis (blue dotted line).

The components of the GCM-Tracing will still have the pitch-angle α as well as the (random) phase δ (section 3.2.5). In the frame, where $\vec{b} = \hat{e}_z$, the velocity is given by:

$$\vec{v}^{*}_{GCM} = \begin{pmatrix} cos(\delta) \cdot v_{\perp} \\ sin(\delta) \cdot v_{\perp} \\ v_{||} \end{pmatrix}. \tag{B.6}$$

To align the velocity with $\hat{e}_z$, two more rotations $R_z(-\delta)$ and $R_y(-\gamma)$ are required:

$$\vec{v}^{**}_{GCM} = R_y(-\gamma) \cdot R_z(-\delta)\vec{v}^{*}_{GCM} = v \cdot \hat{e}_z. \tag{B.7}$$

For the single particle tracing, the procedure is very similar. An initial vector $\vec{v} = \begin{pmatrix} v_x \\ v_y \\ v_z \end{pmatrix}$ is transformed as follows:

$$\phi_{PT} = f_R(v_x, v_y) \tag{B.8}$$

$$\vec{v}^{*}_{PT} = R_z(-\phi_{PT}) \cdot \vec{v} \tag{B.9}$$

$$\psi_{PT} = \frac{\pi}{2} - f_R(v^*_y, v^*_z) \tag{B.10}$$

$$\vec{v}^{**}_{PT} = R_y(-\psi_{PT}) \cdot \vec{v}^{*} = v \cdot \hat{e}_z. \tag{B.11}$$

Switching back to lab frame The rotations and rotation angles are specifically important to transform the velocity after the collision (in the z-frame) $\vec{v}'_{z-frame}$ back to the lab frame.

In the case of particle tracing, this is fairly straightforward: the velocity after the collision in the lab-frame (LF) is:

$$\vec{v}'_{LF,PT} = R_z(\phi_{PT}) \cdot R_y(\psi_{PT}) \cdot \vec{v}'_{z-frame}, \tag{B.12}$$

where ϕ_{PT} and ψ_{PT} are the angles from eq. B.8 and B.10.

For the GCM, we first compute $v_{||}$ and $v_{\perp}$ after the collision. To achieve this, the vector after the collision $\vec{v}'_{z-frame}$ is rotated to a frame where $\vec{b} = \hat{e}_z$:

$$\vec{v}'_{bz} = R_z(\delta) \cdot R_y(\gamma) \cdot \vec{v}'_{z-frame}. \tag{B.13}$$

In this frame, the guiding center velocity components are (once again):

$$v'_{||} = \sqrt{(v'_{bz;x})^2 + (v'_{bz;y})^2}$$

$$v'_{\perp} = v'_{bz;z}.$$

The velocity of the guiding center after the collision in the lab-frame is:

$$\vec{v}'_{GCM} = R_z(\phi_{GCM}) \cdot R_y(\psi_{GCM}) \cdot \vec{v}'_{bz}, \tag{B.14}$$

where the angles ϕ_{GCM} and ψ_{GCM} are the ones from eq. B.2 and B.4.

Despite $\vec{v}'_{GCM}$ not being needed for the continued tracing, it is necessary to compute the displacement $d\vec{r}$ of the particle due to a collision. It is given by: [75]

$$d\vec{r} = -\frac{d\vec{v} \times \vec{b}}{\Omega_e}, \tag{B.15}$$

where $d\vec{v} = \vec{v} - \vec{v}'$ is the change of velocity due to the collisions and Ω_e is the electron gyrotron frequency (see eq. 2.10).

C. Program Flowchart

Fig. C.1 shows the flowchart of the final code and the modules contained therein.

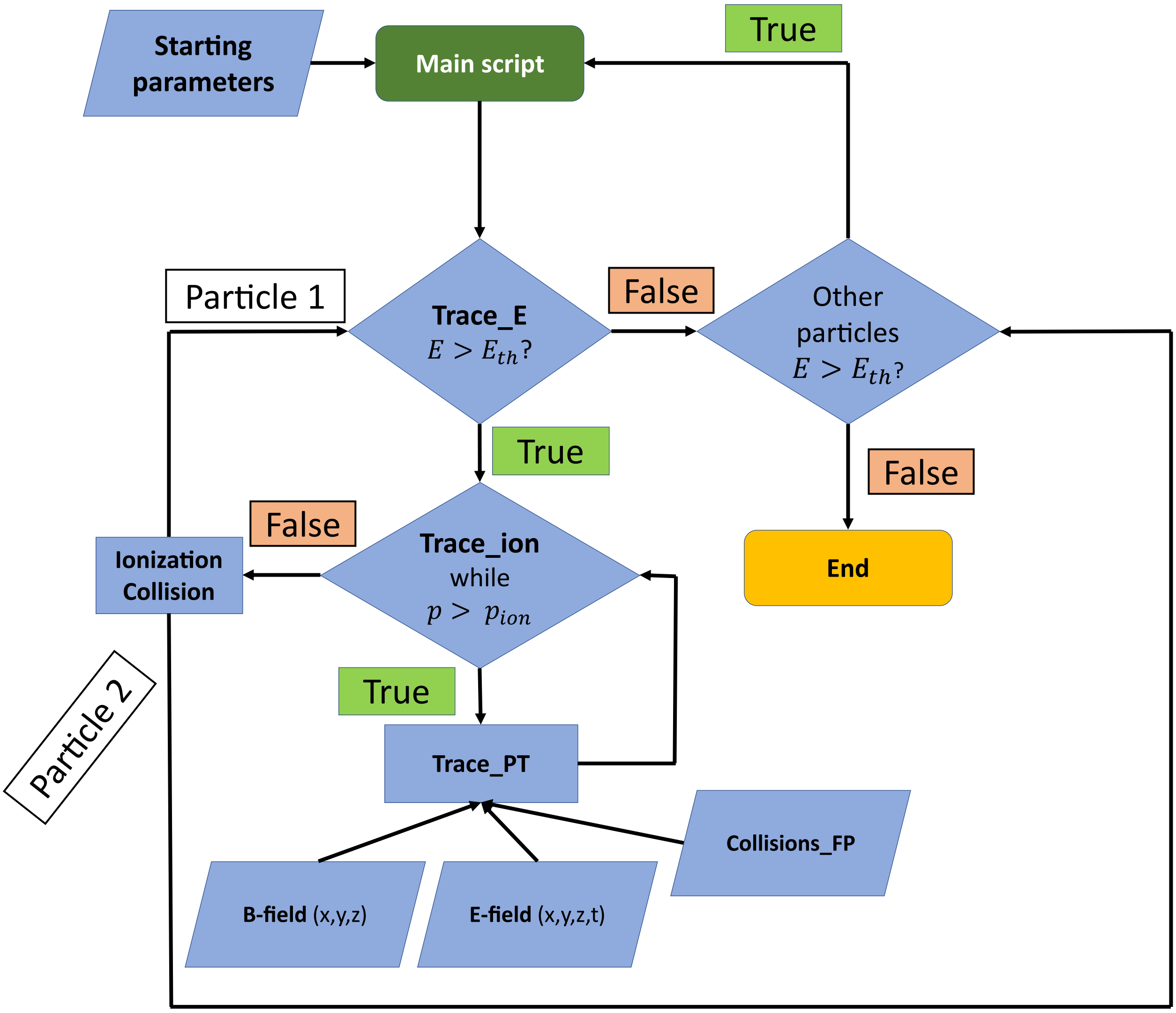

Figure C.1: Flowchart of the final code and how the single modules interact with each other.

A short description of the single modules:

- **Starting parameters:** Gives the starting position, energy and pitch-angle α of the particle. The velocity components will then be computed using the magnetic field at the particles' position.
- **Main script:** Main Fortran-program.
- **Trace E:** Traces the current particle, until its energy has dropped below a certain threshold-energy E_{th} after the particle underwent an ionization collision.
- **Trace ion:** For every step, a new random number $0 \leq p < 1$ is created. As long as $p > p_{ion}$; with p_{ion} being the ionization probability (section 3.2.9); the tracing continues.

- **Trace PT (Particle Tracing):** Module where the step integration takes place. First, the change in velocity $d\vec{v}$ as a result of collisions is computed (eq. 3.44) and next the equations of motion are integrated using the RK4-method (section 3.2.1). The magnetic field is computed using the model presented in section 3.2.3; the electric field computed using the approach from section 3.2.12.

- **Ionization collision:** Once $p < p_{ion}$, an ionizing collision takes place. The energy and velocities of the two resulting electrons are computed using the approach in section 3.2.9. The incident particle is then returned to module Trace E, where the tracing continues if $E > E_{th}$. The second particle is then added to the list of secondary particles, to be traced later.

- **Other particles:** If the particle undergoes an ionizing collision, the position $\vec{r}$ and velocity $\vec{v}$ of the secondary particle are saved to an external file and once the energy of the initial particle drops below threshold E_{th}, the tracing of that initial particle stops. If any of the secondary particles has an energy $E > E_{th}$, the tracing for this new particle will continue, until eventually no particles with $E > E_{th}$ are left and the code ends.

- **Exit criteria:** In addition to the particle energy dropping below E_{th}, the tracing for a single particle will also stop if the particle leaves the simulation domain or it recombines (section 3.2.11).